UNIVERSITY OF THE WITWATERSRAND

SCHOOL OF MECHANICAL, INDUSTRIAL AND

AERONAUTICAL ENGINEERING

OPTIMIZING THE SURFACE INTEGRITY OF MACHINED Ti-6Al-4V USING ADVANCED CARBIDE INSERTS AND MINIMUM QUANTITY LUBRICATION

OFEM, NWEOYI LEKAM

A thesis submitted to the Faculty of Engineering and the Built Environment, University of the Witwatersrand, Johannesburg, in fulfilment of the requirements for the degree of Masters of Science in Engineering.

MAY, 2016

DECLARATION

Name: Ofem, Nweoyi Lekam Student Number: 1108612

I, the undersigned, declare that this thesis is my own unaided work, being submitted to the University of Witwatersrand, Johannesburg for a Degree of Masters of Science.

I hereby declare the following:

- I am aware that plagiarism (the use of someone else's work without their permission and/or without acknowledging the original source) is wrong;
- I confirm that the work submitted herewith for assessment in the above course is my own unaided work except where I have explicitly stated otherwise;
- This task has not been submitted before, either individually or jointly, for any course requirement, examination or degree at this or any other tertiary educational institution;
- I have followed the required conventions in referencing the thoughts and ideas of others;
- I understand that the University of the Witwatersrand may take disciplinary action against me if it can be shown that this task is not my own unaided work or that I failed to acknowledge the sources of the ideas or words in my writing in this task.

…………………………………………………

(Signature)

………………… day of …………………. Year………….

ABSTRACT

This research is focused on optimizing the surface integrity of Ti-6Al-4V using advanced carbide inserts and minimum quantity lubrication (MQL). Experiments were designed to machine twenty Ti-6Al-4V blocks under dry and MQL lubricating conditions using innovative cemented carbide inserts produced by Liquid Phase Sintering (LPS) and Spark Plasma Sintering (SPS). The cutting speed, feed rate, and depth of cut, were considered as machining parameters, while the cutting force, temperature, tool wear, surface roughness and residual stress were considered as performance characteristics. The results obtained for surface roughness and residual stress measurements were used to analyze the surface integrity of the machined Ti-6Al-4V samples. The influence of sintering techniques and milling parameters on performance characteristics and surface integrity were investigated from experimental results obtained. Discrepancy in behavioral trends with respect to lubricating conditions was also investigated. The analyses of milling results showed that cutting speed played a major role in the optimization of surface integrity of the Ti-6Al-4V workpieces followed by the depth of cut. The results also showed that the LPS inserts performed better than the SPS inserts due to their better mechanical properties (higher fracture toughness (K_{IC}) and transverse rupture strength). The application of MQL was also observed to significantly reduce milling temperatures resulting in better surface integrity. However, an optimized surface integrity of the Ti-6Al-4V samples was achieved during MQL milling with the 10Co-L insert at a low finishing speed of 75m/minute and a reduced depth of cut of 0.5mm.

DEDICATION

I would like to foremost dedicate this work to God almighty who has made this research a success. I will also like to dedicate this work to my beloved wife; Mrs. Marlisa Lekam, and my mother; Mrs. Alice Ofem, who steadfastly stood by me throughout the course of this research.

ACKNOWLEDGMENTS

I thank Almighty God for his grace and favors during this research. This research would have been impossible if not for the Lord being on my side.

I also thank Dr. Stephen Akinlabi for his enormous contributions towards the commencement of this research.

I appreciate my mother, Mrs. Alice Ofem and my wife, Mrs. Marlisa Lekam for their encouragements and supports.

I also appreciate Le Roux Heinrich for his encouragement during this research.

My sincere gratitude goes to my project supervisors, Prof. Claudia Polese and Dr. Rodney Genga for their exceptional supervision, advice and guidance throughout this research. It was a privilege having an opportunity to work with them and sharing from their valuable expertise and knowledge.

TABLE OF CONTENTS

LIST OF TABLES

LIST OF FIGURES

GLOSSARY

Binder	A substance added to the powder to increase the strength of the compact and cement together powder particles that alone would not sinter into a strong object.
PCBN	Polycrystalline Cubic Boron Nitride.
PCD	Polycrystalline diamond.
Rockwell hardness number (HR)	A number derived from the net increase in depth of impression as the load of the indenter is increased and decreased from a fixed load. The numbers are always quoted with a scale symbol.
Spindle	A rotation axis of a machine, on which a cutting tool is mounted.
SRT	Scheduled Replacement Time (e.g. 30 minutes).
Vickers hardness number	An indentation hardness test employing a 136^{o} diamond pyramid indenter (Vickers) and variable loads, enabling the use of one hardness scale for all ranges of hardness.
WC	Tungsten Carbide.
XRD	X-Ray Diffraction.

NOMENCLATURE

Symbol	Description	Unit
a_p	Axial Depth of Cut	Mm
v_c	Cutting Speed	m/minute
F_x	Force in x axis N	N
V_f	Feed rate	m/minute
f_z	Feed/tooth	Mm
F_y	Force in y axis N	N
F_z	Force in z axis N	N
a_e	Radial depth of Cut	Mm
F_R	Resultant Force N	N
R_a	Mean Surface Roughness	Mm
N	Spindle Speed	m/minute
R_q	Root mean square that corresponds to Ra	Mm
σR_a	Standard deviation for the roughness	Mm
R_t	Sum of max peak a max depth in on surface	Mm
R_z	Sum of max peak a max depth in sample space on surface	Mm

Chapter 1 : Introduction

1.1 Background

Machinability refers to the ease or difficulty of a material to be machined [2003Kir]. The machinability of a material can be termed 'good' if low temperatures and cutting forces are experienced during machining, continuous chips are easily removed, tool life is longer, and an acceptable surface integrity is achieved [2003Kri]. Titanium and its alloys are considered difficult to machine materials owing to their relatively high machining cost resulting from high tool expense and poor surface integrity of machined components [2003Kri]. Therefore, the optimization of machining parameters is an important step for economic machining of Ti-6Al-4V, as it entails utilization of mathematical models to select machining parameters with respect to achieving minimum tool wear and high surface integrity at the most effective cost. During optimization, an alternative with most cost effective or highest achievable performance is sought after, with desired factors maximized and undesired ones minimized [2015Url[a]]. In order to justify the optimisation of surface integrity as well as increase machining efficiency, the adjustment of machining parameters is a necessity [2006Cus].

1.2 Aim

This research is aimed at optimizing the surface integrity of Ti-6Al-4V using innovative cemented carbide inserts produced by Liquid Phase Sintering (LPS) and Spark Plasma Sintering (SPS) under dry and minimum quantity lubricating conditions. The cutting speed, feed rate, and depth of cut will be considered as machining parameters, while the cutting forces, temperature, tool wear, and surface roughness (R_a) will be considered as performance characteristics correlating to surface integrity. An analysis of the influence of milling parameters on performance characteristics during Ti-6Al-4V machining will be conducted for optimization.

1.3 Objectives

The objective of the research is to improve the production of reliable Ti-6Al-4V components in South Africa and the world at large. Furthermore, this research will contribute immensely to existing literature in the field Ti-6Al-4V machining.

1.4 Motivation

A large amount of research has been published on optimizing the surface integrity and machining of Ti-6Al-4V alloy under dry and flood lubricating conditions with traditional tungsten carbide (WC) and polycrystalline diamond (PCD) tools produced by conventional sintering [2014Sat]. Little or no research efforts have however, been focused towards utilizing other cemented carbide tools with higher mechanical properties than tungsten carbide or utilizing advanced lubricating techniques such as Minimum Quantity Lubrication (MQL).

1.5 Hypothesis

The machining of Ti-6Al-4V using cemented carbide tools with superior mechanical properties to tungsten carbide tools could result in optimized surface integrity. Also, varying the sintering techniques used in producing cemented carbide tools could improve upon their mechanical properties such as abrasion and chemical wear resistance, fracture toughness, and hardness which would further improve their performance in Ti-6Al-4V machining, as well as reduce overall machining cost. It is expected that a decrease in milling temperature and forces with the application of MQL could further improve both the tool life and the surface integrity of the machined Ti-6Al-4V components.

1.6 Overview

This study seeks to optimize machining parameters for Ti-6Al-4V using innovative carbide tools under dry and MQL milling conditions. The innovative cutters were designed by altering the binder matrixes of industrially accepted tungsten, nickel and niobium carbide tools, and adding alloying elements which may improve upon their properties. Both Liquid Phase Sintering (LPS) and Spark Plasma Sintering (SPS) techniques were used in the production of the cutting tool inserts in a bid to improve upon their mechanical properties. Minimum quantity lubrication was applied during some finishing milling runs with the aim of decreasing milling temperatures, lubricating cutting tool edges and cleaning workpiece – tool contact surfaces. The resultant effect of MQL was then compared to that of dry machining in finishing runs. Mechanical properties such as wear resistance (flank and crater) and surface roughness (R_a) were then investigated and correlated to surface integrity. Similarly, the effect of cutting speed, feed rate, depth of cut, and MQL on surface integrity were also investigated.

Chapter 2 gives a detailed literature review on the workpiece material (Ti-6Al-4V), milling and milling parameters, sintering techniques, minimum quantity lubrication (MQL), tool wear, surface integrity, and residual stress.

Chapter 3 describes the experimental procedures and facilities used for this research

Chapter 4 is the data analysis and results obtained during the milling processes.

Chapter 5 discusses trends picked up during the optimization process.

Chapter 6 is the conclusion and recommendation for future study.

Chapter 2 : Literature Review

2.1 Theoretical background

Titanium is the ninth most abundant metal on the earth's crust [1981For]. It was discovered in Cornwall, Great Britain, by William Gregor in 1971 and named after the Titans (the powerful sons of the earth in Greek mythology) [1981For]. Titanium only occurs in nature in chemical combinations with mostly oxygen and iron [1981For]. Titanium is usually alloyed with iron, aluminum, vanadium and molybdenum, among other elements to improve its strength to weight ratio [2006Enc]. These alloys of Titanium can generally be classified into four main categories namely; alpha alloys, near – alpha alloys, alpha and beta alloys, and beta alloys [2006Jaw]. Titanium grade V alloy (Ti-6Al-4V) is the workhorse alloy of the titanium industry [2010Dav]. It exists in the alpha + beta phase, with aluminium as the alpha stabilizer and vanadium as the beta stabilizer [2010Dav]. Ti-6Al-4V is composed of 6% aluminium, 4% vanadium, 0.25% iron, 0.2% oxygen, and 89.55% titanium, making it significantly tougher than commercial titanium possessing the same stiffness and thermal properties [1993Hon[a]]. The high strength, low density, and excellent fatigue/corrosion resistance of Ti-6Al-4V makes it suitable for manufacturing components requiring high reliability [1997Ezu]. The mechanical and thermal properties of Ti-6Al-4V are shown in Table 2.1 and Table 2.2 respectively [1996Joh]. Despite these exceptional properties and increased utilization of Ti-6Al-4V in manufacturing, the ability to produce components with high productivity and good surface integrity has continually been a challenge owing to complexities associated with its fabrication and machining [1984Mye].

At elevated temperatures the high strength of Ti-6Al-4V opposes plastic deformation required for chip formation. This results in excessive build-up of temperature on the tool face resulting to premature tool failure [2012Mac]. Additionally, when machining Ti-6Al-4V at low cutting speeds, the cutting tool inserts are prone to Built-Up Edge (BUE) formation which usually results in poor surface finish and rapid tool wear [1953Coo]. Similarly, the chemical reactivity of Ti-6Al-4V with almost all tool materials at temperature exceeding 500^{o}C results in chipping, welding, and premature tool failure [1970Zla]. Additionally, its high strength maintained by Ti-6Al-4V at elevated temperature and its low modulus of elasticity further impairs its machinability [1993Hon].

Table 2.1: Mechanical properties of Ti-6Al-4V [1996Joh]

Properties	Metric	Comment
Hardness, Brinell	334	Estimated from Rockwell C.
Hardness, Knopp	363	Estimated from Rockwell C.
Hardness, Rockwell C	36	Estimated from Rockwell C.
Hardness, Vickers	349	+13
Tensile Strength, Ultimate	950 MPa	-8
Tensile Strength, Yield	880 MPa	-
Elongation at Break	14 %	+4
Reduction of Area	36%	-10
Modulus of Elasticity	113.8GPa	-8
Compressive Yield Strength	970 MPa	+5
Notched Tensile Strength	1450 MPa	+1
Ultimate Bearing Strength	1860 MPa	e/D = 2
Bearing Yield Strength	1480 MPa	e/D = 2
Poisson’s Ratio	0.342	-

Charpy Impact	17J	V-notch
Fatigue Strength	240 MPa	At 1E+7 cycles. K_t*= 3.3
Fatigue Strength	510 MPa	Unnotched 10,000,000 Cycles
Fracture Toughness	75 MPa-m½	-
Shear Strength	550 MPa	Ultimate shear strength

*K_t = Stress concentration factor.

Table 2.2: Thermal properties of Ti-6Al-4V [1996Joh]

Properties	Metric	Comment
CTE, linear 20ºC	8.6 µm/m-°C	20-100ºC
CTE, linear 250ºC	9.2 µm/m-°C	Average over the range 20-315ºC
CTE, linear 500ºC	9.7 µm/m-°C	Average over the range 20-650ºC
Specific Heat Capacity	0.5263 J/g-°C	-
Thermal Conductivity	6.7 W/m-K	-
Melting Point	1604 - 1660°C	-
Solidus	1604°C	-
Liquidus	1660°C	-
Beta Transus	980°C	-

2.1.1 Advances in Titanium Alloy Machining

In 1990, titanium alloys were described as difficult to machine materials because of the high tool vibration, high cutting temperature, high cutting forces and short tool life associated with its machining [1990Mac]. High temperature concentration at tool tip during titanium alloy machining promotes diffusive wear of cutting tool inserts [1990Mac, 2005Cap]. The thermal-mechanical instability of titanium alloys results in segmented chip formation with adiabatic shear band which limits machinability [1990Mac, 2005Cap]. The appropriate use of coolants during Ti-6Al-4V machining can reduce/eliminate the poor heat dissipation associated with its machining. [1985Asm]. Sharp cutting tool edges are recommended when machining titanium alloys as they eliminate seizing and galling effects which promotes premature tool failure [1985Asm, 2005Grz]. The machinability, machining cost and surface integrity of titanium alloys can be improved if the right combination of cutting tools, cutting conditions and machine tools are selected [1985ASM, 2005Grz].

2.2 Milling

Milling is a high speed material removal process in which rotary cutters are used to remove material from a workpiece by advancing in a direction at an angle with the axis of the tool [2000Tre]. This is accomplished by either spinning a cutter with many teeth at high speed towards the workpiece, or advancing the material towards the cutter, and/or using a combination of both approaches [2013Ush]. Milling operations can generally be divided into face milling and end milling (Figure 2.1[a] and Figure 2.1[b]) [2009Sch]. Face milling also known as "intermittent cutting action" is a milling technique used for surface level machining, and depending on the orientation of the axis of rotation of the 45^{o} cutter relative to the cutting plane, it can be considered as horizontal and vertical face milling [2009Sch]. End milling on the other hand refers to milling operations where flat bottomed cutters are used for machining at an axis vertical to the workpiece [2009Sch]. In manufacturing operations the face milling technique is usually recommended for longer tool life and better surface quality [2014Kum]. This is because small depth of cut used during face milling as well as the full engagement of the cutter which keeps the forces on either side of the centreline balanced, furthermore the chips during face milling are started out at a zero thickness [2014Kum]. Thus face milling technique was selected for this investigation.

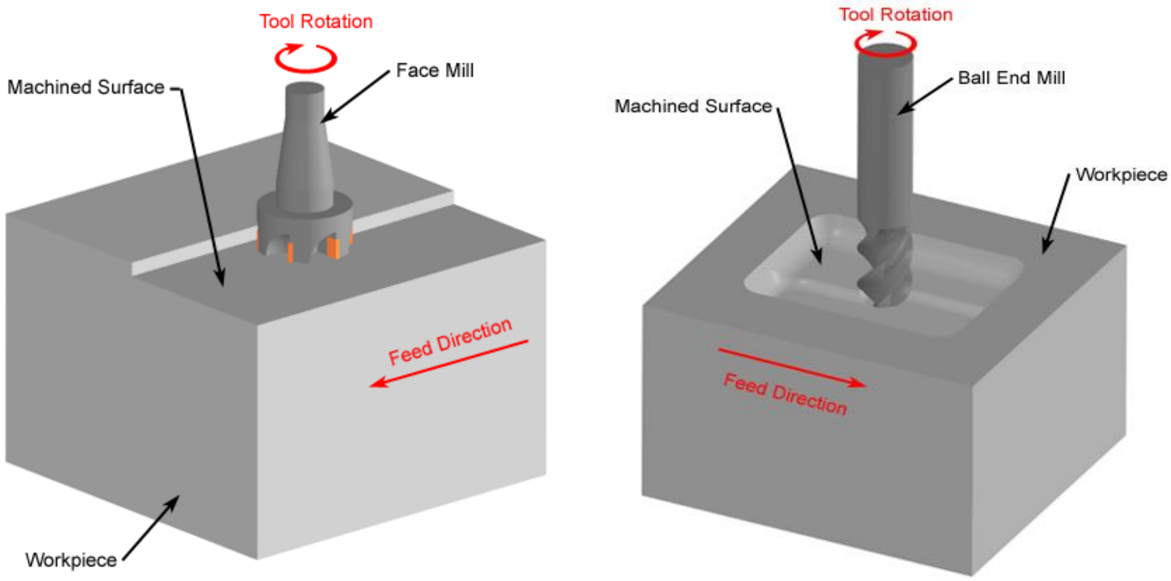

(a) (b)

Figure 2.1: Representation of milling operations: (a) Face milling, (b) End milling [2009Url]

2.3 Milling parameters

During milling operations, the following cutting parameters are usually taken into consideration; cutting speed (v_c), feed rate (v_f), axial depth of cut (a_p), radial depth of cut (a_e), and material removal rate (MRR). A proper understanding of these parameters is important for improving any milling process.

2.3.1 Cutting Speed

The cutting speed (v_c) is the cutting edge tangential peripheral velocity measured in m/min [2005Yan]. It is the speed difference between the cutting tool and the surface of the workpiece it is operating on [2008Smi]. In any machining operation, the selection of an appropriate cutting speed is of key importance as this influences the resultant forces and temperature [2005Yan]. Cutting speed can generally be calculated using Equation 2.1.

$$v_c = \frac{\pi N D}{1000} \qquad \text{Equation 2.1}$$

Where N is the spindle speed in rpm and D is the tool diameter in mm [2005Yan].

The cutting speed is usually varied to suit different combinations depending on the application and nature of the cutting tool insert [2013Ush]. Lower cutting speeds, which permit for increased cutting depth, are used for roughing operations where high material removal rate is of primary interest [2013Ush], while higher cutting speeds are recommended for finishing operations where increased productivity and surface quality of the machined part are of interest [2013Ush]. This is because at higher cutting speeds, milling temperatures are elevated and the strain hardening effect is eliminated owing to the thermal softening and ductility of the workpiece material [2008Smi]. Cutting speeds may also be adjusted based on chip shape and colour, rigidity of work holding, and machine horsepower meter readings [2004Dud]. In the past, the cutting speed for machining titanium ranged from 18 to 30 m/min, until recent when cutting speeds exceeding 300m/min were attainable with enhanced cutting tool materials [1998Cha, 2008San].

2.3.2 Feed Rate

Feed rate (v_f) is the velocity at which the cutter is fed into the workpiece [2008Smi]. The selection of feed rate is dependent on the tool types, surface finish, power available at the spindle, tooling setup and rigidity of the machine, work-piece material strength and work-piece material machinability [1953Coo]. For milling machines where multi-tipped/multi-fluted cutting tools are utilized, the feed rate is usually dependent on the number of teeth on the cutter in addition to the desired amount of material per tooth to cut [2008Smi]. The greater the number of cutting edges, the higher the feed rate permissible for a cutting edge to work [1953Coo]. Increasing the feed rate during machining increases the machining forces [1989Mac]. The increase in machining forces is owing to the increased level of engagement between the cutter and workpiece [1989Ken]. A general formula for calculating the feed rate during milling is given in Equation 2.2 below [1953Coo].

$$V_f = f_z Z N \qquad \text{Equation 2.2}$$

Where: V_f = feed rate (m/minute); f_z = feed/tooth (mm/tooth); Z = number of teeth, and N = spindle speed (rpm or mm/minute) [1953Coo].

2.3.3 Depth of Cut

The depth of cut describes the thickness of the work piece material that is to be removed by the cutting edge during machining [2010Get]. The "depth of cut" during milling is represented by two parameters, the axial depth of cut (a_p) and the radial depth of cut (a_e) (Figure 2.2) [1993Saw]. Depending on the axis of orientation, both parameters indicate the level of engagement of the cutting tool into the workpiece [1993Saw]. An increase in depth of cut increases the cutting [1993Saw]. This could be because the tool cuts through more material and therefore requires more cutting force to do so.

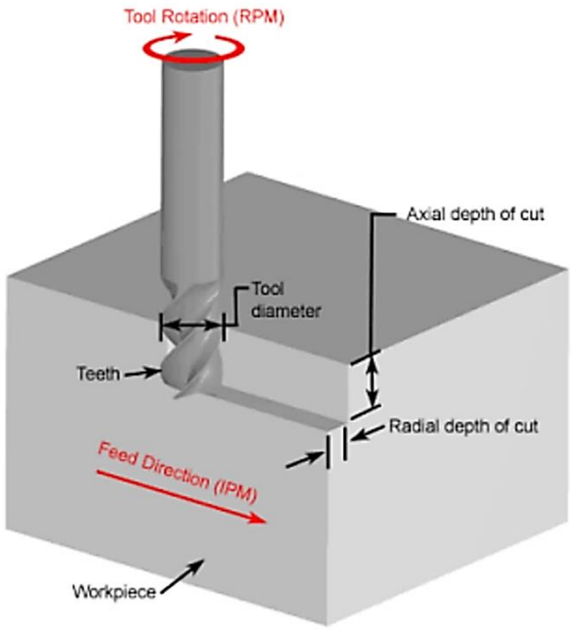

Figure 2.2: Representation of axial and radial depths of cut [2009Url]

2.3.4 Material Removal Rate

Material removal rate refers to the volume of material removed or machined per time unit [1993Saw]. Material removal rate is usually high for roughing operations and low for finishing operations [1993Saw]. This is because of the variation in depth of cut for roughing and finishing operations [1993Saw]. The material removal rate is measured in mm^3/min and is calculated using Equation 2.3 below [1993Saw].

$$MRR = \frac{a_p \, . \, a_e \, . \, v_f}{1000} \qquad \text{Equation 2.3}$$

Where a_p= axial depth of cut, a_e = radial depth of cut, and v_f = feed rate.

2.4 Cutting tool inserts

Cutting inserts are usually made from materials which are at least three (3) times harder or tougher than the material which is to be cut, also the tool must be able to withstand the heat generated during the metal cutting process [1997Sie]. Some industrially accepted cutting tool materials are shown in Table 2.3. Cutting tool materials with high stability, high abrasion resistance and high hardness are usually recommended for machining Ti-6Al-4V since it reacts with most cutting tool materials resulting in short tool life [1953Coo, 2009Ibr]. Several cutting tool materials have been developed for machining titanium to improve its machinability. These tools include coated carbides, uncoated carbides, ceramics and diamond tools.

Cutters made from cemented carbides are widely used in a range of tribological applications such as cutting, milling, metal forming, drilling and turning due to their good combination of mechanical properties such as hardness and wear resistance [2013Gen[b]]. The performance of a cutting tool insert is usually dependent on the tool geometry [2009Asm]. The ISO and ANSI Standards for tool geometry acknowledge two systems of cutting tool geometry, namely; the tool-in-hand and, the tool-in-use systems [1997Ste]. The choice of a particular system or combination of systems depends on the tool holder, tool post design, tool fixing in the machine, and direction of the tool motion with respect to the workpiece or axis of rotation [1997ste].

Table 2.3: Cutting Tool Materials [1997Ste, 2009Sch]

Tool Material	Properties	Applications
Cermets	• Stable. • Extremely high resistance to abrasion. • Hardness up to HRC 95.	• Used for making turning tool bits.
Diamond	• Stable. • High resistance to abrasion. • Superior hardness.	• Mostly used for machining abrasive materials. • Used for coating tools.
Cubic Boron Nitride (CBN)	• Stable. • Extreme hardness. • Hardness higher than HRC 95.	• Used for making turning tool bits. • Extensively used for hard machining.
Cemented carbides	• Stable. • High resistance to abrasion. • Hardness up to HRC 90.	• Used for making milling cutters and saw blades.
Ceramics	• Stable. • Fragile. • Hardness up to HRC 93.	• Used almost exclusively on turning tool bits.
Cast Cobalt Alloys	• Stable. • Fragile. • Hardness up to HRC 65.	• Rarely used since it does not permit for high speed machining.

The surface of the cutting tool inserts onto which the chips are formed during cutting process is known as the “rake” or “chip face” of the insert (Figure 2.3), while the side of the cutter is known as the “flank” [2008Bon]. For enhanced tool life, a chip breaker geometry (or a chip groove) is usually manufactured on the cutting tool rake surface, so as to obstruct the flow of continuous chips by breaking them into pieces [2008Bon]. Obstructing the flow of continuous chip reduces the cutting pressure and produces chips which can easily be evacuated [2012Joe]. The surface finish and dimensional accuracy of machined surface are also improved with the obstruction of continuous chip [2012Joe].

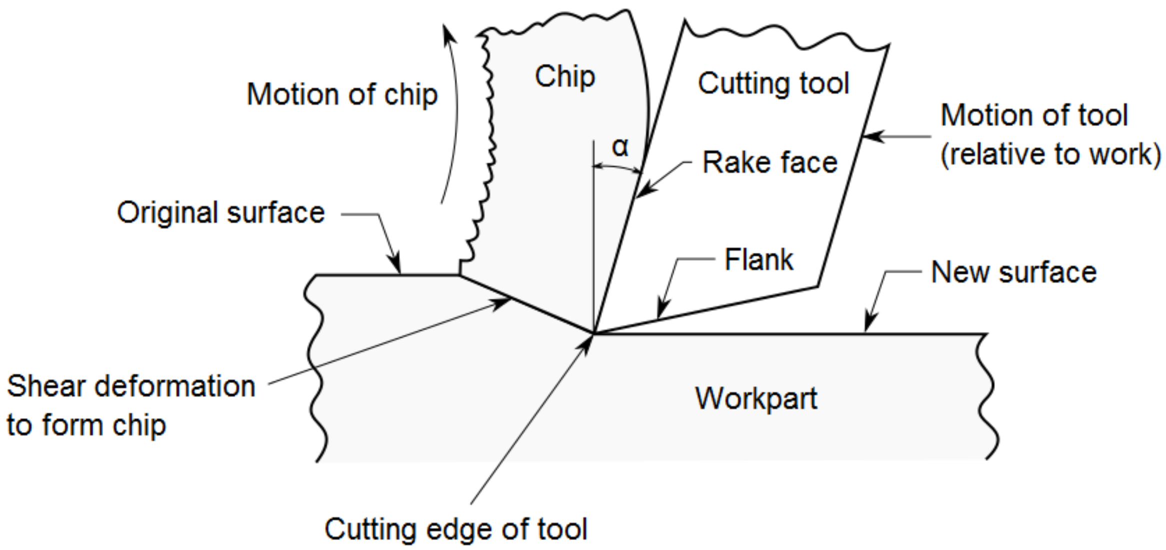

Figure 2.3: A schematic showing the geometry of a cutting tool insert [2015Url[b]]

2.5 Cemented carbides

Cemented carbides (Cermets) are composite materials containing hard tungsten carbide grains and ductile metal binder matrix of either cobalt or nickel [2011Kar, 1995Spr]. They are widely used in a range of tribological applications due to their hardness, toughness, wear resistance and strength [2013Gen[a]]. Cermets are usually manufactured by powder metallurgy, with their mechanical properties serving as criteria for performance [2011Kar, 2000Chi]. These properties are dependent on the composition (constituents and their relative amounts), the size distribution of the tungsten carbide grains after sintering, as well as the type and amount of binder metal [2001Che]. The densification, hardness, and fracture toughness are mechanical properties of cemented carbide to be considered in this study.

2.5.1 Densification

Densification or specific gravity of a cemented carbide is the weight per unit volume of that cemented carbide measured in grams per cubic centimeter (g/cm^3). The densification of cemented carbide which is through the elimination of porosity during sintering, indicates the effectiveness of the sintering process [1991Jen]. To accurately measure the density and open porosity of samples, the true volume of sample, true density of sample, and the volume of open porosity of the sample are required [1991Jen].

2.5.2 Hardness

Hardness is a characteristic of a solid material expressing its resistance to permanent deformation, it is a measure of the resistance of a material to surface indentation or abrasion [1996Exr, 2010Get]. The hardness of a cemented carbide which is measured using either the Rockwell or Vickers scale gives an indication of its composition and microstructure [1975Bro, [1996Exr]. Hardness is primarily a function of composition and grain size [1996Exr]. Carbides with high binder metal contents and coarser tungsten carbide grain sizes produce lower hardness values, while those with low binder contents and fine grain sizes produce high hardness values [1996Exr]. The hardness of a cemented carbide material is usually directly proportional to its abrasive wear resistance [1996Exr].

2.5.3 Fracture toughness

Fracture toughness is a measure of resistance of a material to failure from fracture from a pre-existing crack [2010Get]. Brittle materials tend to have low fracture toughness, while ductile materials tend to have high fracture toughness [1995Her]. Materials with high fracture toughness undergo ductile fracture [1995Her]. Brittle fracture is however very characteristic of materials with less fracture toughness [1995Her]. Fracture toughness is generally inversely related to hardness, and increases with increased binder mean free path [1984War]. At elevated temperatures, the fracture toughness of materials does not vary significantly until about 600^{o}C – 700^{o}C where it increases [1984War].

2.5.4 Transverse rupture strength

Transverse Rupture Strength (TRS) is a measure of the tensile strength of a cemented carbide in a three point bending test performed on standard rectangular bars [2000Hod]. It is a combination of shear strength, compressive strength and tensile strength, and hence used as a general measure for toughness of WC-cemented carbides [1963Gur]. The transverse rupture strength of a material determines the maximum energy that material can absorb before actual fracture or failure takes place [1963Gur]. Cements having relatively high TRS values are generally applied where shock, impact, or failure by breakage are dominant [2000Hod].

2.6 Cutting Tools Production Techniques

Sintering is a processing technique used to produce density-controlled materials from metal or/and ceramic powders by applying thermal energy [2005Kan]. When this energy is applied to a powder, two basic phenomena occur, densification (without or with shrinkage) and grain growth [2005Kan]. The benefits of sintering cutting tool materials include; uniform porosity, uniform starting materials, high strength, high purity, and improved mechanical properties

[2009Ger, 1975Luy]. The sintering techniques used in this study are liquid phase sintering (LPS), and spark plasma sintering (SPS) techniques.

2.6.1 Liquid phase sintering

Liquid phase sintering is the process of forming high performance components from powders under conditions where solid grains coexist with a wetting liquid [2008Ran]. This process involves adding an additive to the powder which will melt before the matrix phase [2005Kan]. During liquid phase sintering particles are bonded together, leading to higher strength at the same time low porosity decreased [2011Kar]. The mechanism for Liquid phase sintering includes; particle rearrangement, solution-precipitation and Ostwald ripening grain growth stages that usually overlay [2002Pet]. Final shapes of metallic powder are usually consolidated by liquid phase sintering [1984Kay]. This is because the resulting mechanical and physical properties of the shapes become superior owing to low sintering temperatures, fast densification, and high density [1984Kay]. Nevertheless, the long sintering time and inhomogeneous structure owing to WC grain growth (Ostwald ripening) is a major limitation during liquid phase sintering [2008Hua].

2.6.2 Spark plasma sintering

Spark plasma sintering (SPS), also known as a pulse electric current sintering (PECS), is a sintering technique which employs high heating rates combined with high compressive pressure to consolidate powder compacts to a high density in a short time [1999Tok]. Spark plasma sintering is widely used in the production of functionally graded materials, as well as for bonding dissimilar materials [1999Tok]. This is because the high degree of densification, owing to the short sintering and low temperature results in fine carbide grains and enhanced hardness of the material produced [1999Tok, 2006Son].

2.7 Tool Wear and Tool Life

Tool wear generally describes the gradual failure of a cutting tool insert due to regular operation [2012Jin]. The productivity and economy of manufacturing by machining is significantly influenced by the life of the cutting tool insert [2011Ali]. During milling process, the cutter removes parts of the workpiece by a process of intense plastic deformation at a high strain rate within the primary and secondary shear zones. Thus, tool face is subjected to high temperature and pressure resulting in wear (Figure 2.4) [2002Bra]. Although different modes for tool failure exist, the gradual degradation (gradual wear) of a cutting tool insert owing to regular operation is the only accepted mode in the machining industry [2012Jin, 1995Hen]. This is because it makes it possible to schedule tool replacements and also find optimum cutting parameters relative to production cost [1995Hen]. Catastrophic tool failure is an undesirable failure mode which is unpredictable, usually resulting in work piece damage and cause downtime [1996Qui].To ensure an economic viable solution the tool life for milling Ti-6Al-4V should currently be at least 30 minutes (SRT) [2010Get]. Depending on the failure mechanism, wear may either be termed as adhesive, chemical or abrasive wear [2012Jin]. Abrasive wear is the most common type of wear in milling operation [1976Rud]. It is caused by the combined action of chips sliding on the rake face of the tool and also by the friction phenomenon between the tool flank and the work piece [1976Rud]. The failure and wear of cutting tools are more evident during milling at higher cutting speeds [1984Mye]. This is because of the high chemical reactivity resulting from higher cutting temperatures [1984Mye]. At lower cutting speeds tool wear and failure still exist in the form of mechanical wear [1984Mye]. The cutting speed is the most influential parameter on tool life, followed by feed rate and then depth of cut [1993Hon]. Increasing the cutting speed during machining usually increases the cutting temperature, which results in decreased hardness of the tool material, hence facilitating wear [1993Hon].

Wear may also result from mechanical breakage or plastic deformation of the cutting edge [2013Cha]. The breakage of the cutting edge is normally due to excessive forces and shocks on the cutting tool, while the plastic deformation of the cutting edge is usually because of the intensive transfer of stresses and temperature to cutting edge [2013Cha]. For cemented carbide tools wear is perceptible at elevated temperature, when the hardness, plastic modulus and fracture toughness of the carbide tools decreases due to increased thermal stresses on the cutting tool insert [1983Ree]. Wear in cutting tool inserts can generally be summarised into flank wear and crater wear depending on the location and causes [2012Jin] (Figure 2.4). Flank wear (VB) occurs in tools as a result of high frictional coefficient between the machined surface of the workpiece and the tool flank, while crater wear occurs as a result of the chemical reaction between the workpiece material and the cutting tool insert, or as a result of change in temperature (hot to cold) of cutting edges [2012Dra, 2014Kum]. Nevertheless, Crater wear may also occur as a result of chip sliding over the tool face [2012Par]. Cutting forces usually increase with increase in flank wear, however if flank wear exceeds a critical value (> 0.6mm), the excessive cutting force results in tool failure [2012Dra, 2012Ije].

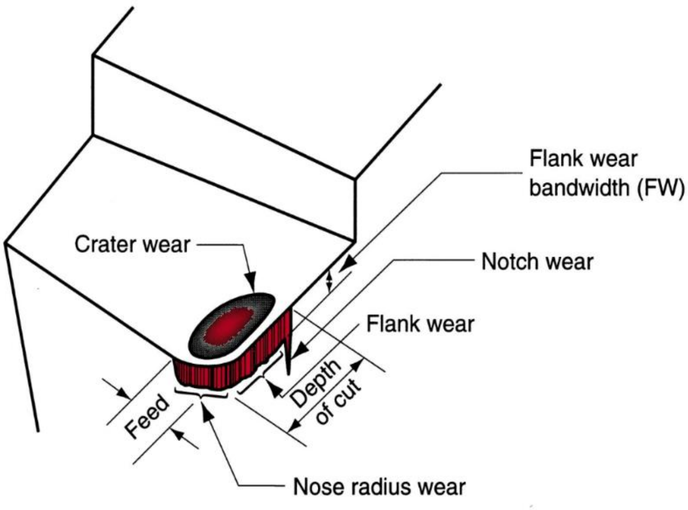

Figure 2.4: Worn cutting tool, showing the principal location of flank wear and crater wear [2013Akh]

When machining extremely hard materials at lower cutting speeds machining forces are usually increased due to low temperatures and built up edge (BUE) formation [2005Yan]. However at a higher cutting speed, the magnitude of the cutting force decreases due to thermal softening of the workpiece, hence improving the eliminating BUE formation and improving surface roughness [2004Dud]. On the contrary, the elevated temperatures associated with higher cutting speed can also result in build-up of compressive stresses near the tool edge resulting in an accelerated flank wear rate of the cutting tool insert [2004Dud].

2.7.1 Influence of milling parameters on tool life

The influence of milling parameters on tool life is illustrated in Figure 2.5 below. The most influential parameter on tool life is the v_c followed by the a_e and f_z respectively (Figure 2.5). The a_p has the least influence on tool life (Figure 2.5).

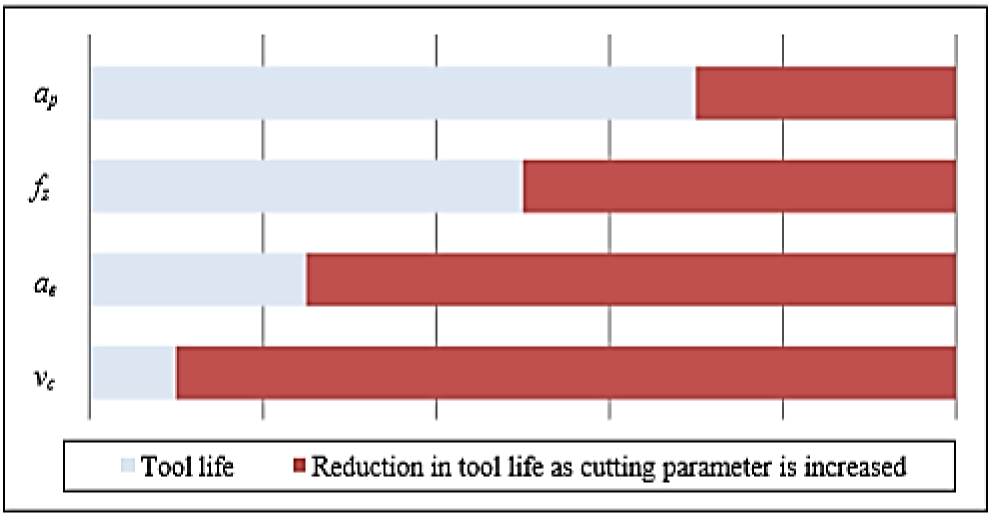

Figure 2.5: Influence of milling parameters on tool life [2007San]

2.7.2 Effect of built-up edge on tool wear

Built-Up Edge (BUE) is defined as a cap of work hardened material attached to the rake face of a metal cutting tool [1970Ram]. When the coefficient of friction is high, a bond between the tool and the chip may occur to initiate the built-up edge [1970Ram]. The generation of

(BUE) on the cutting tool edge during machining affect the tool in various ways, sometimes decreasing the tool life (adhesive wear) or sometime increasing it [1993Saw]. The formation of BUE is usually evident when machining materials possessing high strength and stiffness at a lower cutting speed and feed. The effect of BUE usually decreases the cutting forces as the cutting speeds increase, until a minimum force is attained (figure 2.6) [1966Zor]. Furthermore, the formation of built-up edge (BUE) and adhesive layers degrades the shape and efficiency of a cutting tool, as well as the surface quality and dimensional accuracy of the finished product [1966Zor].

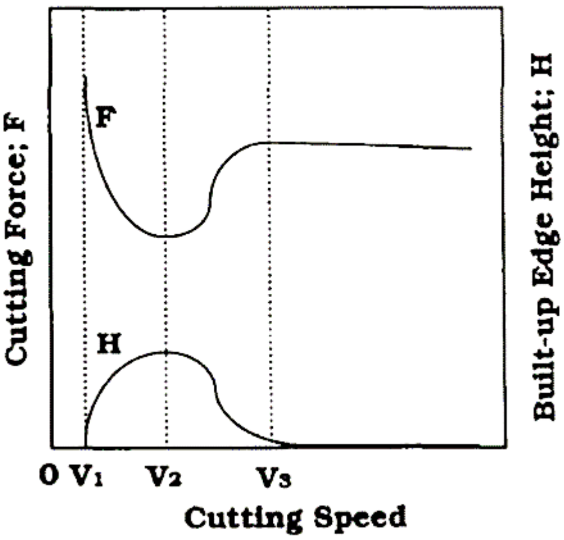

Figure 2.6: Diagram showing the typical influence of cutting speed on cutting force with built-up edge [1966Zor]

2.8 Cutting Fluid

During machining cutting fluids are used for three main functions; cooling, lubrication and chip disposal [2004Ina]. The cooling effect of cutting fluids prevent distortion of the tool geometry by stabilizing thermal conditions, while the lubricating effect prevents sticking (a phenomena whereby chips become welded to the tool face during machining thereby increasing cutting resistance) [2004Ina]. Cutting fluids also enhance chip disposal by flushing away chips from the tool-workpiece interface thereby ensuring the tool is always exposed to a clean cutting surface [2004Ina]. Most cutting fluids are made from petroleum distillates, animal fats, plant oils, water and fats, and are usually available commercially as oil, oil-water emulsions, paste, gels, and mist, with their effectiveness largely depending on their composition and method of application [2015Wil]. The different conditions for cutting fluid applications include flood coolant (wet machining), near - dry machining and the dry machining [2009Sch]. Nevertheless, the application of cutting fluids in machining is usually accompanied by a number of drawbacks. The cutting fluids used for machining represents 16–20% of the manufacturing costs, also most cutting fluids pose health risks to operators (2008Ast). The disposal of used cutting fluid is still a major challenge (2008Ast). In an attempt to reduce machining cost, environmental pollution, and health hazards, global industrial trends are leading away from wet machining operations to near-dry machining (MQL) and dry machining [2008Ast].

2.8.1 Dry machining

Dry machining can be considered as any machining operation which is carried out without the application of cutting fluid [2000Sre]. It is ecologically desirable and reduces significantly machining costs. Dry machining increases milling temperature resulting in rapid tool failure and increased workpiece thermal residual stresses [2000Sre]. The high temperatures generated at cutting zones during dry machining at high speed, lower the flow of stress in the cutting material, resulting in lesser cutting forces being required for machining [2000Sre]. Adhesion occurrence on the major flank face at low cutting speeds is particular in dry machining [1999Fri]. During dry machining, increasing the cutting speed extends adhesion to the minor flank face, and subsequently, to the rake face at the major cutting edge, resulting in inaccuracy in geometry and shape of the machined parts [1999Fri, 2007Kor].

2.8.2 Minimum Quantity Lubrication

Minimum Quantity Lubrication (MQL) is a cutting fluid technology that reduces the amount of applied lubricant during machining to a minimum optimized level (only a minute amount typically of a flow rate of 50 to 500ml/hour) [2004Wei]. It involves controlled application of atomized fine droplets of high-pressure air stream and cutting fluid on the tool-workpiece interface in order to generate lubricating and cooling effects [2000Sre]. A schematic representation of an MQL unit is shown in Figure 2.7. The application of MQL does not only reduce the temperature in the tool-workpiece interface, but also changes the contact stress and frictional coefficient at the tool-chip interface resulting in reduced cutting forces, residual stresses and surface roughness [1998Chi]. Furthermore, it prevents environmental pollution and improves the machinability characteristics [2004Wei]. The utilization of MQL provides a neat, clean and dry working area, avoiding inconvenience and health hazards due to heat, smoke, fumes, gases, etc. [2004Wei]. At lower cutting speeds the application of MQL eliminates thermal stresses, resultant forces and built-up edge formation on the tool to workpiece interface [1998Chi]. It also provides extra oxygen which promotes the formation of a protective quaternary Ti-6Al-4V oxide which acts as diffusion barriers between the chips and the tool interface [1998Chi].

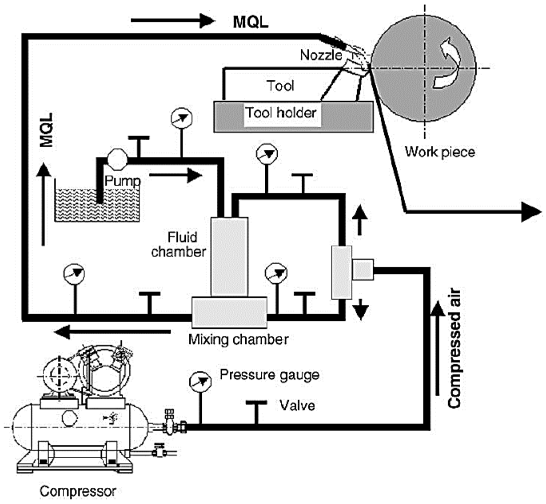

Figure 2.7: Schematic representation of a minimum quantity lubrication unit [1998Chi]

In a milling experiment by Liao et.al using NAK80 hardened steel under high speed end milling condition, it was observed that the application of MQL significantly reduces cutting temperature resulting in higher resultant force [2007Lai]. However, as the cutting speed was increased, the application of MQL significantly reduces cutting force [2007Lia] (Figure 5.28). This shows that the cutting speed influences the milling temperature and forces during MQL milling [2007Lia].

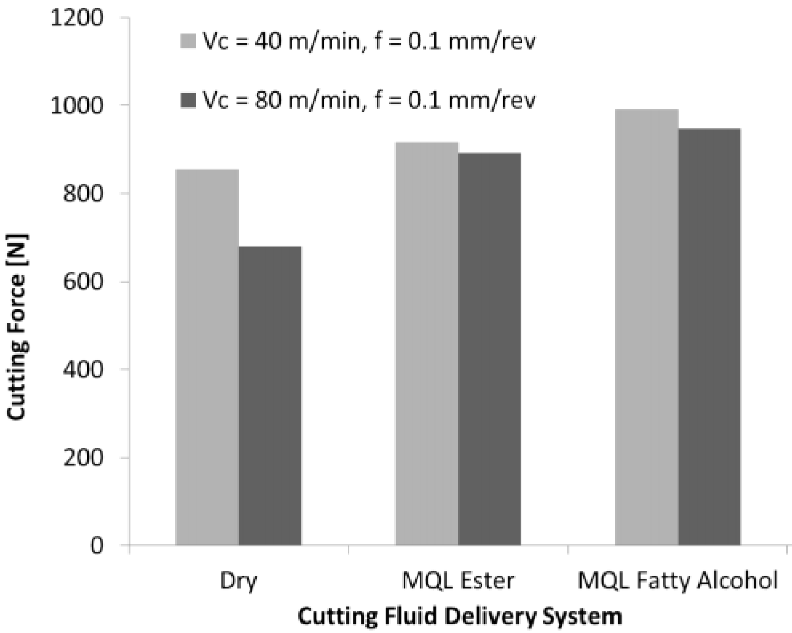

Figure 2.8: Cutting forces with respect to cutting fluid delivery system and cutting speed [2007Lia].

The experimental results from Liao et.al also revealed that depending on the cutting parameters, the application of MQL can increase tool insert life by four times [2007Lia]. This reflects a significant reduction in cutting tool cost. Although the extent to which MQL influences tool life is dependent on the cutting parameters, mechanical properties of the cutting tool material and the extent of its application, an optimum effect of MQL can be obtained by positioning the nozzle relative to the feed direction [1998Chi].

2.9 Surface Integrity

Surface integrity is the sum of all of elements describing the conditions existing on the surface of a machined material [1970Kos]. It can also be said to be the surface condition of a workpiece after being modified by a manufacturing process [2003Pau]. The quality of a machined component is usually evaluated with respect to how closely it adheres to set product finish parameters, and relative properties [2011Ali]. The dimensional accuracy, tool wear and surface quality are three factors to be considered if an optimum surface integrity is to be achieved [2011Ali]. The manufacturing processes, type of cutting tool and cutting conditions dictate the type of surface that will be produced [1964Fei, 1970Fei]. Poor surface finishing affects the life and functionality of machined component to which it applies [2002Bra]. The integrity of a surface in general is divided into two categories, namely surface topography characteristics and the subsurface layer characteristics [2003Pau]. The surface topography characteristics describe the roughness, waviness, error of form, flaws, and lay or texture of the outermost layer of a sample, while the subsurface layer describes the residual stresses and microstructural alterations [2003Pau].

2.9.1 Surface Roughness

Surface roughness is one distinctive characteristics of surface topography which is quantified by the deviations in the direction of the normal vector of a real surface from its ideal form [2008Gao]. If these deviations are large, the surface is rough, and if they are small, the surface is smooth [2008Gao]. A detailed overview for surface roughness can be seen in Figure 2.9. The roughness height determines the height of irregularities in the surface, while the roughness width defines the nominal distance between successive peaks which constitutes the predominant roughness pattern [2008Gao]. The lay represents the predominant direction of surface pattern produced on the machined surface, and it also reflects the type of machine operation used [2008Gao]. The roughness-width cutoff is the greatest spacing of the respective surface irregularities, any irregularity outside this cutoff value is termed waviness [2008Gao]. Table 2.4 shows some features of surface roughness and their potential causes.

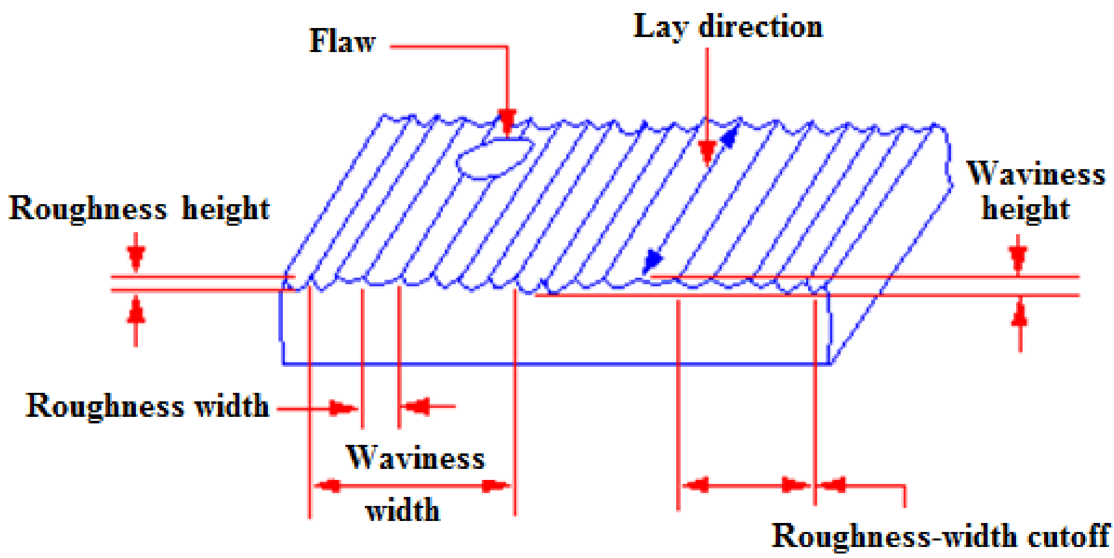

Figure 2.9: Surface roughness overview [2009Gao]

Table 2.4: Features of surface roughness and potential causes [2012Sad]

Surface feature	Cause
Form errors (flatness, roundness, straightness, cylindricity, etc.)	• Errors of machine tool slides, • Elastic deformations, • Erroneous fixation of tool or work piece, • Severe tool wear.
Cracks	• Tool-nose wear, • Built-up-edge formation, • Mode of chip formation, • Galvanic procedures.
Waviness	• Eccentric rotation of work piece or tool, • Vibrations in the Manufacturing system. • Tool wear, • Inhomogeneity of processed material.
Grooves	• Tool edge form, • process kinematics, • chip morphology

Different specialized techniques can be employed in analyzing the surface topography of a material. The selection of a particular technique or combination of techniques is dependent on the surface area of interest [2012Sad]. Table 2.5 shows the common techniques which can be employed in observing/analyzing surface integrity. Surface topography can be measured using a profilometer and laser confocal microscopy [2012Sad]. A profilometer measures variations in surface feature as a function of position using a diamond stylus which runs perpendicular to the direction of the lay of the surface topography [2012Sad].

Table 2.5: Techniques for observing surface topography [2012Sad]

Areas of Interest	Common Techniques	Identifiable defects
Surface Topography	• Profilometry, • Confocal microscopy, • Optical microscopy, • Interference microscopy, • Electron microscopy, • Metrology.	• Surface profile, • Surface roughness, • Waviness, • Lay, • Surface defects, • Distortion.
Surface Chemistry	• Laser probe mass spectrometry, • X-ray spectroscopy, • Auger spectroscopy, • X-ray microprobe analysis, Transmission electron microscopy.	• Surface composition.

The laser confocal microscopy is a more advanced technique which measures the surface topography of a material using a laser light which is passing through the confocal optical path for image formation [2012Sad]. During roughness measurements the basic parameters of interest are the average height (R_a), the root mean square (R_q), and the maximum height (R_z). R_a is the average height of all the peaks within a sample length on a surface (Figure 2.10(a)), and it can be calculated using Equation 2.4 [2015Url[c]].

$R_a = \frac{1}{i}\int_0^1 \mid Z(x) \mid \, dx$ Equation 2.4

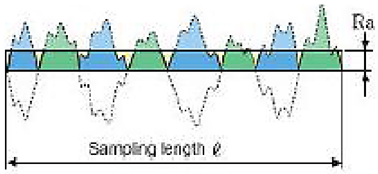

Figure 2.10(a): R_a [2015Url[c]]

R_q is the root mean square that corresponds to R_a (Figure 2.10(b)), which is calculated using Equation 2.5 [2015Url].

$R_q = \sqrt{\frac{1}{i}\int_0^1 \mid Z^2(x) \mid \, dx}$ Equation 2.5

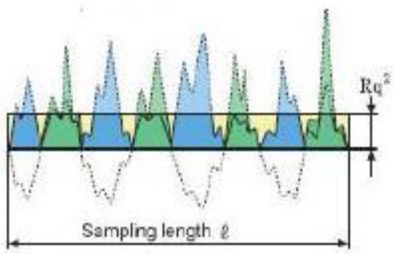

Figure 2.11(b): R_q [2015Url[c]]

R_z is the result obtained by adding the maximum height to the maximum depth for a given sample length. These values are obtained from the datum which is set at the point R_a.R_z (Figure 2.10(c)) is calculated using Equation 2.6 [2015Url].

$R_z = R_p + R_v$ Equation 2.6

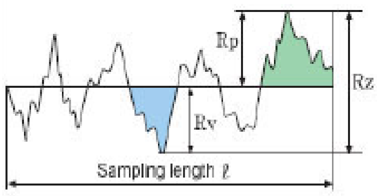

Figure 2.12(c): R_z [2015Url[c]]

2.9.2 Residual Stress

Residual stresses are those stresses existing in a material without the application of any service or external load [2011Url]. These stresses are mostly caused by manufacturing and fabrication processes such as milling, rolling, welding, etc. [2011Url]. During milling operations the resultant residual stress correlates closely with the cutting parameters [2012Wan].

Residual stresses can also be generated in a material after mechanical and thermal loading or phase changes [2000Wit]. The knowledge of the residual stress state of a material is important to determine the actual stresses experienced by the material, thereby explaining or preventing its failure [2000Wit, 2011Url]. The residual stresses in a material may either be compressive or tensile [2013Sha]. Compressive residual stress usually acts by pushing the material together. This is beneficial at surface level, as it increases fatigue strength and fatigue life [2013Sha]. On the other side, tensile residual stress pulls the material apart leading to decreased fatigue strength and fatigue life of the workpiece component [2013Sha]. Residual stresses can be characterized by the magnitude at which they exist within a material. Stresses that occur over long distances within a material are referred to as macro-stresses, while stresses that exist only locally (either between grains or inside a grain) are called micro-stresses [2004Bal].

All residual stress measurement techniques can be categorized into three types: Non-destructive, Semi destructive and destructive [2005Fit[a]]. This categorization is based on how much, if any, material must be removed from the surface of interest to carry out the process of measurement. Techniques such as x-ray diffraction are non-destructive while sectioning is semi destructive. Deep-hole drilling is a destructive technique [2012Hit]. Table 2.6 lists the advantages and limitations of the various residual stress measurement techniques. Cold working techniques such as laser shock peening, ultrasonic peening, hammering, and burnishing, likewise hot working techniques such as heat treatment and controlled cooling may be used to introduce residual stresses [2006Mce].

Table 2.6: Residual stress measurement techniques [2011Ros]

Technique	Advantage	Disadvantage
X-ray diffraction	• Ductile, • Generally available Wide range of materials Hand-held systems, • Macro and Micro RS.	• Lab-based systems, • Small components, • Only basic measurements.
Hole Drilling	• Fast, • Easy use, • Generally available Hand-Held, • Wide range of materials.	• Interpretation of data, • Semi destructive, • Limited strain sensitivity and resolution.
Neutron Diffraction	• Macro and Micro RS, • Optimal penetration and Resolution, • 3D maps.	• Only specialist facility, • Lab-based system.
Barkhausen Noise	• Very quick, • Wide sensitive to microstructure effects especially in welds, • Hand-held.	• Only ferromagnetic Materials, • Need to divide the microstructure signal from that due to stress.
Ultrasonic	• Generally available, • Very quick Low cost. • Hand-held.	• Limited resolution, • Bulk measurements over whole volume.
Sectioning	• Wide range of material, • Economy and speed, • Hand-held,	• Destructive, • Interpretation of data, • Limited strain resolution.
Contour	• High-resolution maps of	• Destructive,

	the stress normal to the cut surface Hand-held, • Wide range of material, • Larger components.	• Interpretation of data, • Impossible to make successive slices close together.
Deep hole drilling	• Deep interior stresses Measurement, • Thick section components, • Wide range of material.	• Interpretation of data • Semi destructive, • Limited strain sensitivity and resolution.

2.10 Approach to Study

Using the information gathered from the literature survey, the first part of this study was to identify the effect of binder matrix alteration and sintering techniques on the mechanical properties of the cemented carbide inserts used for the machining operation.

The second part of this study was to identify promising machining parameters for rough milling and finishing of Ti-6Al-4V. These basically referred to conditions were lower resultant forces, temperatures and flank wear rates were experienced.

The third part of this study involved identifying milling parameters and lubricating conditions under which optimum surface integrity was achieved for the Ti-6Al-4V samples.

Chapter 3 : Experimental Procedures

This chapter gives detailed description of the experimental procedures, apparatus and facilities used for this research. A general illustration of the experimental processes are shown in Figure 3.1.

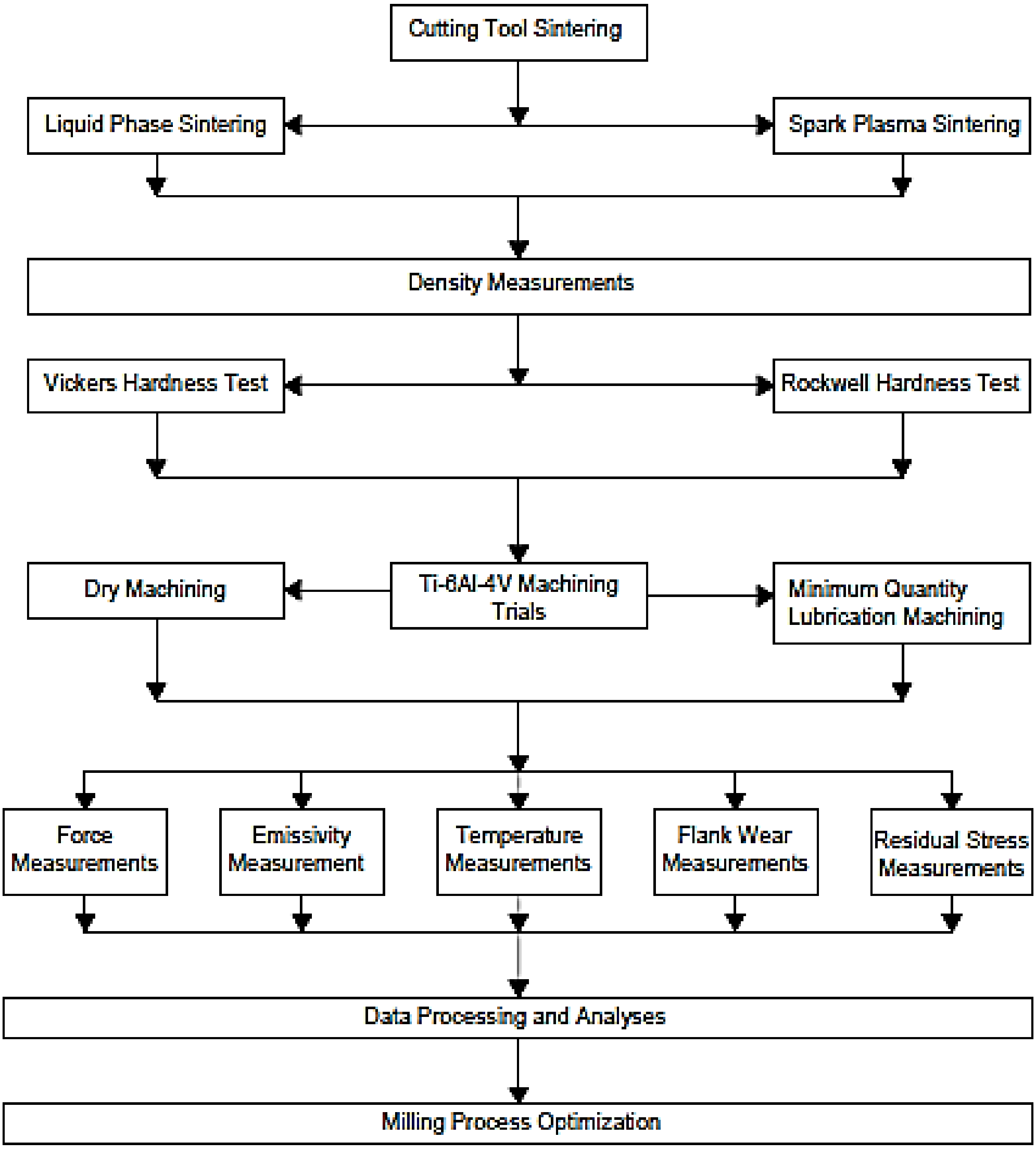

Figure 3.1: Illustration of experimental processes

3.1 Sintering

Eight innovative cutting tool inserts were produced using both liquid phase sintering and spark plasma sintering techniques, under conditions shown in Table 3.1. The finished inserts were then used for machining the Ti-6Al-4V samples.

Table 3.1: Sintering Conditions

Composition (wt%)	Abbreviation	Temperature ($^{\circ}$C) and dwell time	Pressure (MPa)
WC-Cr_3C_2-10Co	10Co-S	1220^{o}C for 5 min	50
WC-Cr_3C_2-10Co	10Co-L	1430^{o}C for 75 min	4.4
WC-Cr_3C_2-Mo_2C-TiC-11Ni	11Ni-S	1320^{o}C for 5 min	70
WC-Cr_3C_2-Mo_2C-TiC-11Ni	11Ni-L	1430^{o}C for 75 min	4.4
WC-Cr_3C_2-Mo_2C-TiC-7Ni	7Ni-S	1380^{o}C for 5 min	70
WC-Cr_3C_2-Mo_2C-TiC-7Ni	7Ni-L	1430^{o}C for 75 min	4.4
NbC-12Co	N-12Co-S	1280^{o}C for 4 min	30
NbC-12Co	N-12Co-L	1430^{o}C for 75 min	4.4

*S = spark plasma sintered, L = liquid phase sintered

3.1.1 Procedure for liquid phase sintering (LPS) using a Sinter-Hip process

The powders of the starting compositions were thoroughly mixed and pressed into compacts before sintering with an ULTAR-TEMP Sinter-HIP furnace (Pilot Tools (Pty) Ltd.). The compacts were then placed in the furnace heating chamber and heated in vacuum (0.04MPa) at an initial heating rate of 2.4^{o}C/minute to 270^{o}C for 65 minutes. The vacuum pump was then turned off to allow the flow of hydrogen into the heating chamber for dewaxing. To ensure elimination of Polyethylene Glycol (PEG), four steps were used for dewaxing at varying heating rates and dwell times ranging from 270^{o}C to 450^{o}C (Figure 3.2). The furnace temperature was then held at 450^{o}C for an additional 20 minutes with the vacuum pump switched on so the hydrogen could be expelled from the heating chamber. To ensure replacement of carbon lost during dewaxing, a heating rate of 4.2^{o}C/minute was administered from 450°C to 1000°C, at which the temperature was held for 5 minutes, with the vacuum pump turned off to allow the flow of methane and hydrogen for carbon correction. Carbon control was then carried out for 90 minutes at a heating rate of .3°C/minute from 1000°C to 1200°C, after which the vacuum pump was switched on to remove the methane and hydrogen. Argon gas was added at a temperature of 1200°C, pressure of 0.37MPa, and a heating rate of 3.5°C/minute to 1430°C, while the temperature was then held for 75 minutes to ensure cobalt loss protection (CLP). Hot isostatic pressing (HIP) was carried out in the last 20 minutes at a pressure of 4.4 MPa, after which the furnace was with water at a rate of 3.5°C/minute to eliminate porosity.

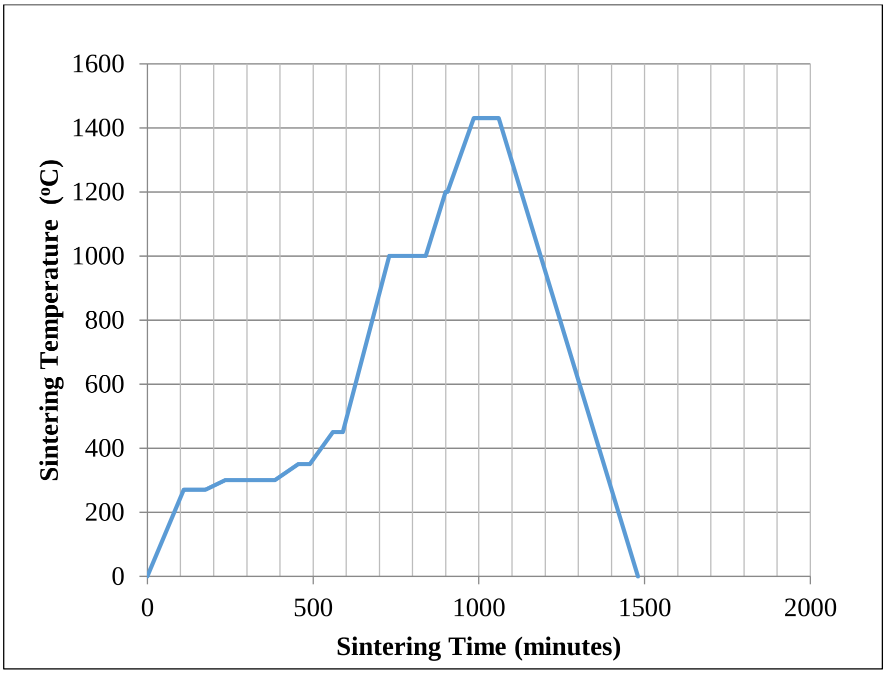

Figure 3.2: LPS temperature profile [total time 24 h and 42 minutes [2013Gen[b]]

3.1.2 Procedure for Spark Plasma Sintering (SPS)

The milled composite powders were consolidated using a HP D5 spark plasma sintering furnace (FCT Systeme GmbH), and afterwards poured into a cylindrical graphite die with inner diameter, outer diameter, and height of 20.9 mm, 40 mm and 48 mm respectively. The composite powder assemblies were heated in a vacuum in two steps (2 hPa). The powders were first heated to 1000°C at a rate of 200°C/min and later to 1220°C at a rate of 100°C/min, with the temperature held at 1220°C for 5 minutes during sintering. The samples were then cooled at a rate of 200 °C/min. Within 30mins of cooling the applied pressure adjusted from 16 MPa to 30 MPa at 1000°C, and from 30 MPa to 50 MPa at 1220°C through the rapid sintering cycle (Figure 3.3). Horizontal and vertical graphite papers were used to separate the powders from the die and punch setup. Boron nitride was placed on the graphite paper during the sintering process, so as to prevent the diffusion of carbon to the powder. In order to minimize heat loss from the surface of the graphite die, the die was wrapped in a carbon cloth. The temperature was monitored and controlled using an optical pyrometer which was focused on a central borehole on the upper punch located 1 mm above the top surface of the sample. The plunger position was also followed in order to monitor the consolidation of the composite powder assemblies in the axial direction. Depending on the compositions of the powder, different sintering profiles were achieved using good densification.

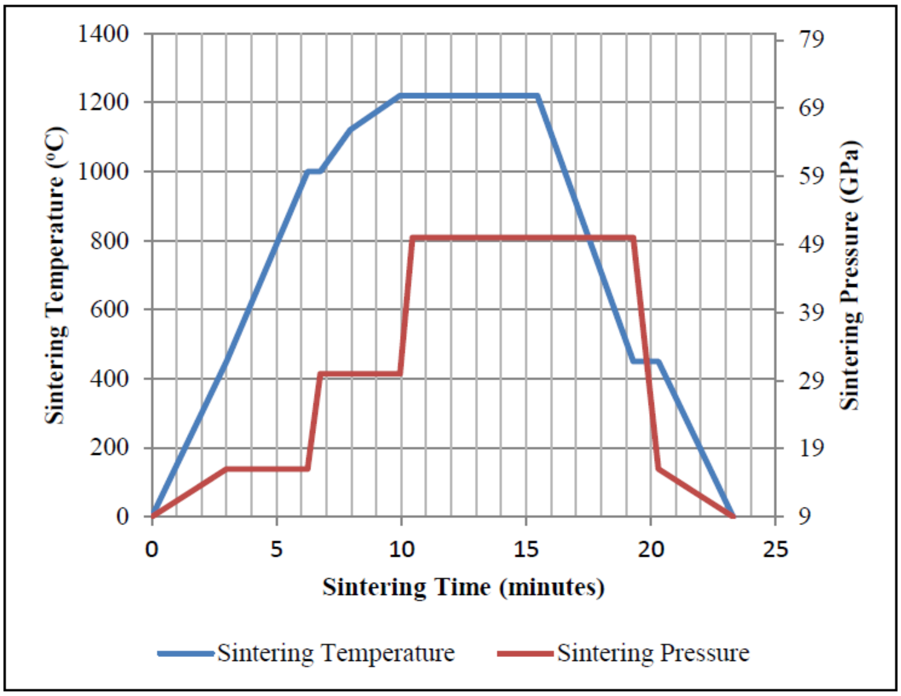

Figure 3.3: SPS temperature profile for production of WC-10Co (wt%), total times 23 minutes [2013Gen[b]]

3.2 Characterization of Sintered Samples

3.2.1 Density measurement

The Sartorius ED224S density measuring machine (Figure 3.4) was used to determine the density and open porosity of the samples. The Sartorius ED224S principle of operation is based on Archimedean principle, making it capable of determining the weight of a solid in air as well as in water. The specific gravity of a solid could also be determined using this machine, if the density of the liquid causing buoyancy is known.

Figure 3.4: Sartorius ED224S density measuring machine

3.2.1.1 Procedure

To accurately measure the density and open porosity of the samples, the surface of the samples were thoroughly cleaned to remove the hexagonal nitride and graphite paper used during the sintering process. To eliminate bubbles and fill surface pores, the samples were boiled in distilled water for 5 hours. The samples were then weighed in air to attain the wet mass (W2), and in distilled water to attain the suspended mass (W3). To attain the dry mass

(W1), a Labotec INC-O-MAT oven was used to dry the samples at 80^{o}C for 24 h, and afterwards the samples were weighed in air for the dry mass [1996Url]. To determine the true volume of sample, true density of sample, and the volume of open porosity of the samples, Equations 3.1 – 3.3 were used [1996Url].

True volume of sample = $\frac{W_1 - W_3}{W_1 \rho W}$ Equations 3.1

True density of sample = $\frac{W_1 \rho W}{W_1 - W_3}$ Equations 3.2

Volume of open porosity = $\frac{W_2 - W_1}{\rho W}$ Equations 3.3

Where ρW is the density of distilled water at room temperature.

3.2.1.2 Precautions

To avoid errors, the change in immersion level of the pan hanger assembly when the sample was immersed was taken into consideration. The air buoyancy during air weighing was also taken into consideration. Also, the temperature of the reference liquid was measured for subsequent correction of its density.

3.3 Mechanical Properties Characterization

3.3.1 Hardness Test

The hardness of the samples was determined using both the Vickers hardness and Rockwell hardness tests.

3.3.1.1 Vickers Hardness Test

The Vickers hardness test usually involves the indentation of samples using a pyramidal diamond indenter having a square base at an angle of 136 degrees (Figure 3.5). The Mitutoyo AVK-Co (Pilot Tools (Pty) Ltd.) was used in conducting the Vickers hardness test for the samples. A load of 1kgf to 100 kgf is then applied on the indentation for 10 to 15 seconds. After which a microscope is used to measure the indentation left on the surface of the material after removing the load. The resultant Vickers hardness is obtained by dividing the load (kgf) by the square area of indentation.

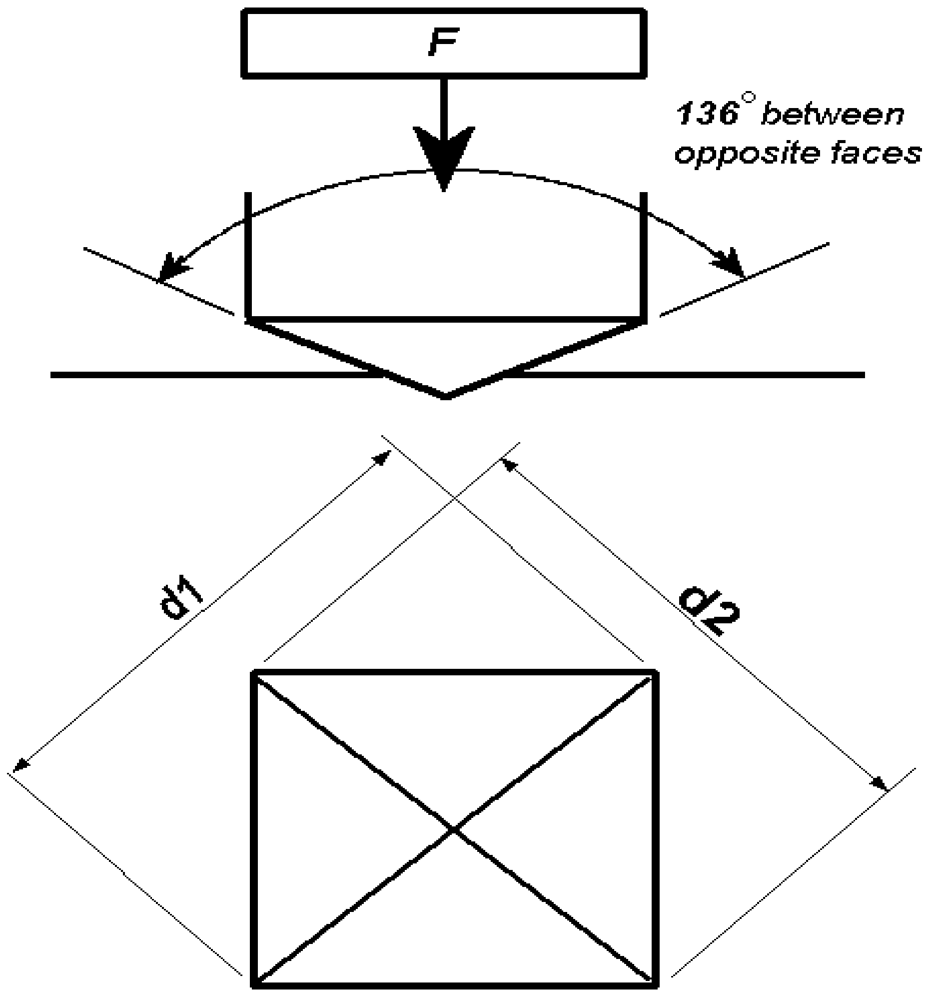

F = Load in kgf and d = Arithmetic mean of the two diagonals (d1 and d2) in mm.

Figure 3.5: Schematic diagram of diamond indenter used for Vickers hardness [1996Url]

3.3.1.1.1 Procedure:

Loads of 10Kg (HV10) and 30Kg (HV30 loads were applied on the diamond indenter for 10 seconds. Five indentations were carried out on different regions of each sample and the results were averaged. The corresponding Vickers hardness for the sample was calculated using Equation 3.4 – 3.5 [1996Url].

The force applied on the sample was calculated using Equation 3.4.

$F = m \times g$ (Equation 3.4)

Where F is Force applied, m is mass of load applied (kg), and g is gravitational acceleration ($9.82 m/s^2$).

While the Vickers hardness of the sample is given by Equation 3.5.

$HV = 1.854 \frac{F}{D^2}$ (Equation 3.5)

Where HV is the Vickers hardness of the sample, F is Force applied, and A is the area where the force is applied.

3.3.1.1.2 Precaution

Protective goggles were used to avoid the spark area. The surfaces of the samples were carefully prepared to ensure accurate measurements.

3.3.1.2 Rockwell Hardness Test

This test usually involves indenting the test material with either a diamond cone or hardened steel ball indenter having a minor and an additional major load serving as indentation forces. A general principle of the Rockwell hardness test can be seen in Figure 3.6. The Mitutoyo AKR-600 Rockwell-A tester (Pilot Tools (Pty) Ltd) was used for conducting the Rockwell hardness tests.

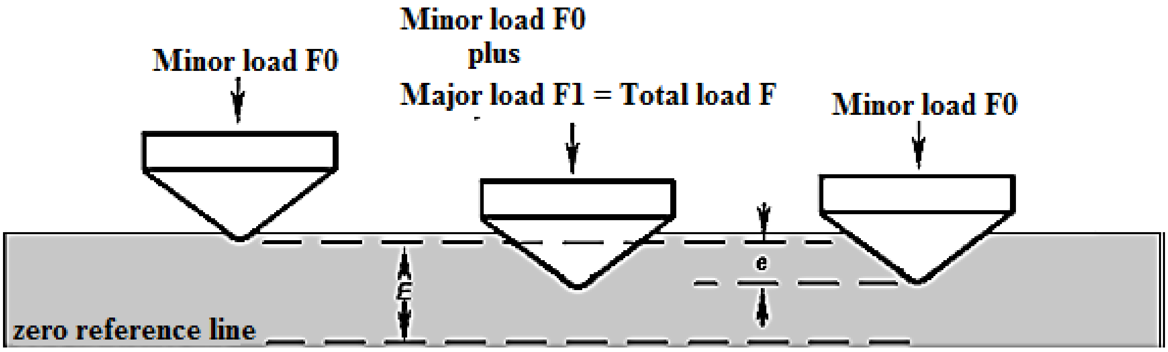

Figure 3.6: Rockwell Principle [1996Url]

3.3.1.2.1 Procedure

A minor load of 10kg (F1) was initially applied until equilibrium was reached. The indicator which follows the indenter movement, responded to the change in indenter penetration depth (e), and a reference position of zero was set. A major load of 60kg (F2) was then applied over the major load for 10 seconds and released to obtain a new penetration depth (E). The deference in penetration depth between the minor load position and the major load position was automatically measured and converted to obtain the Rockwell hardness number (HR) (Equation 3.6) [1996Url].

$$HR = E - e \qquad \text{(Equation 3.6)}$$

Where:

HR = Rockwell hardness number,

E = New penetration depth,

e = indenter penetration depth.

3.3.1.2.2 Precautions

In order to acclimatize the indenter, raising lowering screw, and specimen platform two preliminary tests were carried out. The specimen measurement location was spaced to at least

4d (where d = indentation diameter) from the centre of existing indentations. The surface and reverse face of the specimen was kept as horizontal as possible.

3.3.2 Fracture toughness

The fracture toughness of the sintered samples was measured using a Mitutoyo AVK-Co hardness indenter (Pilot Tools (Pty) Ltd) (Figure 3.7).

Figure 3.7: Mitutoyo AVK-Co hardness indenter

3.3.2.1 Procedure

The stress induced on the samples by the diamond indenter resulted in radial cracks at the edge of the indentations, Shetty equation (Equation 3.7 – 3.8) was used for accurate computation of fracture toughness in $MPa.m^{1/2}$ units [1985She]. For accurate computation of fracture toughness using Shetty equation, the following criteria were met: $1.25 \leq c/a \leq 2.25$ and $0.25 \leq I/a \leq 2.5$ [1985She].

Where:

c = crack length from the crack tip to centre of indentation.

a = half diagonal length of indentation, and

I = c-a

Shetty's equation is given in Equation 3.6 as follows:

$K_{IC} = 0.0889H^{0.5} \times (F/4I)^{0.5}$ Equations 3.7

Where:

H = hardness (GPa),

F = applied force (Newton), and

I = is average crack length (mm) given by Equation 3.8.

$I = (2c-2a)/2$ Equations 3.8

3.3.2.2 Precautions

Protective goggles were used to avoid the spark area.

3.4 Ti-6Al-4V Machining Trials

The Bridgeport GX1000 CNC milling machine (School of Mechanical, Industrial and Aeronautical Engineering, Wits University) (Figure 3.8) was used for conducting all the machine trials. A vice was bolted to the CNC machine table to clamp the work-piece in place.

3.4.1 Procedure

Face milling was carried out on the 105mm x 105mm x 5mm Ti-6Al-4V samples (Figure 3.9) (Twenty workpieces were used) using the innovative cemented carbide cutting tools produced by Liquid Phase Sintering (LPS) and Spark Plasma Sintering (SPS). The geometry of the cutting tool inserts can be seen in Figure 3.10. One effective insert was used per milling test. For each test, the respective cutting tool insert was inserted into the BT40-22-45V cutting tool holder which had an 80mm radial depth of cut (Figure 3.11). The tool was fastened onto the tool holder with the desired cutting edge facing outwards. The tool holder was then locked onto the spindle of the CNC machine. The Depth of cut (a_p), cutting speed (v_c) and other machining parameters were sequentially programmed into the CNC machine in accordance with the machining parameters shown in Table 3.2 and Table 3.3. On completion of each machine trial, the workpiece and the cutting tool edge were labeled accordingly for identification and further analysis. Chips were also collected from each machining trial for future investigation.

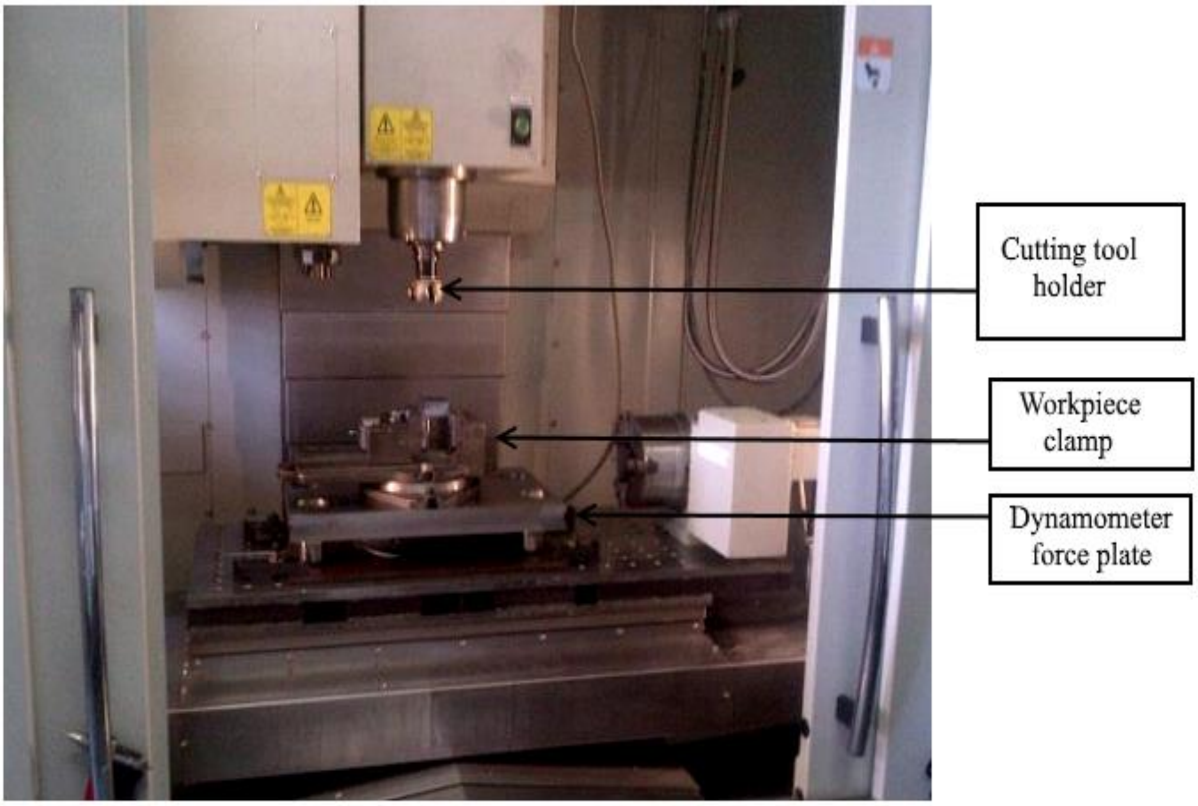

Figure 3.8: Overview of Bridgeport GX1000 CNC Machine with attached cutting tool holder, workpiece clamp, and dynamometer force plate

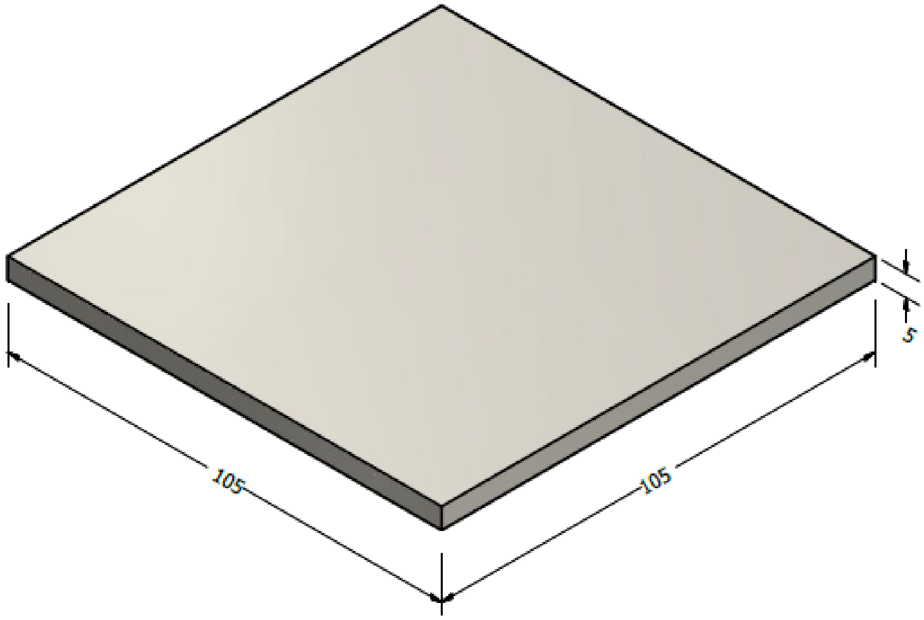

Figure 3.9: Dimension of the Ti-6Al-4V workpiece in millimeters

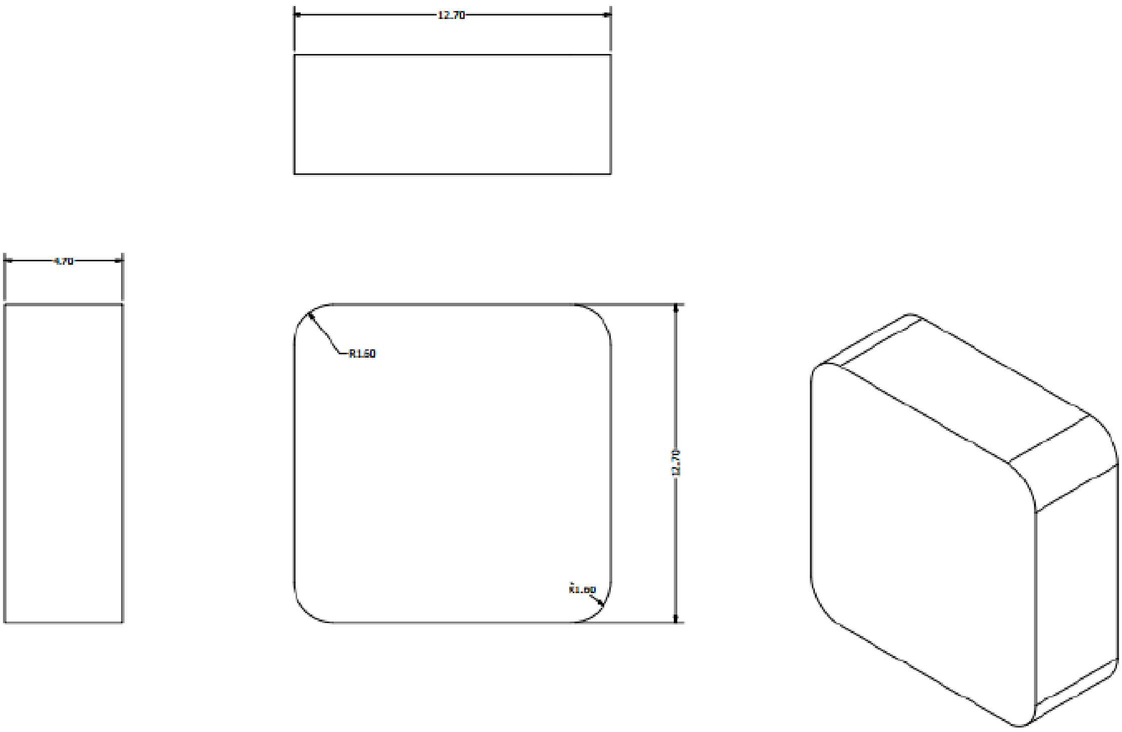

Figure 3.10: Cutting tool geometry

F75 SN

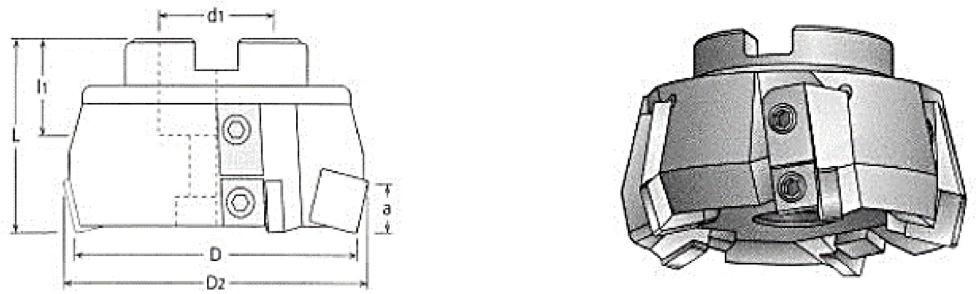

DESCRIPTION	ITEM NUMBER		DIMENSIONS (mm)						INSERT	INS. SCREW	INS. WEDGE	CART. WEDGE	CARTRIDGE	TORX KEY
			D	D2	L	d1	l1	a						
F75SN12080	1133204	5	80	86	50	27	22	9						

Figure 3.11: Tool holder geometry and specifications

Table 3.2: Dry milling parameters for Ti6Al-4V

Test No:	Insert	Cutting speed, v_c [m/minute]	Depth of cut, a_p [mm]	Spindle speed, N [rpm]	Feed rate, v_f [mm/minute]
1	10Co-L	40	1	160	16
2	10Co-S	40	1	160	16
3	11Ni-L	40	1	160	16
4	11Ni-S	40	1	160	16
5	7Ni-L	40	1	160	16
6	7Ni-S	40	1	160	16
7	N-12Co-L	40	1	160	16
8	N-12Co-S	40	1	160	16
9	10Co-L	60	1	240	24
10	10Co-S	60	1	240	24
11	11Ni-L	60	1	240	24

12	11Ni-S	60	1	240	24
13	7Ni-L	60	1	240	24
14	7Ni-S	60	1	240	24
15	10Co-L	75	0.5	300	30
16	10Co-S	75	0.5	300	30
17	7Ni-L	75	0.5	300	30
18	7Ni-S	75	0.5	300	30
19	10Co-L	100	0.5	400	40
20	10Co-S	100	0.5	400	40
21	7Ni-L	100	0.5	400	40
22	7Ni-S	100	0.5	400	40

Table 3.3: MQL milling parameters for Ti6Al-4V

Test No:	Insert	Cutting speed, v_c [m/minute]	Depth of cut, a_p [mm]	Spindle speed, N [rpm]	Feed rate, v_f [mm/minute]	MQL Flow rate [pulse/sec]
23	10Co-L	75	0.5	300	30	0.4
24	10Co-S	75	0.5	300	30	0.4
25	7Ni-L	75	0.5	300	30	0.4
26	7Ni-S	75	0.5	300	30	0.4
27	10Co-L	100	0.5	400	40	0.4
28	10Co-S	100	0.5	400	40	0.4
29	7Ni-L	100	0.5	400	40	0.4
30	7Ni-S	100	0.5	400	40	0.4

*S = spark plasma sintered, L = liquid phase sintered

3.4.2 Precautions

To ensure the DOC was always accurate, the CNC machine was always calibrated toward the datum of the top surface of the workpiece placed in the holding clamp. This was done before milling commenced on every Ti-6Al-4V workpiece used. Furthermore, all foreign objects within the CNC machine machining chamber were removed to avoid obstruction.

3.5 Force Measurement

The Kistler 9255C dynamometer system (Figure 3.12) which comprised of a force plates, an amplifier, and a data acquisition system was used in measuring the cutting forces during the milling trials. The Kistler force plate was mounted underneath the workpiece clamp of the milling machine, while the data acquisition system was connected to a computer which had a DynoWare software installed for data acquisition and analyses (Figure 3.12). The dynamometer principle of operation is based on the unidirectional piezoelectric crystals in the force plate generating an electrical potential difference when a force is exerted. The force plate measures the force in three orthogonal directions (Fx, Fy, and Fz), while the summing box computes the net effect of the force and the moment in the three orthogonal direction (Mx, My, Mz).

Figure 3.12: Kistler 5697A DAQ System and Charge Amplifier

3.5.1 Procedure

The Kistler 9255C dynamometer force plate was bolted in-between the vice and the CNC machine. The cutting force per milling run the resultant forces obtained for every one tenth of a second ($^{1}/_{10}$sec) and resolved in the *x*, *y*, and *z* direction, where x is the direction correlating to the feed direction, y in the direction of the perpendicular to the feed and parallel to the workpiece top surface, and z the direction parallel to the spindle. The resultant force for every one tenth of a second ($^{1}/_{10}$sec) was then calculated using Equation 3.9. The average resultant force per milling run was afterwards calculated using Equation 3.10.

Resultant force (F_R) = $\sqrt{{F_X}^2 + {F_Y}^2 + {F_Z}^2}$ Equation 3.9

Average resultant force (Av.F_R) $\frac{F_{R1} + F_{R2} +,+ \ldots + F_{Rn}}{\text{number of } F_R \text{ readings in experiment}}$ Equation 3.10

Where: $F_{R1}, F_{R2}, + \ldots + F_{Rn}$ are respective resultant forces for every one tenth of a second ($^{1}/_{10}$sec).

3.6 Emissivity Measurement

For accuracy in thermal readings, the K-type thermocouple was used in calibrating the emissivity of the workpiece material. The K-type thermocouple had a sensitivity of 1 µV/°C, with a thermal measuring capacity ranging from −200°C to 1,260°C. It was basically made up of two thermo-elements; Chromel (90% Nickel, 10% Chromium) and Almelo (95% Nickel, 2% Manganese, 2% Aluminium and 1% Silicon).

Figure 3.13: K – Type Thermocouple

3.6.1 Procedure

One Ti-6Al-4V block was heated in a 2400W LABOTEC oven (School of Chemical and Metallurgical Engineering, Wits University) for six hours, at a controlled temperature of 60^{o}C. Immediately the block was removed from the oven, one end of the thermocouple wires was fastened to the workpiece using an adhesive, while the other end was connected to the digital multimeter using a plug. The resulting temperature of the workpiece was displayed on the LCD of the multimeter. Simultaneously, the Flir T640 thermal imaging camera (Figure 3.13) which was mounted on a tripod stand 1m away from the work-piece material was also focused on the work-piece. The resulting temperature and emissivity value displayed on the thermal camera's LCD was recorded. The true emissivity of the Ti-6Al-4V block was finally obtained when the temperature reading on the Flir thermal camera corresponded with the temperature reading on the K-type thermocouple. The emissivity of the Ti-6Al-4V sample was 0.23.

3.6.2 Precautions

To ensure accuracy in thermal readings, the flir thermal camera was mounted 1m away from the workpiece.

3.7 Temperature Measurement

The Flir T640 Thermal imaging Camera (School of Mechanical, Industrial and Aeronautical Engineering, Wits University) (Figure 3.14) was used in measuring the cutting zone temperature for each milling trial.

Figure 3.14: Flir T640 thermal imaging camera connected to a laptop computer

The temperature range of the camera was between -40 to 2000°C, while the thermal sensitivity of the camera was 0.035°C [2014Fli]. The operating principle of the thermal imaging camera is based on detecting the amount of infrared an object emits due to temperature.

3.7.1 Procedure

The Flir camera was mounted onto a tripod stand which was positioned 1m away from the milling machine to ensure accurate thermal readings. The camera was then connected to a computer which had a Flir Tools software installed and running. The work-piece emissivity, reflective temperature, atmospheric temperature and other operating parameters for the camera was configured on the camera setup menu. The camera was then focused on the cutting zone (the combination of the cutting insert and the workpiece). The Flir tools software was used to create a video file for each machine trial. These video files were subsequently analyzed to obtain the thermal readings for each machine trial.

3.7.2 Precaution

The thermal range on the Flir PC suite was switched to a higher thermal regime immediately the temperature exceeded 1000^{o}C.

3.8 Minimum Quantity Lubrication

The Producut MQL system was used for controlled application of working fluid during MQL machining trials. The MQL system was attached to the Bridgeport GX1000 CNC milling machine (Figure 3.15). A biodegradable plant oil with a high flash point was used for the working fluid.

3.8.1 Procedure

The hose of the MQL system was fastened 50cm away from the clamped workpiece, with the cutting zone in focus. The MQL dial was then set to the 0.6 seconds/pulse. The system was then turned on immediately the cutter was about to engaged the workpiece.

3.8.2 Precautions

To avoid excessive lubrication the MQL system was turned on immediately when the cutter was about to engage with the workpiece and turned off immediately the cutter exited the workpiece.

Figure 3.15: Producut MQL system mounted onto the Bridgeport GX100 CNC milling machine

3.9 Flank Wear Measurement

The Leica DM600 metallurgical microscope (Figure 3.16) was used to capture micrographs of the cutting tool edges after the milling trials. The micrographs were then analyzed to determine the resultant crater wear and flank wear on the cutting tool edges.

Figure 3.16: Leica DM600 Metallurgical Microscope

3.9.1 Procedure

The Leica DM600 metallurgical microscope was connected to a computer which had the Leica DM600 software installed. The software was launched, and the "Live feed" mode was enabled. The microscope was then set to 5x magnification, and each cutting insert was placed on the microscope stage with the cutting edge in focus. The knob and dials of the microscope were used to adjust the view of the sample until the sight of the flank was clear. The DM600 was then used to acquire and measure the longest vertical length of the flank wear. The measured length and scale bar for each flank wear image was onto the image and saved accordingly.

3.9.2 Precautions

To avoid taking skew measurements, the distance measured was always vertical. It was ensured that the cutting tool insert was at the center of the monitor before each micrographs was acquired.

3.10 Roughness Measurement

The roughness of the machined Ti-6Al-4V surfaces was measured using the profilometry and laser confocal techniques.

3.10.1 Profilometry

The TR220 profilometer (School of Chemical and Metallurgical Engineering, Wits University) (Figure 3.17) was used to measure the surface roughness of the work-pieces after the machine trials. The profilometer basically consist of a detector and a sample stage. The detector was made up of a diamond stylus which was used to determine the points on the sample surface, while the sample stage was used to measure the surface roughness of the sample. The sample stage performs lateral movements which results in the stylus scratching over the point of interest, hence determining the surface roughness at that point.

3.10.1.1 Procedure

To determine the roughness value of the machined Ti-6Al-4V samples, roughness measurements were carried out on six different points per sample surface as shown in Figure 3.18a and 3.18b. Each sample was placed on the TR220 profilometer stage, with the detector 20mm away from the machined clearance of the workpiece. The “pick up” icon on the TR220 PC suite was then clicked to display the scale and contact of the stylus. After which the lever of the profilometer was adjusted until the stylus came in contact with the work-piece and a value of zero was displayed on the scale. The zero value indicated that the sensor is completely horizontal.

Figure 3.17: TR220 Profilometer

The “measurement” icon was clicked for the roughness measurement, and the result obtained was recorded. The above procedure was repeated for all the Ti-6Al-4V samples and the obtained roughness values were recorded. The surface roughness values results obtained from the six points measured per workpiece was averaged using Equation 3.11, while the roughness error for each surface was determined by standard deviation (Equation 3.12).

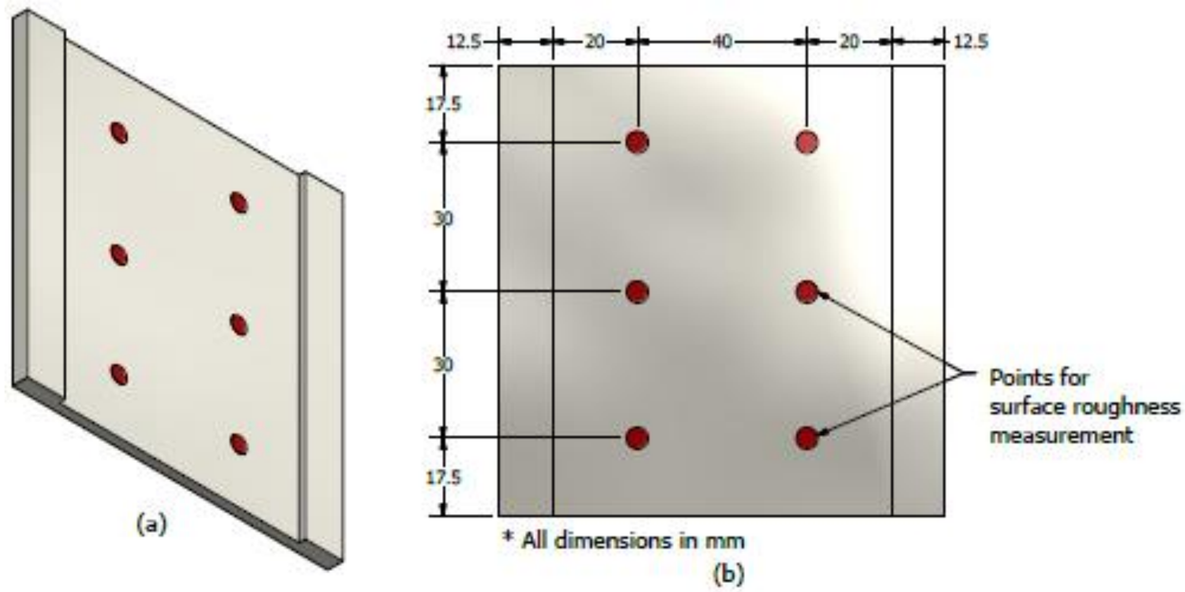

Figure 3.18: (a) 3D and (b) 2D representation of workpiece showing locations where surface roughness measurements were taken

$$R_{a_{(average)}} = \frac{R_{a1}+R_{a2}+R_{a3}+R_{a4}++R_{a5}+R_{a6}}{6} \qquad \text{Equation 3.11}$$

$$\sigma R_a = \sqrt{\frac{\sum(x-\bar{x})}{N}} \qquad \text{Equation 3.12}$$

Where σR_a = standard deviation for the roughness,

x = each value in the measurement,

$\bar{x}$ = mean of the values, and

N = number of values obtained per surface.

3.10.1.2 Precautions

The surface of the samples were cleaned with ethanol to ensure they were free from foreign bodies. The lever of the profilometer was adjusted with absolute care as any impact on the sensor might damage or distort the functionality of the sensor. Roughness measurements were only carried out when a value of zero was obtained on the scale.

3.10.2 Leica Confocal

The Leica LCSM TCP SP2 SE Microscope (Figure 3.18) was also used to measure the surface roughness of the workpieces. The SP2 microscope uses a laser beam to obtain high resolution optical images with depth selectivity and then reconstructs them into two dimensional or three dimensional topographical images.

Figure 3.19: Leica LCSM TCP SP2 SE Microscope

3.10.2.1 Procedure

To measure the roughness of each Ti-6Al-4V surface three points were selected on the surface of each work-piece as shown in Figure 3.20a and 3.20b. The Hg arc power supply of the microscope was turned on, followed by the microscope controller power, the PC Stand Power, the CPU, and the Scanner Power. The Ar laser blower and lasers were then started with the Ar laser tuned to 9:00. The adjustment knob on the microscope scan head was set to visual mode. The Leica application was then used to set the microscope objective, beam type and other parameters. The objective used was 40x, while the beam type was reflected and the MicCtrl” tab set to visual. The Ti-6Al-4V workpiece was placed under microscope scan head (stage) with the area of focus facing downward. The knobs and dials of the microscope were used to adjust the view of the sample until the brightest spot of the sample became visible and clear. The adjustment knob on the microscope scan head was then set to scan. On the Leica software the continuous mode was enabled and the Z scan was set to wide. Before initializing the Z scan, the series tab was used to configure the Z scan range and gain. After scanning was complete, the 2D images were averaged and analyzed in both 2D and 3D topographical layers. The roughness of the sample at that point was determined by the standard deviation value.

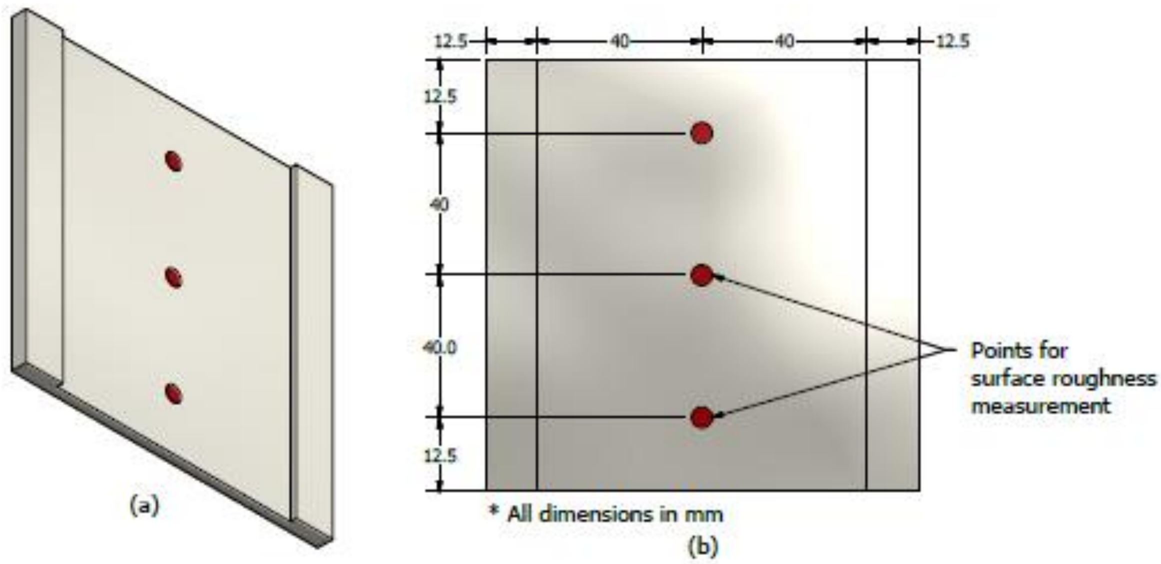

Figure 3.20: (a) 3D and (b) 2D representation of workpiece showing locations where surface roughness measurements were taken

The surface roughness values obtained from the three measured points on each sample were averaged using Equation 3.13, while the roughness error for each surface was determined by standard deviation (Equation 3.12)

$$R_{a(average)} = \frac{R_{a1} + R_{a2} + R_{a3}}{3} \qquad \text{Equation 3.13}$$

3.10.2.2 Precautions

For accuracy in roughness readings, the Z scan was always set to the maximum limits (where the image was almost out of focus) with the gain of the brightest area in the Z-scan range reduced. All the Z scan images were averaged for results.

3.11 Residual Stress Measurement

The residual stress in each sample was measured using the X-ray Diffraction Technique (XRD). The XRD is a non-destructive experimental technique which entails measuring the strain in the crystal lattice and calculating the residual stress producing the strain. An intrinsic property, such as strain or force and area is measured and calculated for the associated stress. To determine the stress, the strain in the crystal lattice will be precisely measured for at least two known orientation relative to the sample surface. The Xstress 3000 G3 X-ray stress analyser (X-ray diffractometer) was used for measuring the residual stresses in the Ti-6Al-4V samples (Figure 3.21).

Figure 3.21: G3 X-ray stress analyser

3.11.1 Procedure

To measure the residual stress in each workpiece, three points were selected on the surface of each work-piece as shown in Figure 3.22a and 3.22b (the cutter entry and exit point on the workpiece as well as the mid-point of the workpiece).

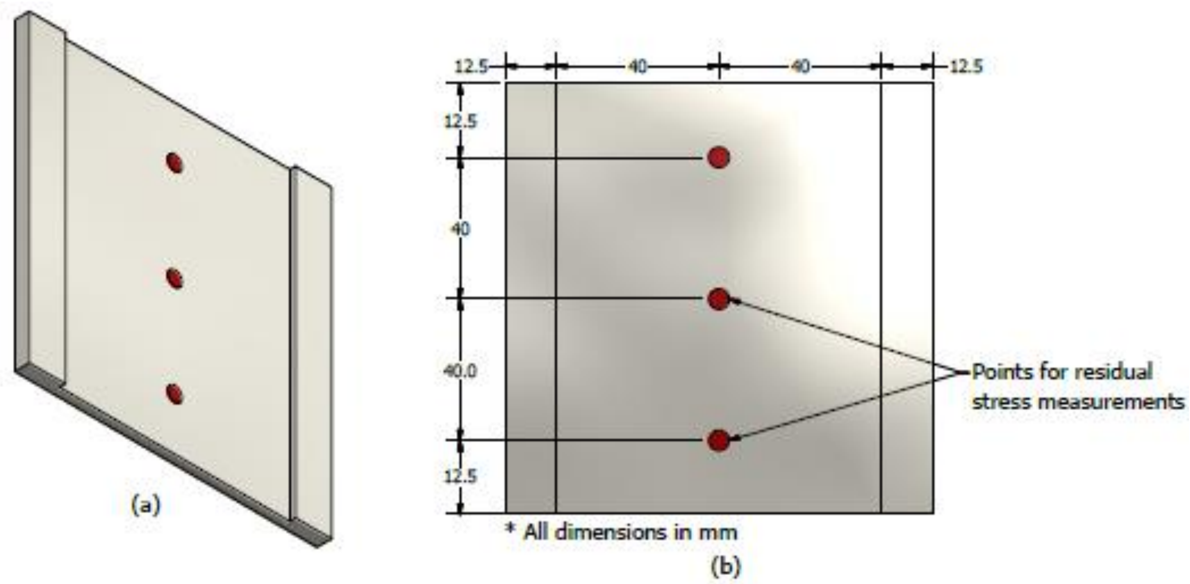

Figure 3.22: (a) 3D and (b) 2D representation of workpiece showing locations where XRD measurements were taken

The $\sin^2\Psi$ method was used to determine residual stresses in the Ti-6Al-4V samples after machining. The residual stress was defined by Equation 3.14 below [2005Fit[b]]. A linear relationship between the inter-planar spacing at the measured Ψ value and $\sin^2\Psi$.

$$\sigma = m\left(\frac{E}{1+v}\right) \quad \text{Equation 3.14}$$

Where σ is residual stress, m is the slope of the regressed straight line, E is the elastic modulus and, v = Poisson ratio.

Bragg's Law (Equation 3.15) was used to create the straight line shown in Figure 3.23.

$$d_\Psi = m\left(\frac{n\lambda}{2sin\theta}\right) \quad \text{Equation 3.15}$$

Where d_Ψ is the inter-planar spacing at a chosen Ψ-value.

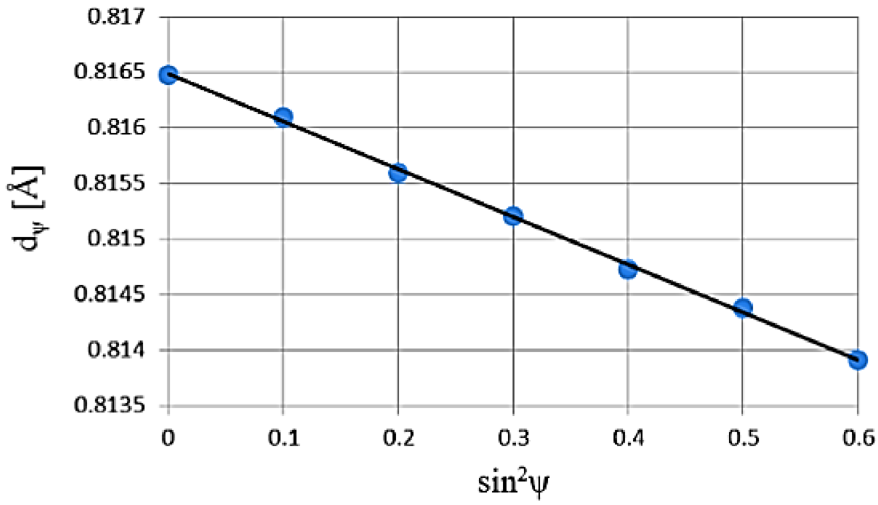

Figure 3.23: linear curve created by sin2Ψ method

The value of Ψ is usually chosen logically, so for each residual stress measurement in these experiments, so seven different values of Ψ were used. In order to determine the value for θ, the X-ray intensity over a range of θ values were measured until the peak intensity was found. The Gaussian amplitude peak function, Lorentzian Peak function, Pearson VII peak function, Voigt Peak function, Pseudo Voigt type I peak function, and the Pseudo Voigt type II peak function were used to find the peak intensity [2005Fit[b]].

3.11.2 Precautions

The sample surface was carefully protected from secondary abrasion, corrosion, or etching so as to avoid alterations of in the residual stress.

Chapter 4 : Data Analysis and Results

This chapter analyses obtained data as well as results for both milling parameters and performance characteristics.

4.1 Physical and Mechanical Properties of Inserts

It is suspected that altering the binder matrixes of cemented carbide tools as well as varying the sintering techniques used for their production could improve upon their mechanical matrixes. The mechanical properties of the cemented carbide inserts after altering their binder matrixes and sintering condition are analysed in this section, in an attempt to find enhanced properties.

4.1.1 Densification

The obtained densification and volume of open porosity for the cutting tool samples are shown in Table 4.1.

Table 4.1: Density and Open Porosity of Sintered Samples

Abbreviation	Densification [%]	Open porosity volume [%]
10Co-L	99.85 ± 0.14	0.07 ± 0.01
10Co-S	99.75 ± 0.09	0.01 ± 0.00
7Ni-L	99.76 ± 0.12	0.00 ± 0.00
7Ni-S	99.02 ± 0.20	0.04 ± 0.01
11Ni-L	99.75 ± 0.16	0.03 ± 0.02
11Ni-S	99.61 ± 0.24	0.02 ± 0.01
N-12Co-L	98.92 ± 0.29	0.03 ± 0.01
N-12Co-S	99.20 ± 0.12	0.02 ± 0.01

The densification of the LPS samples was higher than that of the SPS samples, except for the N-12Co-S sample which had a densification than the N-12Co-L sample (Figure 4.1). The higher densification of the LPS samples was due to the longer sintering dwell time, pressure and temperature [2015Gen].

The 10Co-L sample had the highest densification with a low amount of open porosity volume, while the 11Ni-L and 7Ni-L samples had fairly similar densification despite the differences in their open porosity volume of the 7Ni-L insert (Figure 4.1).

4.1.2 Hardness

Results from the Vickers and Rockwell hardness test of the samples shows that the hardness for the SPS samples was higher than the LPS samples, with the 7Ni-S and N-12Co-L samples having the highest and lowest hardness respectively (Table 4.2 and Figure 4.2).

Table 4.2: Vickers hardness and Rockwell hardness of Samples

Abbreviation	Vickers hardness, HV_{30} [GPa]	Rockwell-A hardness, HRA [60Kgf]
10Co-L	15.03 ± 0.13	90.20 ± 0.18
10Co-S	17.34 ± 0.10	93.02 ± 0.13
7Ni-L	18.00 ± 0.27	93.48 ± 0.12
7Ni-S	20.36 ± 0.11	94.60 ± 0.35
11Ni-L	15.96 ± 0.15	92.02 ± 0.27
11Ni-S	18.85 ± 0.19	93.58 ± 0.24
N-12Co-L	10.46 ± 0.11	87.6 2± 0.17
N-12Co-S	13.21 ± 0.11	89.86 ± 0.11

*S = spark plasma sintered, L = liquid phase sintered

The 11Ni-L sample also had higher hardness than the 10Co-L samples (Figure 4.2). Similar in hardness trend was also observed for the SPS samples, with the 7Ni-S and N-12Co-S samples having the highest and lowest hardness respectively (Figure 4.2).

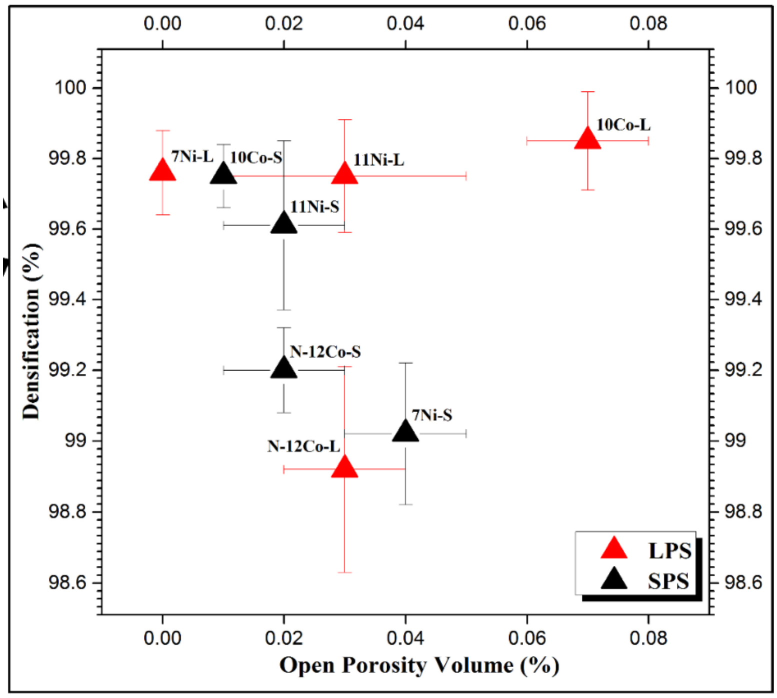

Figure 4.1: Variation in densification and open porosity for cutting tool samples

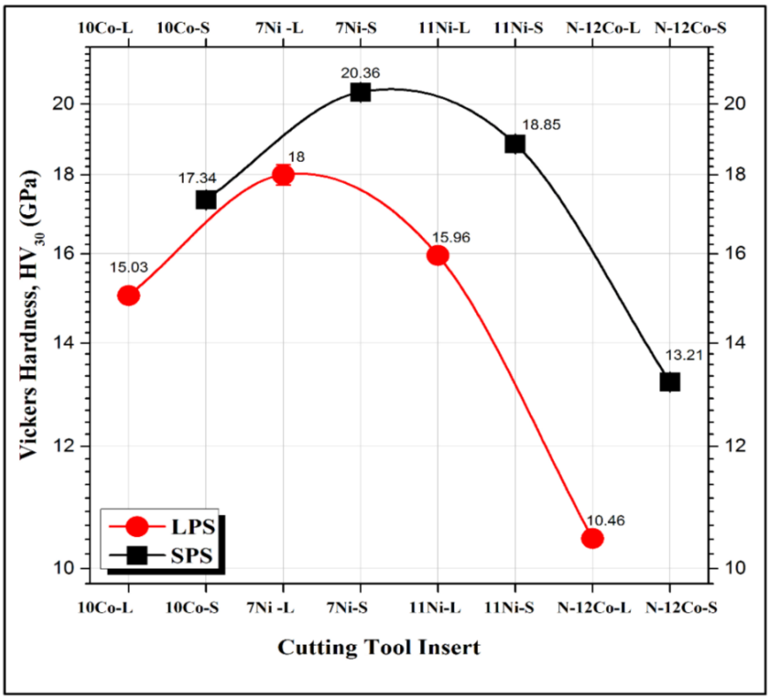

Figure 4.2: Variation in Vickers hardness (HV30) for LPS and SPS samples

4.1.3 Fracture Toughness (K_{IC})

The results obtained for the fracture toughness (K_{IC}) of the sintered samples shows that the LPS samples had higher K_{IC} than the SPS samples, except for the N12Co-L insert which had a lower K_{IC} compared to the N-12Co-S insert (Table 4.3 and Figure 4.3).

Table 4.3: Fracture toughness of Samples

Abbreviation	Fracture toughness, KIc [MPa.m1/2]
10Co-L	12.71 ± 0.23
10Co-S	11.84 ± 0.16
7Ni-L	10.69 ± 0.23
7Ni-S	10.18 ± 0.15
11Ni-L	11.22 ± 0.16
11Ni-S	10.38 ± 0.43
N-12Co-L	7.30 ± 0.15
N-12Co-S	7.87 ± 0.18

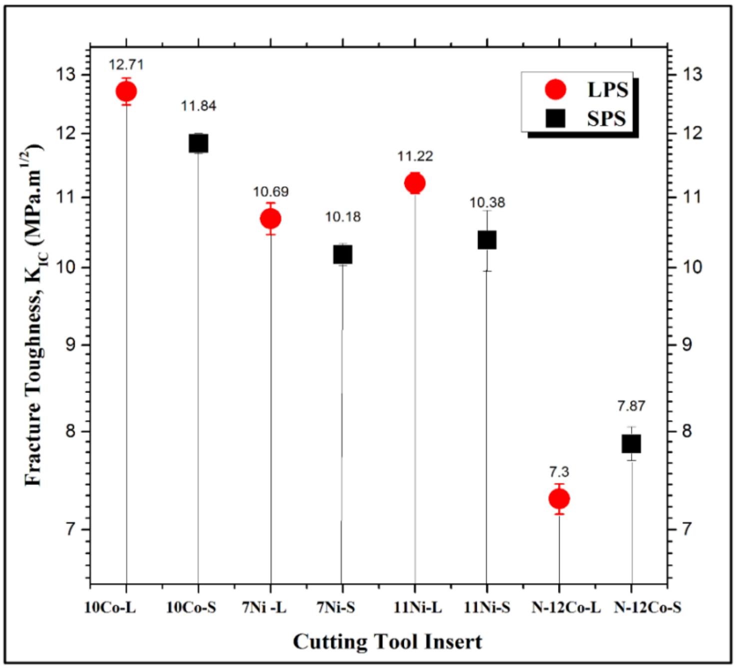

Figure 4.3: Variation in Fracture toughness (K_{IC}) for LPS and SPS samples

4.1.4 Overall Trends

It was observed that samples with higher Vickers hardness had lower fracture toughness, while those with higher fracture toughness had lower Vickers hardness (Figure 4.4). This trend was consistent for all the samples except for the N-12Co-L and N-12Co-S samples which had relatively lower Vickers hardness and Fracture toughness (Figure 4.4). The LPS samples generally had a higher K_{IC} than the SPS samples, while the SPS samples had a higher HV_{30} than the SPS inserts (Figure 4.4).

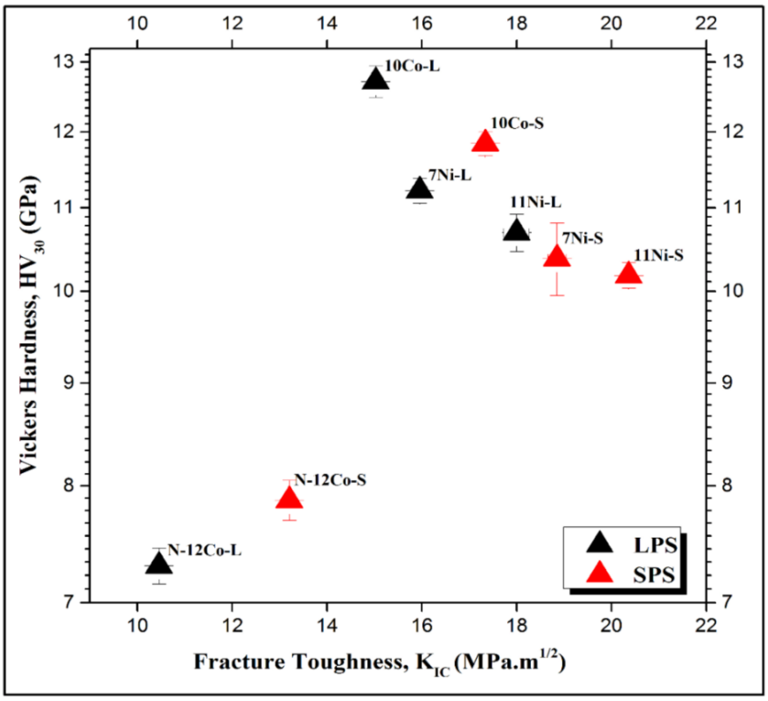

Figure 4.4: Comparison of Fracture toughness (K_{IC}) and Vickers hardness (HV30) for cutting tool inserts

4.2 Temperature

It is suspected that the temperatures generated at the tool-workpiece interface during milling are influenced by milling parameters. Therefore, the temperature data obtained from each milling run are analyzed in this chapter, in order to compare, as well as attempt to find correlations between the milling parameters and temperature.

4.2.1 Analyses of milling temperature at a $\boldsymbol{v_c}$ of 40m/minute and $\boldsymbol{a_p}$ of 1mm

At a v_c of 40m/minute and an a_p of 1mm, the temperatures experienced by the LPS inserts were lower than that of the SPS inserts (Table 4.4 and Figure 4.5).

Table 4.4: Average cutting temperature during MQL milling at a v_c of 40m/minute and an a_p of 1mm

Sample abbreviation	Milling Conditions		Average Temperature [^{o}C]
	v_c [m/minute]	a_p [mm]	
10Co-L	40	1	632.5 ± 17.9
10Co-S	40	1	724.4 ± 21.5
11Ni-L	40	1	786.9 ± 23.6
11Ni-S	40	1	804.4 ± 24.2
7Ni-L	40	1	636.6 ± 18.4
7Ni-S	40	1	714.7 ± 20.1
N-12Co-L	40	1	486.6 ± 11.8
N-12Co-S	40	1	610.7 ± 17.4

The N-12Co-L insert experienced the lowest temperature of 486.6 ± 11.8 ^{o}C, followed by the 10Co-L and 7Ni-L inserts with similar temperatures of 632.5 ± 17.9 ^{o}C and 636.6 ± 18.4 ^{o}C respectively (Figure 4.5). The 7Ni-L insert experienced the highest temperature for the LPS inserts, while the 11Ni-S insert experienced the highest temperature for the SPS inserts (Figure 4.5).

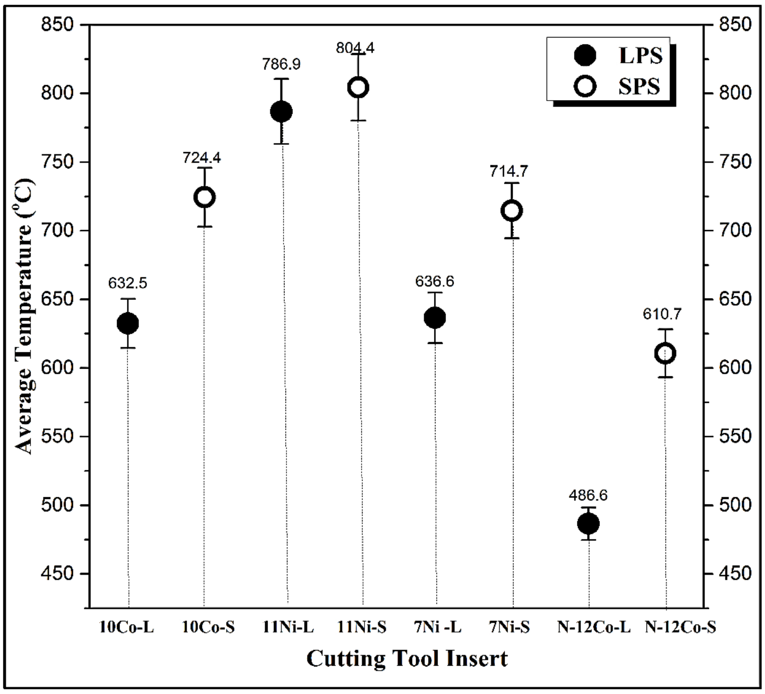

Figure 4.5: Variation in milling temperatures during dry milling at a v_c of 40m/minute and an a_p of 1mm

4.2.2 Analyses of milling temperature at a $\boldsymbol{v_c}$ 60m/minute and $\boldsymbol{a_p}$ of 1mm

At a v_c of 60m/minute and an a_p of 1m, the temperature experienced by the LPS inserts was also lower than that of the SPS inserts (Table 4.5).

Table 4.5: Average cutting temperature during MQL milling at a v_c of 60m/minute and an a_p of 1mm

Sample abbreviation	Milling Conditions		Average Temperature [°C]
	v_c [m/minute]	a_p [mm]	
10Co-L	60	1	427.3 ± 10.6
10C0-S	60	1	676.4 ± 17.9
11Ni-L	60	1	748.5 ± 21.6
11Ni-S	60	1	864.7 ± 26.1
7Ni-L	60	1	703.4 ± 19.1
7Ni-S	60	1	760.4 ± 22.7

The 10Co-L insert experienced the lowest temperature of 427.3 ± 10.6°C, followed by the 7Ni-L insert (Figure 4.6). The 11Ni-L and 11Ni-S inserts experienced the highest temperature for LPS and SPS inserts respectively (Figure 4.6).

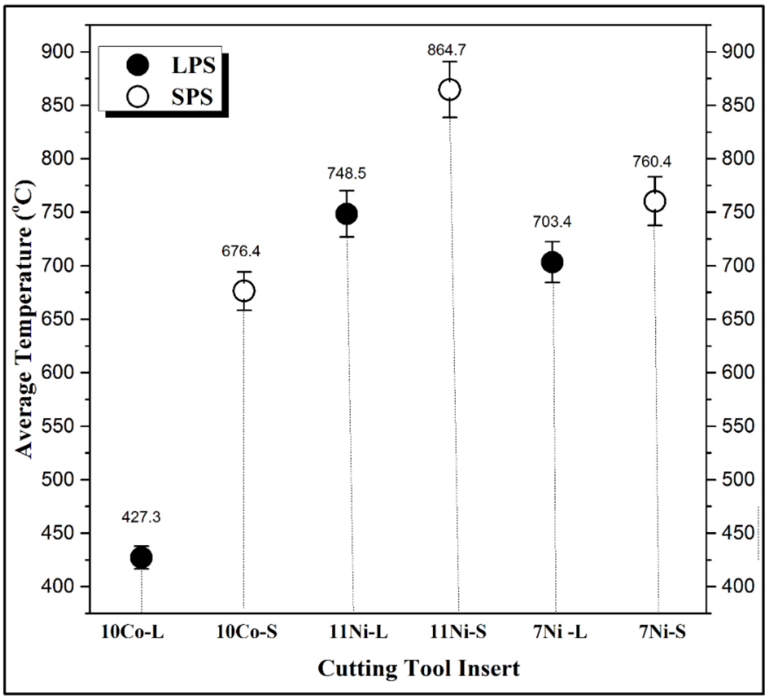

Figure 4.6: Variation in milling temperatures during dry milling at a v_c of 60m/minute and an a_p of 1mm

4.2.3 Analyses of temperature at a $\boldsymbol{v_c}$ of 75m/minute and $\boldsymbol{a_p}$ of 0.5mm

The results for milling runs at a v_c of 75m/minute and an a_p of 0.5mm, shows that the temperatures experienced by the LPS inserts were lower than that of the SPS inserts (Table 4.6 and Figure 4.7). The temperature experienced by the 10Co-L insert was lower than that of the 7Ni-L insert (Figure 4.7). Similarly, the temperature experienced by the 10Co-S insert was lower than that of the 7Ni-S insert (Figure 4.7). An analysis of the cutting temperature with respect to insert composition reveals that the temperatures experienced by the 10Co-L and 10Co-S inserts were lower than that of the 7Ni-L and 7Ni-S insert (Figure 4.7).

Table 4.6: Average cutting temperature during dry milling at a v_c of 75m/minute and an a_p of 0.5mm

Sample abbreviation	Milling Conditions		Average Temperature [ºC]
	v_c [m/minute]	a_p [mm]	
10Co-L	75	0.5	237.8 ± 6.5
10C0-S	75	0.5	251.3 ± 6.3
7Ni-L	75	0.5	638.7 ± 18.1
7Ni-S	75	0.5	649.1 ± 17.6

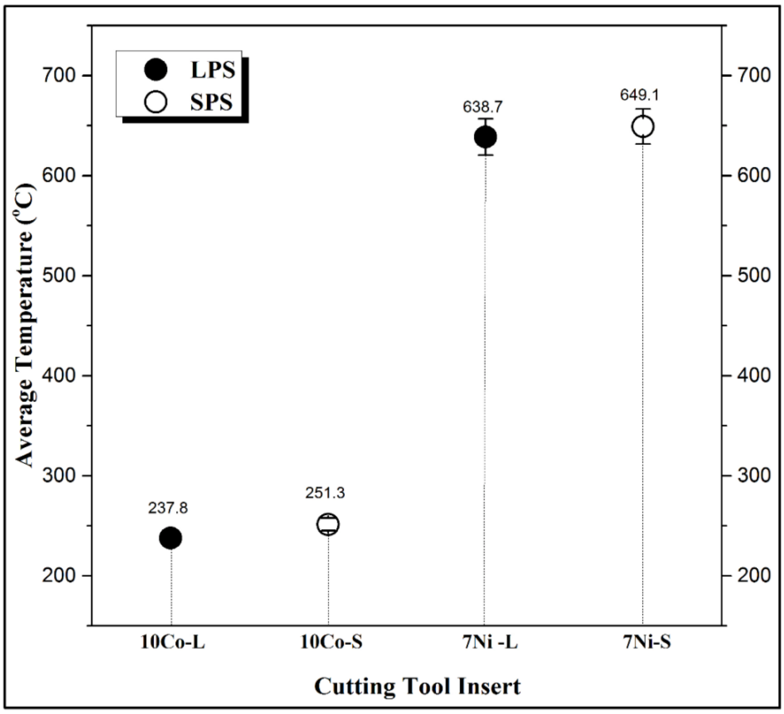

Figure 4.7: Variation in milling temperatures during dry milling at a v_c of 75m/minute and an a_p of 0.5mm

4.2.4 Analyses of temperature at a v_c of 100m/minute and a_p of 0.5mm

At a v_c of 100m/minute and an a_p of 0.5mm, the temperature experienced by the LPS inserts was lower than that of the SPS inserts (Table 4.7, Figure 4.8). The 10Co-L insert experienced the lowest temperature of 575.3 ± 13.5°C, while the 7Ni-S insert experienced the highest temperature of 866.4 ± 26.1°C (Figure 4.8).

Table 4.7: Average cutting temperature during dry milling at a v_c of 100m/minute and an a_p of 0.5mm

Sample abbreviation	Milling Conditions		Average Temperature [°C]
	v_c [m/minute]	a_p [mm]	
10Co-L	100	0.5	575.3 ± 13.5
10C0-S	100	0.5	712.5 ± 19.7
7Ni-L	100	0.5	641.3 ± 23.9
7Ni-S	100	0.5	866.4 ± 26.1

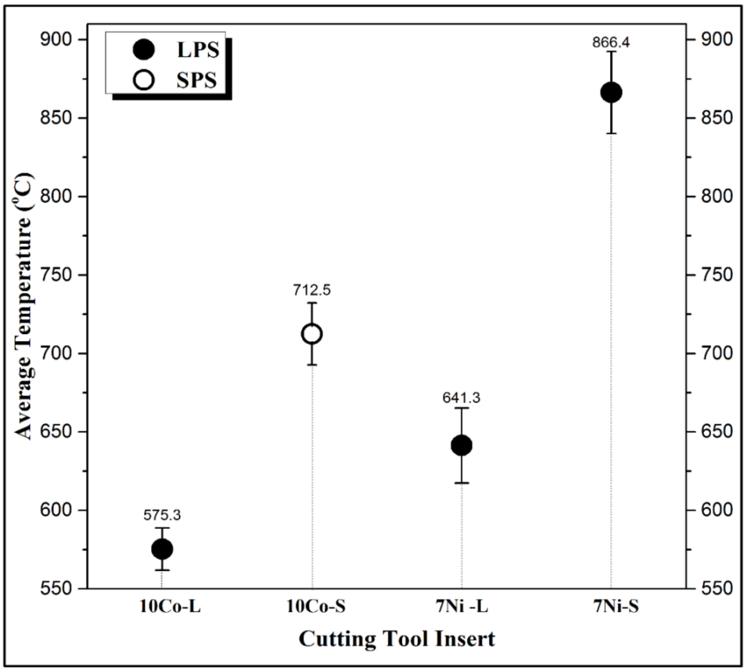

Figure 4.8: Variation in milling temperatures during dry milling at a v_c of 100m/minute and an a_p of 0.5mm

4.2.5 Effect of MQL on temperature at $\boldsymbol{v_c}$ of 75m/minute and an $\boldsymbol{a_p}$ of 0.5mm

The results for MQL milling at a v_c of 75m/minute and an a_p of 0.5mm shows that the temperatures experienced by the SPS inserts were lower than that of the LPS inserts (Table

4.8 and Figure 4.9). The 10Co-S inserts experienced the lowest temperature of 325.9 ± 8.8°C followed by the 7Ni-S insert with a fairly similar temperature of 326.4 ± 8.9°C (Figure 4.9). The 7Ni-L insert experienced the highest milling temperature of 375.9 ± 9.8°C (Figure 4.9).

Table 4.8: Average cutting temperature during MQL milling at a v_c of 75m/minute and an a_p of 0.5mm

Sample abbreviation	Milling Conditions		Average Temperature [°C]
	v_c [m/minute]	a_p [mm]	
10Co-L	75	0.5	364.4 ± 10.6
10C0-S	75	0.5	325.9 ± 8.8
7Ni-L	75	0.5	375.9 ± 9.8
7Ni-S	75	0.5	326.4 ± 8.9

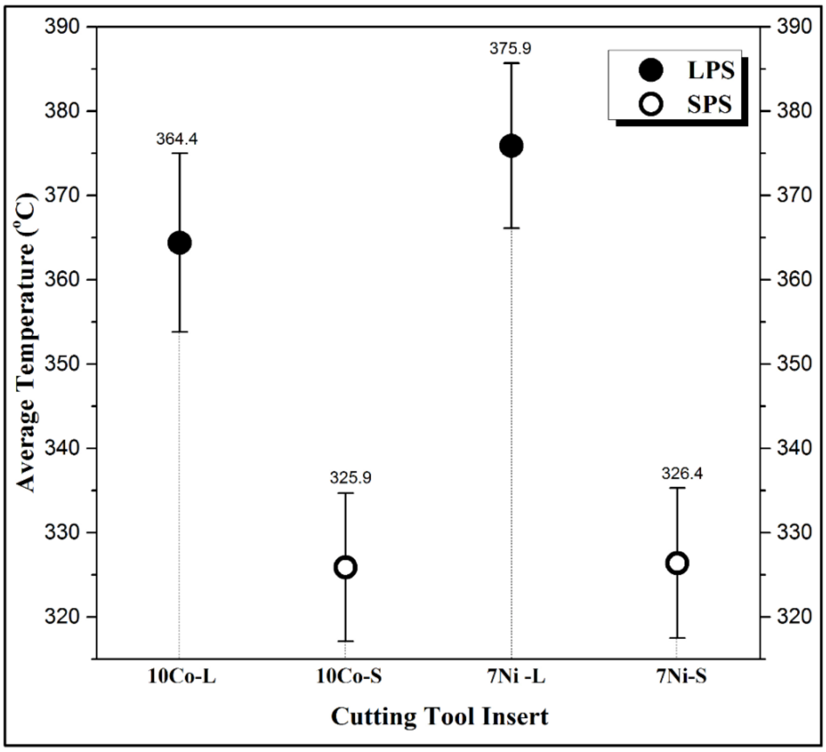

Figure 4.9: Variation in milling temperatures during MQL milling at a v_c of 75m/minute and an a_p of 0.5mm

4.2.6 Effect of MQL on temperature at $\boldsymbol{v_c}$ of 100m/minute and an $\boldsymbol{a_p}$ of 0.5mm

The results for MQL milling at a v_c of 100m/minute and an a_p of 0.5mm is shown that the temperatures experienced by the LPS inserts were lower than that of the SPS inserts (Table 4.9). The 7Ni-L insert experienced the lowest temperature of 398.5 ± 8.1°C, while the 7Ni-S insert experienced the highest temperature of 455.5 ± 10.8°C (Figure 4.10).

Table 4.9: Average cutting temperature during MQL milling at a v_c of 100m/minute and an a_p of 0.5mm

Sample abbreviation	Milling Conditions		Average Temperature [°C]
	v_c [m/minute]	a_p [mm]	
10Co-L	100	0.5	408.3 ± 10.8
10C0-S	100	0.5	446.9 ± 11.7
7Ni-L	100	0.5	398.5 ± 8.1
7Ni-S	100	0.5	455.5 ± 10.8

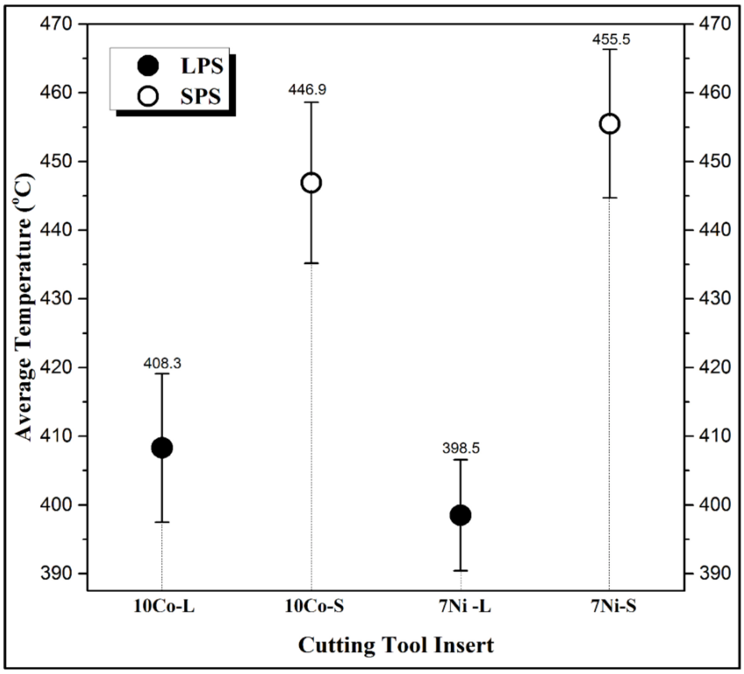

Figure 4.10: Variation in milling temperatures during MQL milling at a v_c of 100m/minute and an a_p of 0.5mm

4.2.7 Overall Trends

During the dry milling runs, the temperatures experienced by the 10Co-L insert were lower than that of the 10Co-S inserts (Figure 4.11). The 10Co-L and 10Co-S inserts experienced relatively low temperatures at a v_c of 75m/minute and an a_p of 0.5mm (Figure 4.11). At a a_p of 1mm, the milling temperature for the 10Co-L and 10Co-S inserts decreased with increase in cutting speed (Figure 4.11). Nevertheless as the a_p was reduced to 0.5mm, the temperature increased with increase in cutting speed (Figure 4.11). For a fixed a_p, the temperatures experienced by the 7Ni-L and 7Ni-S inserts increased with increase in cutting speed (Figure 4.12). During dry milling runs, the 7Ni-L and 7Ni-S inserts also experienced lowest temperature at a v_c of 75m/minute when a_p was recused to 0.5mm (Figure 4.12).

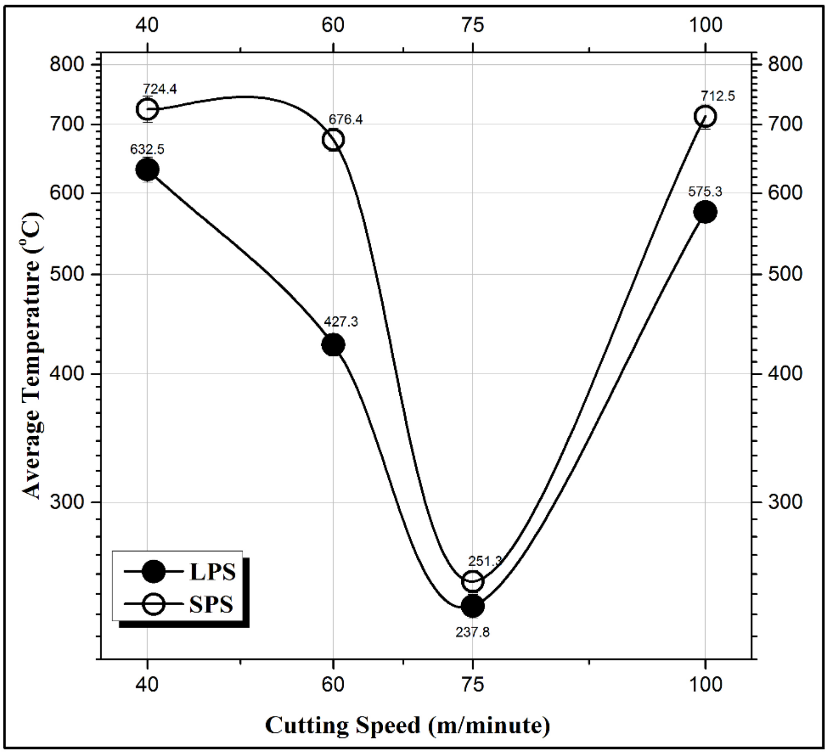

Figure 4.11: Variation in temperature with cutting speed for the 10Co-L and 10Co-S cutting tool inserts during dry milling of Ti-6Al-4V

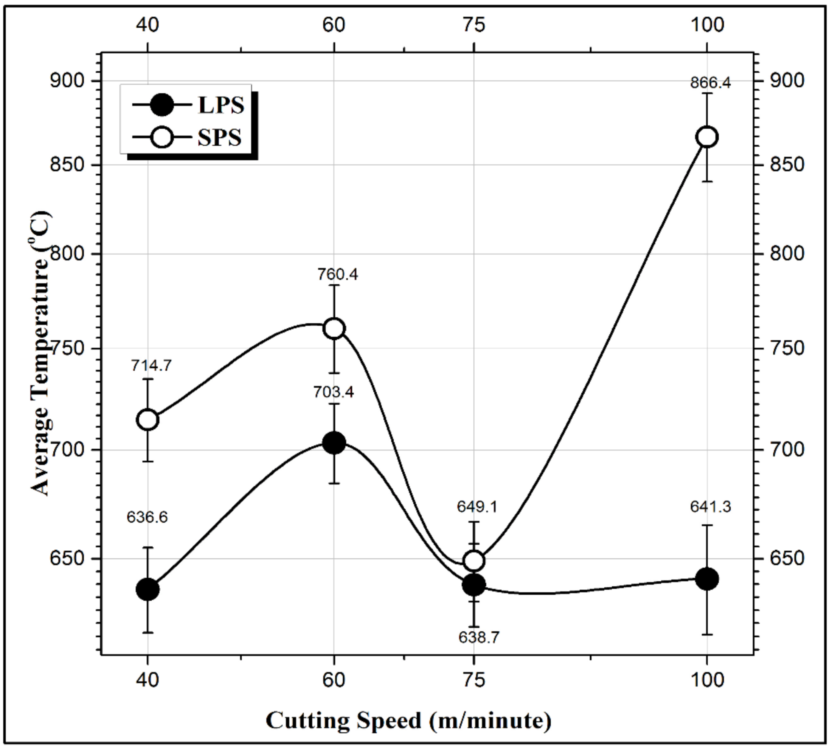

Figure 4.12: Variation in temperature with cutting speed for the 7Ni-L and 7Ni-S cutting tool inserts during dry milling of Ti-6Al-4V

During dry milling runs, the temperatures experienced by the 10Co-L insert were significantly lower than those experienced by the 7N-L cutting insert, although similarities in temperatures could be observed for both inserts during milling trials at a v_c of 40m/minute and an a_p of 1mm (Figure 4.13). The milling temperature for the 10Co-L and 10Co-S inserts increased with the application of MQL at a v_c of 75m/minutes and an a_p 0.5mm, while that of the 7Ni-L and 7Ni-S inserts decreased with the application of MQL at same speed and depth of cut (Figure 4.14). At a v_c of 100m/minutes and an a_p of 0.5mm, the temperature was lower for MQL milling runs than dry milling runs (Figure 4.15).

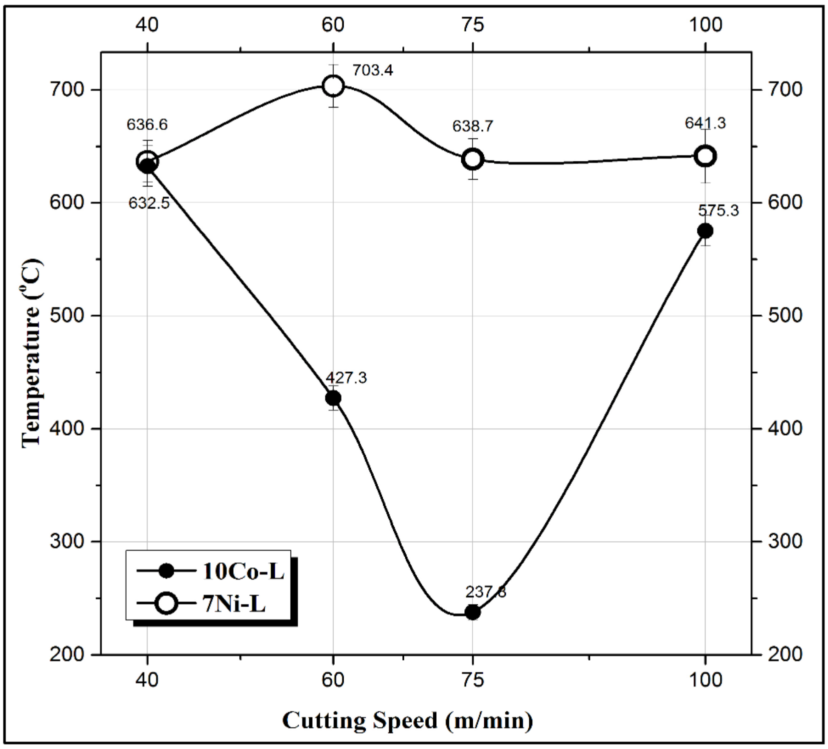

Figure 4.13: Variation in temperature with cutting speed for the 10Co-L and 7Ni-L cutting tool inserts during dry milling

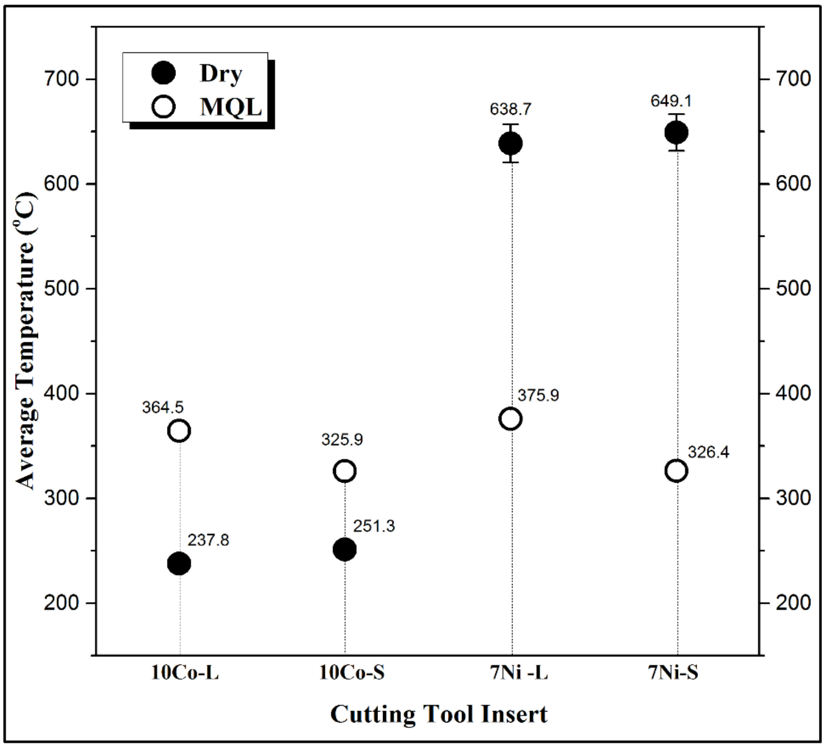

Figure 4.14: Variation in temperature for MQL and dry milling runs at a v_c of 75m/minute and an a_p 0.5mm

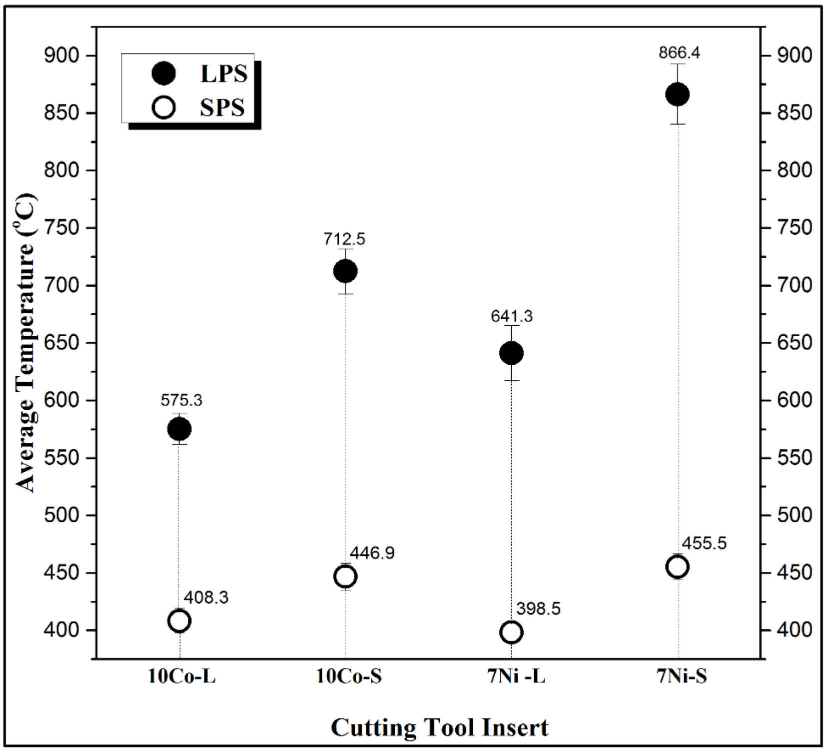

Figure 4.15: Variation in temperature MQL and dry milling runs at a v_c of 100m/minute and an a_p 0.5mm

The milling temperatures were also observed to be lower during MQL milling at a v_c of 75m/minute and an a_p 0.5mm, than at a v_c of100m/minute and an a_p 0.5mm (Figure 4.16).

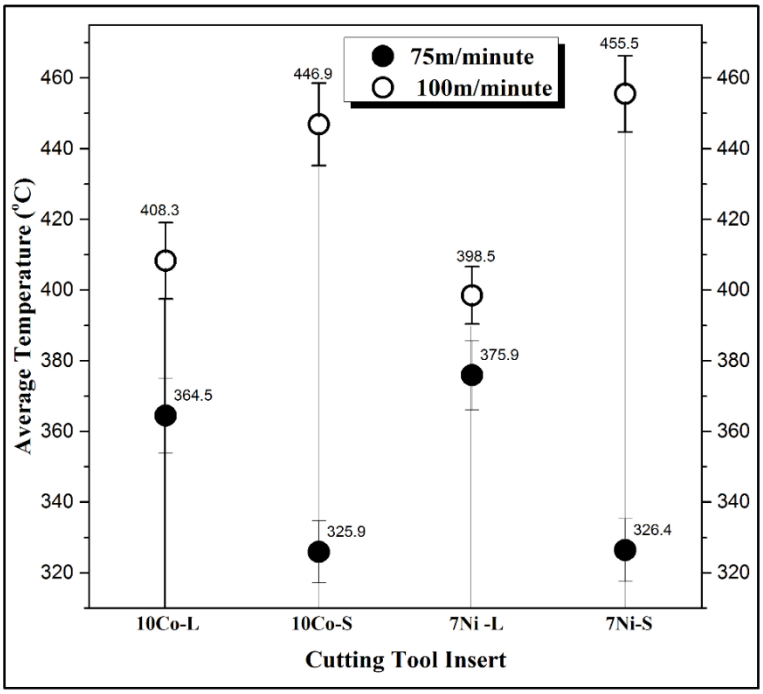

Figure 4.16: Variation in temperature for MQL milling runs at a v_c of 75m/minute and a_p of 0.5mm

4.3 Resultant force

The resultant forces during milling are suspected to be influenced by milling parameters. Therefore, the resultant forces data obtained from each milling run are analyzed in this chapter, in order to compare, as well as attempt to find correlations between the milling parameters and resultant force.

4.3.1 Analyses of resultant forces at a $\boldsymbol{v_c}$ 40m/minute and an $\boldsymbol{a_p}$ of 1mm

The average resultant forces experienced by the cutting tool inserts during milling runs at a v_c of 40m/minute and an a_p of 1mm are shown in Table 4.10. The resultant forces experienced by the LPS inserts were lower than that of the SPS inserts, except for the 11Ni-S insert which experienced a lower resultant force than the 11Ni-L insert (Figure 4.17).

Table 4.10: Average resultant forces for dry milling at a v_c of 40m/minute and an a_p of 1mm

Sample abbreviation	Milling Conditions		Average Resultant Force [N]
	v_c [m/minute]	a_p [mm]	
10Co-L	40	1	769.5 ± 15.4
10Co-S	40	1	1067.2 ± 21.3
11Ni-L	40	1	1092.7 ± 21.9
11Ni-S	40	1	619.8 ± 12.4
7Ni-L	40	1	516.3 ± 10.3
7Ni-S	40	1	875.4 ± 17.5
N-12Co-L	40	1	1313.4 ± 25.5
N-12Co-S	40	1	1363.6 ± 27.3

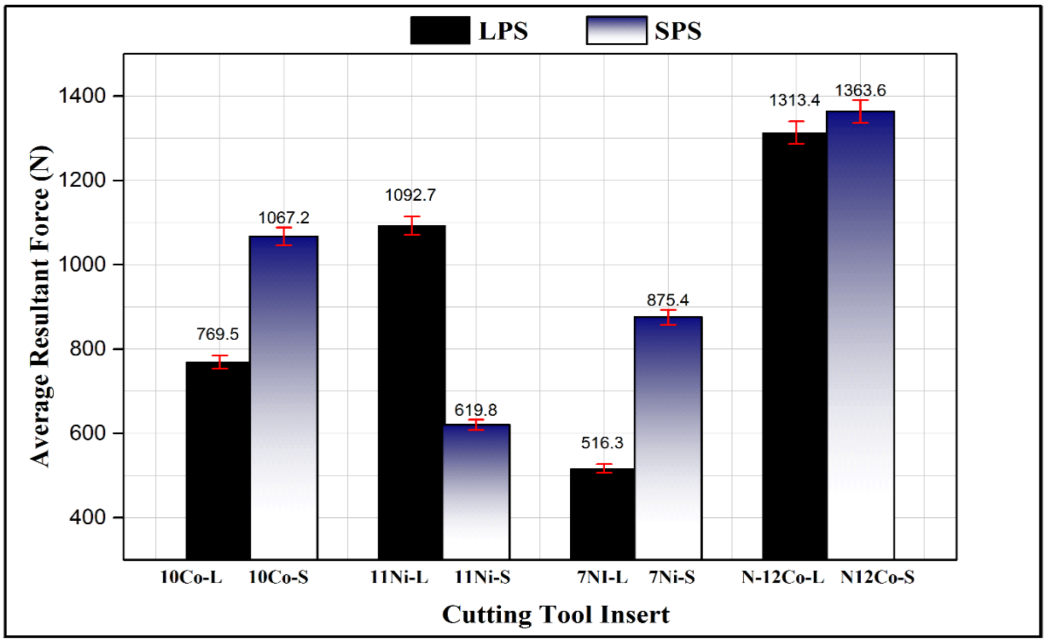

Figure 4.17: Comparison of average resultant forces for the 40m/minute v_c and 1mm a_p milling runs

The 7Ni-L insert experienced the lowest resultant force of 516.3 ± 10.3N, followed by the 11Ni-S and 10Co-L inserts respectively (Figure 4.17). The N-12Co-L and N-12Co-S insert experienced the higher resultant forces of 1313.4 ± 26.3N and 1363.6 ± 27.3N respectively

(Table 4.10). A significant increase (inflection) in the resultant force experienced by the N-12C0-L insert after 105 seconds of milling is shown in Figure 4.18.

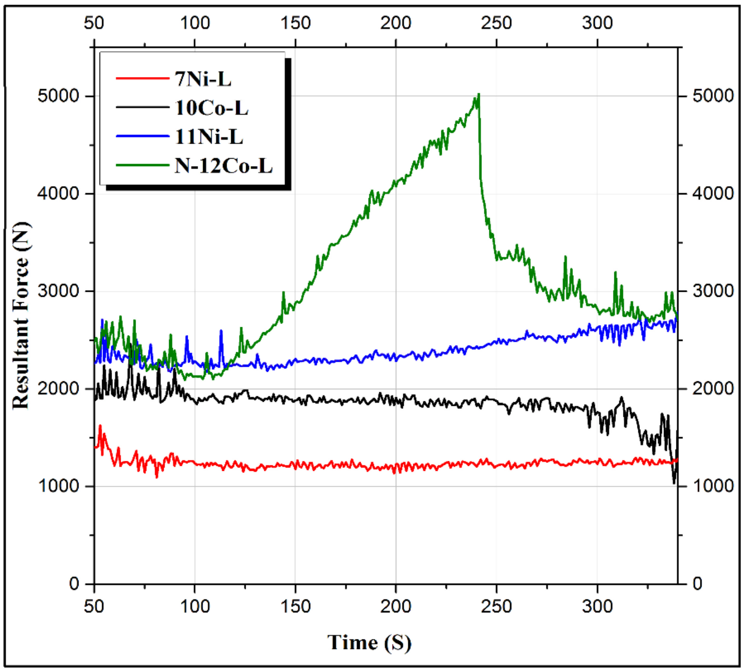

Figure 4.18: Variation in resultant forces with time for cutting tool inserts during dry milling at a v_c of 40m/minute and an a_p of 1mm

4.3.2 Analyses of resultant forces at a $\boldsymbol{v_c}$ 60m/minute and an $\boldsymbol{a_p}$ of 1mm

At a v_c of 60m/minute and an a_p of 1m, the resultant forces experienced by the LPS inserts were lower than those of the SPS inserts. The only exception to this trend was the 7Ni-S insert which experienced a lower resultant force than the 7Ni-L insert (Table 4.11 and Figure 4.19). The 10Co-L insert experienced the lowest resultant force of 640.9 ± 12.8N, while the 7Ni-L insert experienced the highest resultant force of 906.6 ± 18.1N (Figure 4.20).

Table 4.11: Average resultant forces during dry milling at a v_c of 60m/minute and an a_p of 1mm

Sample abbreviation	Milling Conditions		Average Resultant Force [N]
	v_c [m/minute]	a_p [mm]	
10Co-L	60	1	640.9 ± 12.8
10C0-S	60	1	676.8 ± 13.5
11Ni-L	60	1	726.1 ± 14.5
11Ni-S	60	1	745.1 ± 14.9
7Ni-L	60	1	906.6 ± 18.1
7Ni-S	60	1	799.1 ± 15.9

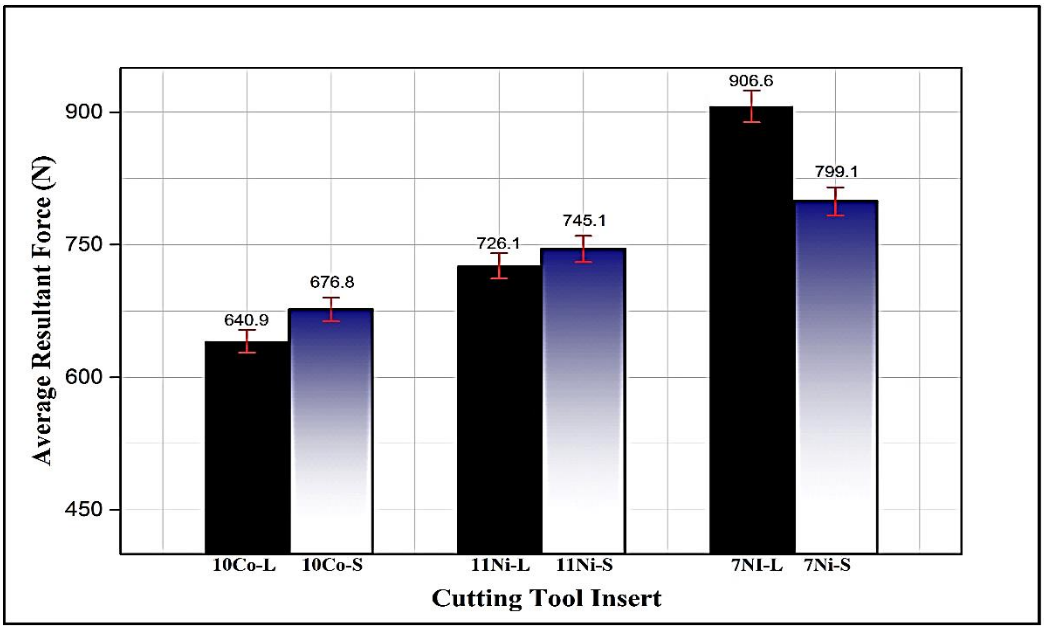

Figure 4.19: Comparison of average resultant forces for the 60m/minute v_c and 1mm a_p milling runs

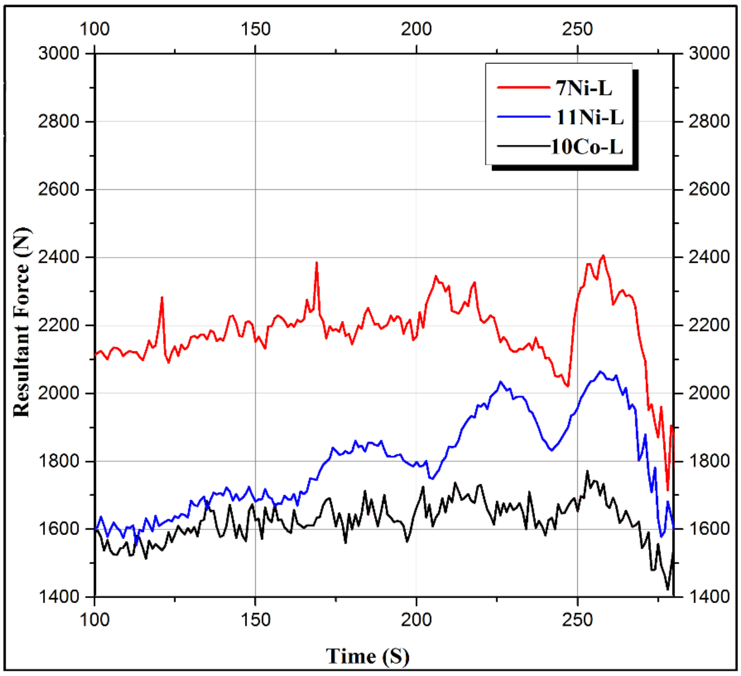

Figure 4.20: Variation in resultant forces with time for cutting tool inserts during dry milling at a v_c of 60m/minute and an a_p of 1mm

4.3.3 Analyses of resultant forces at a $\boldsymbol{v_c}$ 75m/minute and an $\boldsymbol{a_p}$ of 0.5mm

The milling results at a v_c of 75m/minute and an a_p of 0.5mm shows that the SPS inserts experienced lower resultant forces than that the LPS inserts (Table 4.12). The 7Ni-L insert experienced the lowest resultant force of 424.3 ± 8.5N, while the 10Co-S insert experienced the highest resultant force of 542.5 ± 10.9 N (Figure 4.21).

Table 4.12: Average resultant forces during dry milling at a v_c of 75m/minute and an a_p of 0.5mm

Sample abbreviation	Milling Conditions		Average Resultant Force [N]
	v_c [m/minute]	a_p [mm]	
10Co-L	75	0.5	503.1 ± 10.1
10C0-S	75	0.5	542.5 ± 10.9
7Ni-L	75	0.5	424.3 ± 8.5
7Ni-S	75	0.5	463.9 ± 9.3

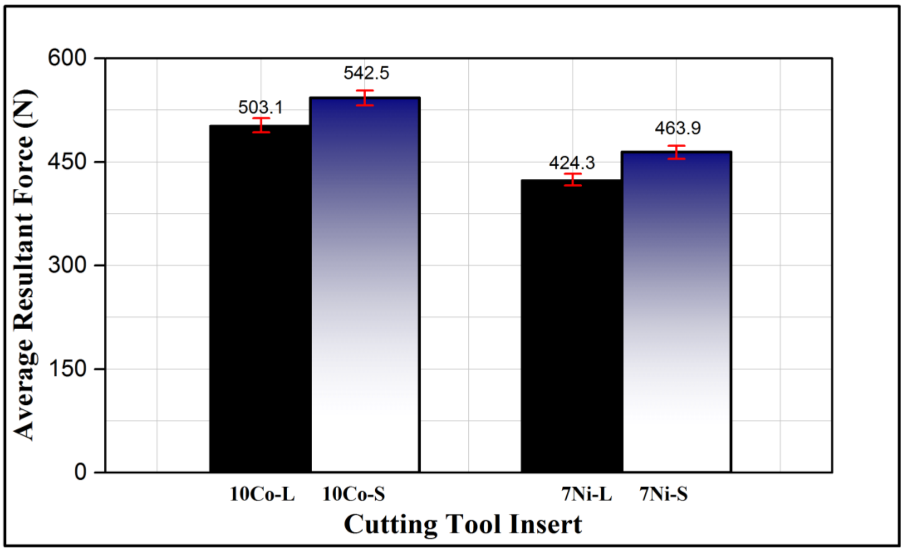

Figure 4.21: Comparison of average resultant forces for the 75m/minute v_c and 0.5mm a_p milling runs

4.3.4 Analyses of resultant forces at a $\boldsymbol{v_c}$ 100m/minute and an $\boldsymbol{a_p}$ of 0.5mm

At a v_c of 100m/minute and an a_p of 0.5mm, the resultant forces experienced by the LPS inserts were lower than those for the SPS inserts (Table 4.13). The 10Co-S insert experienced the lowest resultant force of 301.9 ± 6.1N, while the 7Ni-S insert experienced the highest resultant force of 754.9 ± 15.1N (Figure 4.22). The 10Co-S and 11Ni-S inserts experienced similar resultant forces of 523.8 ± 10.5°C and 520.2 ± 10.4 °C respectively (Figure 4.22).

Table 4.13: Average resultant forces during dry milling at a v_c of 100m/minute and an a_p of 0.5mm

Sample abbreviation	Milling Conditions		Average Resultant Force [N]
	v_c [m/minute]	a_p [mm]	
10Co-L	100	0.5	301.9 ± 6.1
10C0-S	100	0.5	523.8 ± 10.5
7Ni-L	100	0.5	520.2 ± 10.4
7Ni-S	100	0.5	754.9 ± 15.1

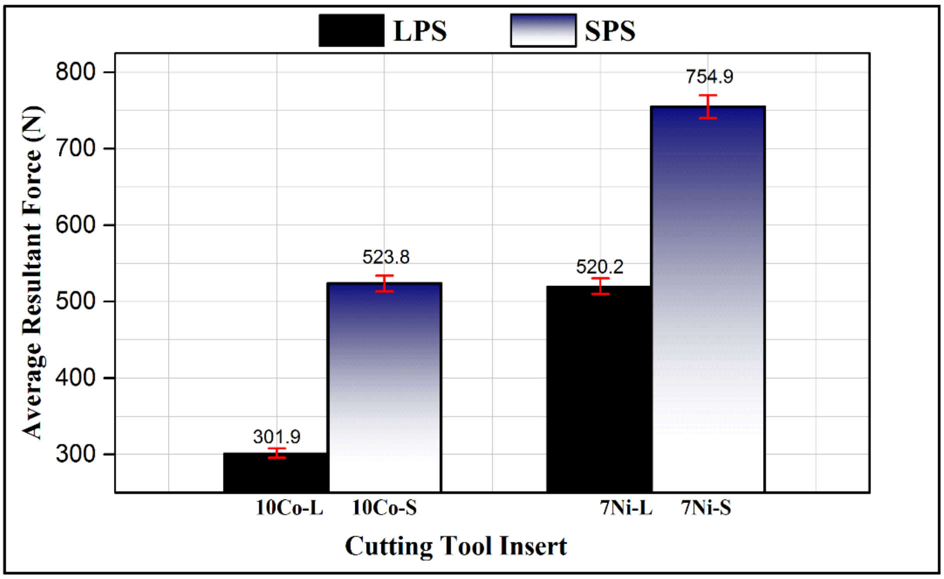

Figure 4.22: Comparison of average resultant forces for the 100m/minute v_c and 0.5mm a_p milling runs

4.3.5 Effect of MQL on resultant forces at $\boldsymbol{v_c}$ of 75m/min and an $\boldsymbol{a_p}$ of 0.5mm

During MQL milling runs at a v_c of 75m/minute and an a_p of 0.5mm, the LPS inserts experienced significantly lower resultant forces than the SPS inserts (Table 4.14 and Figure 4.23).

Table 4.14: Average resultant forces during MQL milling at a v_c of 75m/minute and an a_p of 0.5mm

Sample abbreviation	Milling Conditions		Average Resultant Force [N]
	v_c [m/minute]	a_p [mm]	
10Co-L	75	0.5	387.8 ± 7.8
10C0-S	75	0.5	633.8 ± 12.7
7Ni-L	75	0.5	398.7 ± 7.9
7Ni-S	75	0.5	585.8 ± 11.7

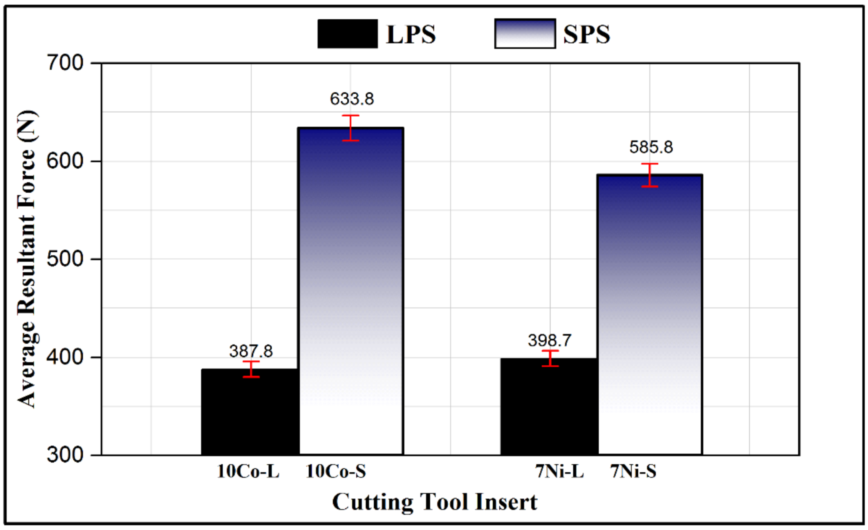

Figure 4.23: Comparison of average resultant forces for the 75m/minute v_c and 0.5mm a_p MQL milling runs

The average resultant force experienced by the 10Co-L insert was slightly lower than that of the 7Ni-L insert, although the plot of resultant force versus time for both cutting tool inserts reveals that the 10Co-L insert experienced a fairly higher temperature during the first 82 seconds of milling (Figure 4.23 and Figure 4.24).

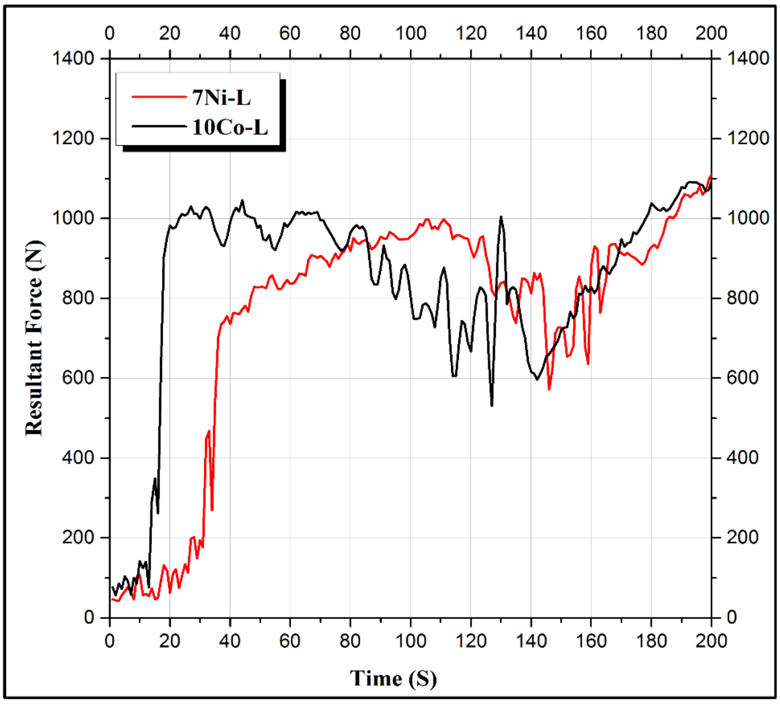

Figure 4.24: Variation in resultant forces with time for the 7Ni-L and 10Co-L inserts after milling with MQL at a v_c of 75m/minute and an a_p of 0.5mm

4.3.6 Effect of MQL on resultant forces at $\boldsymbol{v_c}$ of 75m/min and an $\boldsymbol{a_p}$ of 0.5mm

The resultant forces experienced by the cutting tool inserts during MQL milling runs at a v_c of 100m/minute and an a_p of 0.5mm is shown in Table 4.15. It can be observed that the 7Ni-L and 7Ni-S inserts experienced relatively lower resultant forces than that of the 10Co-L and 10Co-S inserts (Figure 4.25). The 7Ni-L insert experienced the lowest resultant force of 323.5 ± 6.5N, while the 10Co-L insert experienced the highest resultant force of 717.6 ± 14.4N (Figure 4.25). The resultant force experienced by the 10Co-L and 10C0-S inserts were fairly similar (Figure 4.25).

Table 4.15: Average resultant forces during MQL milling at a v_c of 100m/minute and an a_p of 0.5mm

Sample abbreviation	Milling Conditions		Average Resultant Force [N]
	v_c [m/minute]	a_p [mm]	
10Co-L	100	0.5	717.6 ± 14.4
10C0-S	100	0.5	714.4 ± 14.3
7Ni-L	100	0.5	323.5 ± 6.5
7Ni-S	100	0.5	548.7 ± 10.9

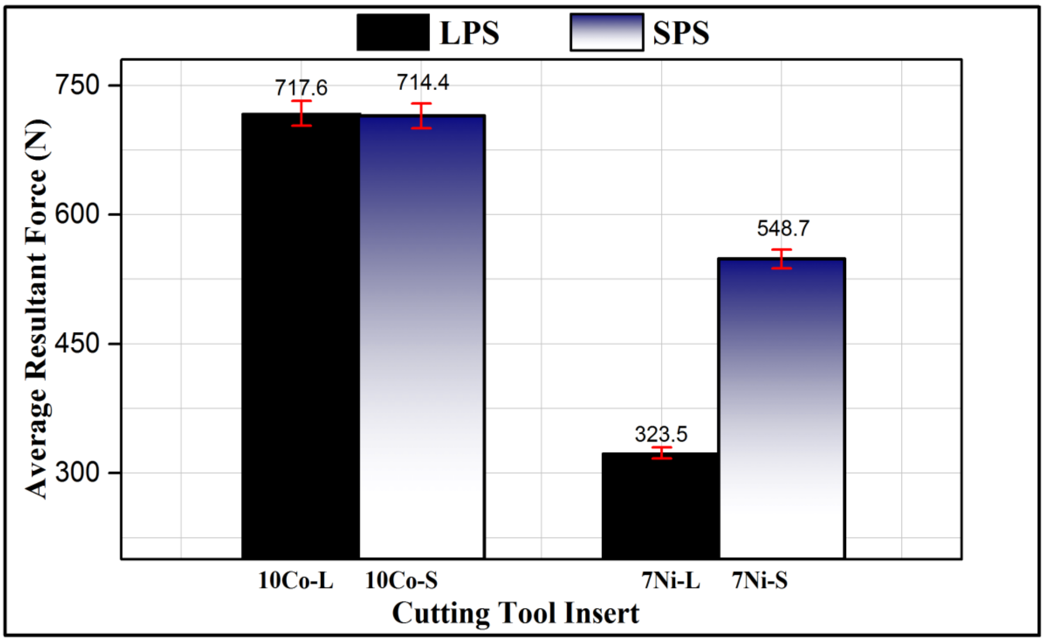

Figure 4.25: Comparison of average resultant forces for the 100m/minute v_c and 0.5mm a_p MQL milling runs

4.3.7 Overall Trends

A series of trends could be established for the resultant forces experienced by the inserts during the milling runs. The 10Co-L and 10Co-S inserts experienced lower resultant forces with decrease in cutting speed, while the 7Ni-L and 7Ni-S inserts experienced higher resultant forces with increase in cutting speed, for a fixed depth of cut (Figure 4.26, Figure 4.27). The cutting tool inserts experienced decreased resultant forces with decrease in depth of cut (Figure 4.26, Figure 4.27). The LPS inserts generally experienced lower resultant forces than the SPS inserts during the dry milling runs (Figure 4.26, Figure 4.27).

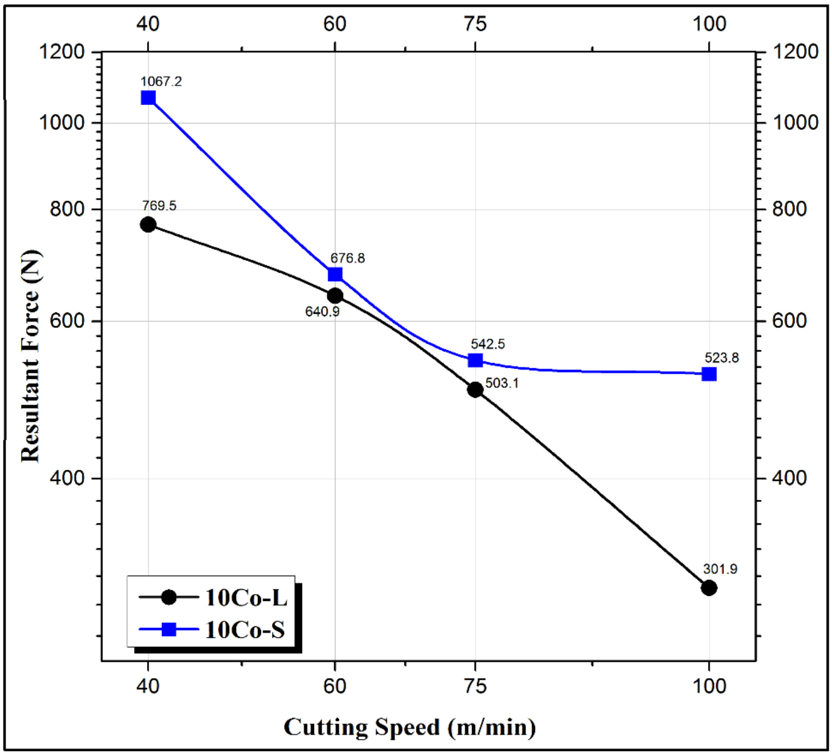

Figure 4.26: Variation in resultant forces with cutting speed for the 10Co-L and 10Co-S cutting tool inserts during dry milling runs

The resultant forces experienced by the 10Co-L and 10Co-S inserts during MQL milling runs were lower at a v_c of 75m/minute than at 100m/minute, while the resultant forces experienced by the 7Ni-L and 7Ni-S inserts were lower during MQL milling runs at 100m/minute than at 75m/minute (Figure 4.28). At a v_c of 75m/minute and an a_p 0.5mm, the LPS inserts experienced lower resultant forces with MQL application, while the SPS inserts experienced higher resultant forces with MQL application (Figure 4.29). At a v_c of 100m/minute and an a_p 0.5mm, the resultant forces for the 10Co-L and 10Co-S inserts increased with the application of MQL, while that of the 7Ni-L and 7Ni-S inserts decreased with the application of MQL (Figure 5.30). The resultant forces experienced by the 10Co-L and 10Co-S inserts was lower during dry milling at a v_c of 100m/minute and an a_p of 0.5mm (Figure 5.29 and Figure 5.30).

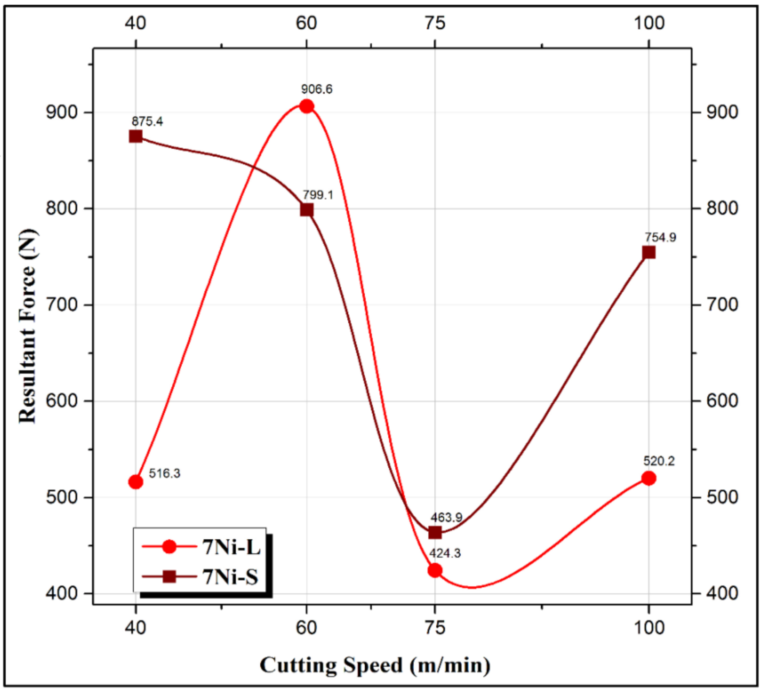

Figure 4.27: Variation in resultant forces with cutting speed for the 7Ni-L and 7Ni-S cutting tool inserts during dry milling of Ti-6Al-4V

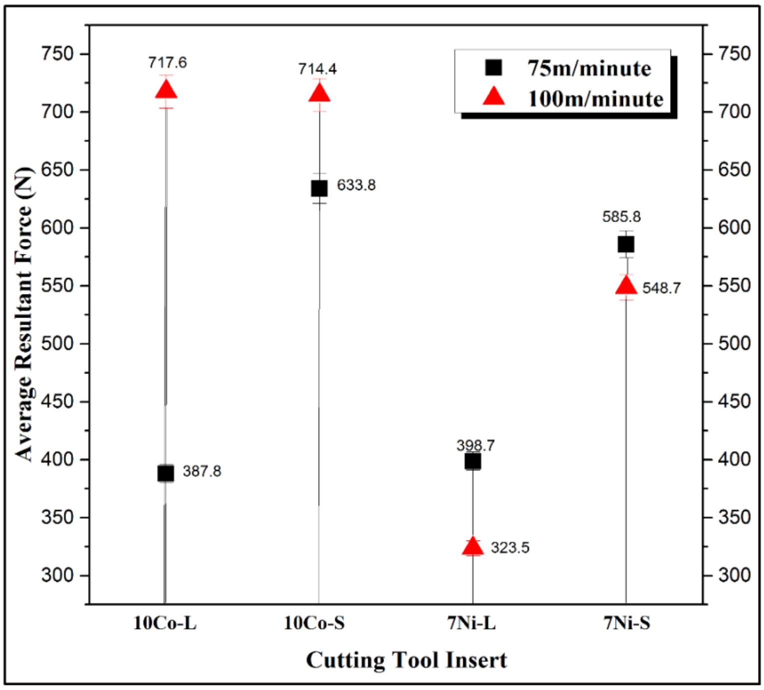

Figure 4.28: Variation of resultant forces during MQL milling at 75m/minute and 100m/minute

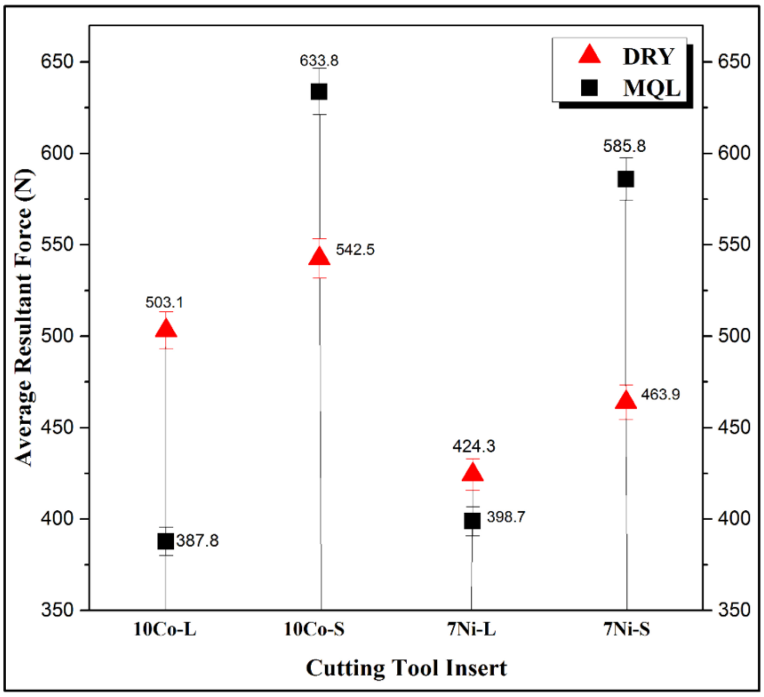

Figure 4.29: Variation of resultant forces in MQL and dry milling at a v_c of 75m/minute and an a_p 0.5mm

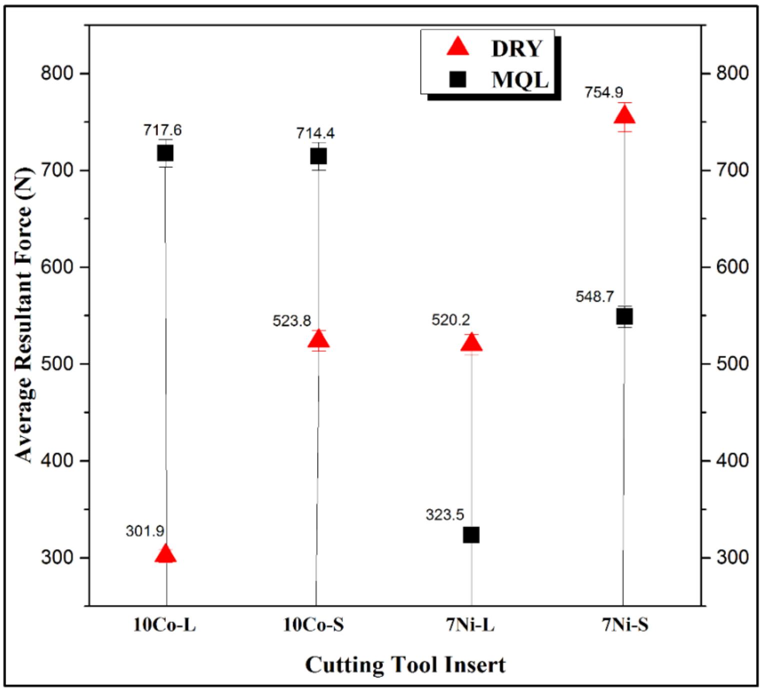

Figure 4.30: Variation of resultant forces in MQL and dry milling at a v_c of 100m/minute and an a_p 0.5mm

4.4 Tool wear

The milling parameters were suspected to influence the Flank Wear Rate (FWR) of the cutting tool inserts. Therefore, the FWR data obtained from each milling run are analyzed in this chapter, in order to compare, as well as attempt to find correlations between FWR and the milling parameters. Only selected micrographs have been included in this section.

4.4.1 Analyses of tool wear at a $\boldsymbol{v_c}$ 40m/minute and an $\boldsymbol{a_p}$ of 1mm

The micrographs of the inserts cutting edges after milling at a v_c of 40m/minute and an a_p of 1mm show that the LPS inserts experienced lower flank wear rate (FWR) than the SPS inserts (Figure 4.31 and Table 4.16). The only exception to this trend was the 11Ni-L insert which had a higher FWR than the 11Ni-S insert (Table 4.16, Figure 4.31). The 10Co-L insert had the lowest FWR of 17.9m/minute, while the 11Ni-S and 7Ni-L inserts had similar FWR of 75.89m/minute and 76.19m/minute respectively (Figure 4.31a, 4.31b and 4.31c). The cutting edges of the N-12Co-L and N-12Co-S inserts were completely damaged (catastrophic failure) hence, making them the inserts with highest FWR (Figure 4.31f).

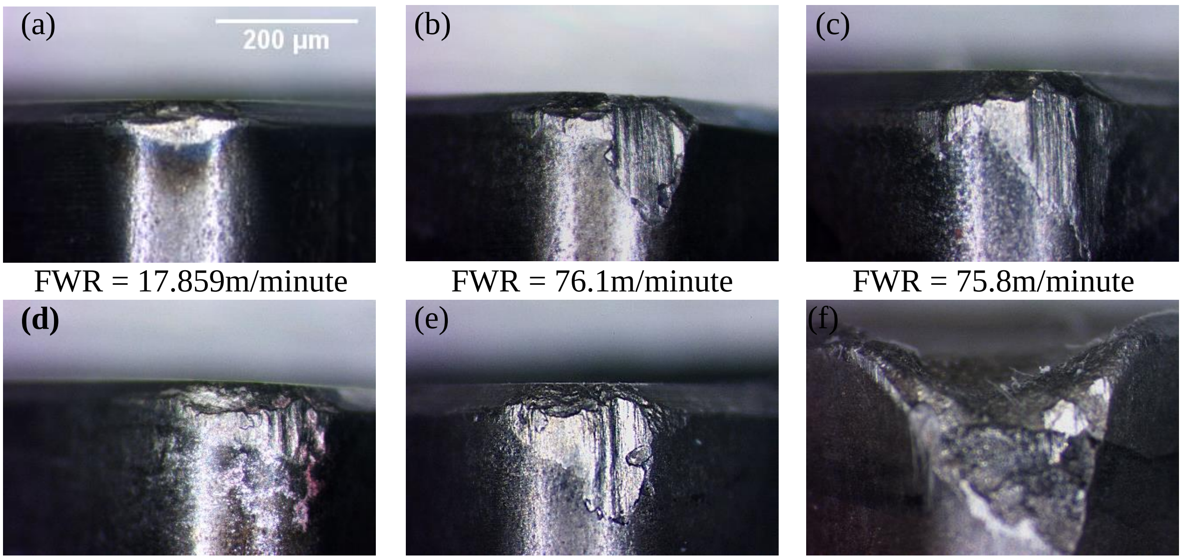

FWR = 17.859m/minute | FWR = 76.1m/minute | FWR = 75.8m/minute

FWR = 31.8m/minute | FWR = 77.5m/minute | FWR = Failure

Figure 4.31: Flank wear rate for: (a) 10Co-L, (b) 7Ni-L, (c) 11Ni-L, (d) 10Co-S, (e) 7Ni-S, (f) N-12Co-L inserts after dry milling at a v_c of 40m/minute and an a_p of 1mm

Table 4.16: Flank wear rate for cutting tool inserts after dry milling at a v_c of 40m/minute and an a_p of 1mm

Sample abbreviation	Milling Conditions		Flank Wear Rate [m/minute]
	v_c [m/minute]	a_p [mm]	
10Co-L	40	1	17.9
10Co-S	40	1	31.8
11Ni-L	40	1	102.1
11Ni-S	40	1	75.8
7Ni-L	40	1	76.1
7Ni-S	40	1	77.5
N-12Co-L	40	1	Failure
N-12Co-S	40	1	Failure

4.4.2 Analyses of tool wear at a v_c 60m/minute and an a_p of 1mm

At a v_c of 60m/minute and an a_p of 1mm, the LPS inserts had lower FWR than the SPS inserts (Table 4.17). The only exception to this trend was the 10Co-S insert which had the lowest FWR of 27.3m/minute (Figure 4.32). The FWR for the 11Ni-L insert was observed to be lower than that of the 7Ni-L insert (Figure 4.32b and 4.32c). The 7Ni-S insert had the highest FWR of 154.1m/minute (Figure 4.32f).

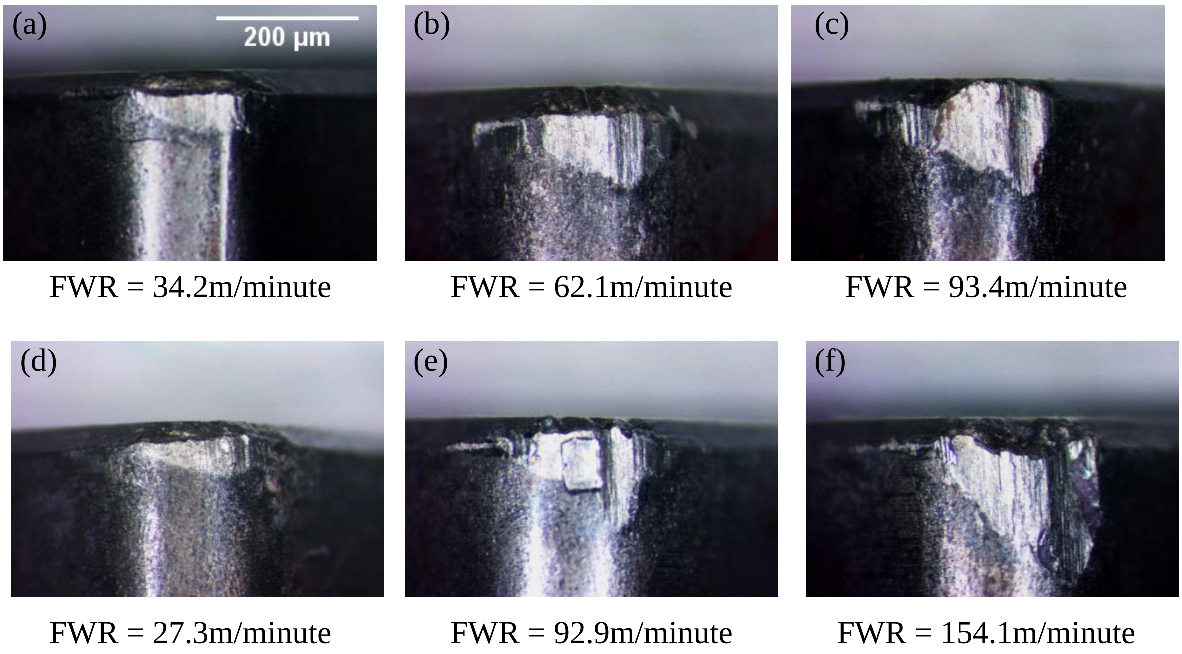

Figure 4.32: Flank wear rate for: (a) 10Co-L, (b) 11Ni-L, (c) 7Ni-L, (d) 10Co-S, (e) 11Ni-S, (f) 7Ni-S inserts after milling at a v_c of 60m/minute and an a_p of 1mm

Table 4.17: Flank wear rate for cutting tool inserts after dry milling at a v_c of 60m/minute and an a_p of 1mm

Sample abbreviation	Milling Conditions		Flank Wear Rate [m/minute]
	v_c (m/minute)	a_p (mm)	
10Co-L	60	1	36.2
10C0-S	60	1	27.3
11Ni-L	60	1	62.1
11Ni-S	60	1	92.9
7Ni-L	60	1	93.4
7Ni-S	60	1	154.1

4.4.3 Analyses of tool wear at a $\boldsymbol{v_c}$ 75m/minute and an $\boldsymbol{a_p}$ of 0.5mm

The micrographs of the cutting tool inserts after milling at a v_c of 75m/minute and an a_p of 0.5mm shows that the LPS inserts experienced lower FWR than the SPS inserts (Figure

4.33). The FWR for the 10Co-L and 10Co-S inserts were lower than that of the 7Ni-L and 7Ni-S insert (Table 4.18 and Figure 4.33). The 10Co-L insert had the lowest FWR of 54.3m/minute, while the 7Ni-S insert had the highest FWR 94.9 m/minute (Figure 4.33a and 4.33d).

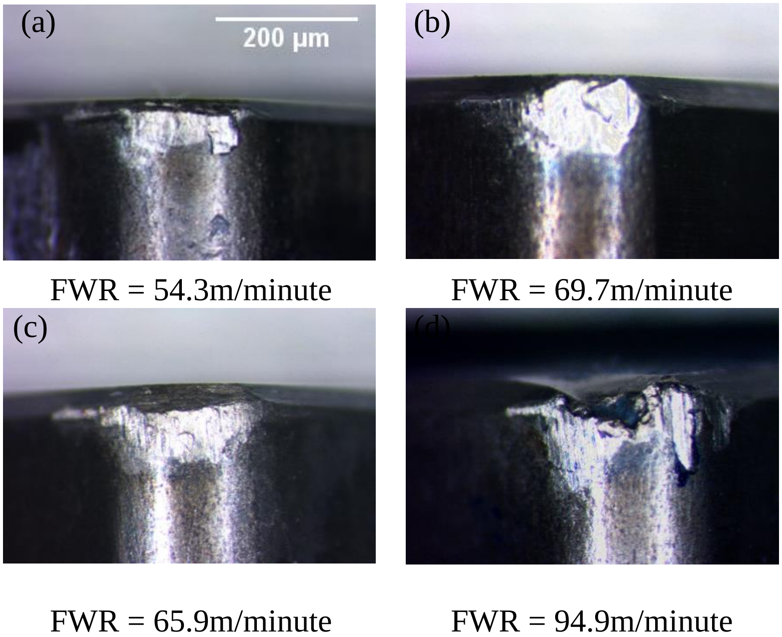

Figure 4.33: Flank wear rate for: (a) 10Co-L, (b) 7Ni-L, (c) 10Co-S, (d) 7Ni-S inserts after milling at a v_c of 75m/minute and an a_p of 0.5mm

Table 4.18: Flank wear rate for cutting tool inserts after dry milling at a v_c of 75m/minute and an a_p of 0.5mm

Sample abbreviation	Milling Conditions		Flank Wear Rate (m/minute)
	v_c [m/minute]	a_p [mm]	
10Co-L	75	0.5	54.3
10C0-S	75	0.5	65.9
7Ni-L	75	0.5	69.7
7Ni-S	75	0.5	94.9

4.4.4 Analyses of tool wear at a $\boldsymbol{v_c}$ 100m/minute and an $\boldsymbol{a_p}$ of 0.5mm

The optical micrographs of the inserts edge after milling runs at a v_c of 100m/minute and an a_p of 0.5mm shows that the FWR for the LPS inserts was lower than that of the SPS inserts (Figure 4.34). The 10Co-L insert had the lowest FWR of 77.8m/minute, while the 7Ni-S insert had the highest FWR of 133.2m/minute (Figure 4.34a and 4.34d and Table 4.19).

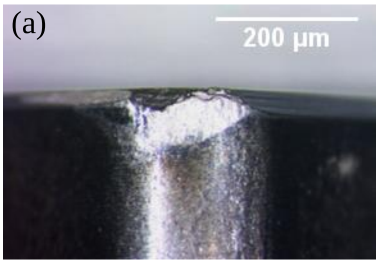

FWR = 77.8m/minute

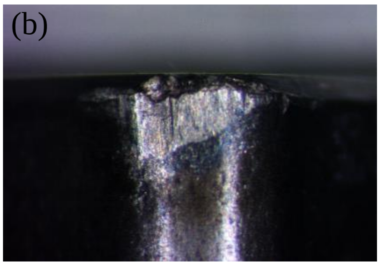

FWR = 100.5m/minute

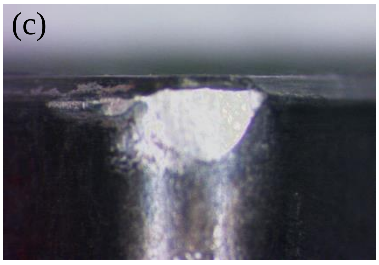

FWR = 112.6m/minute

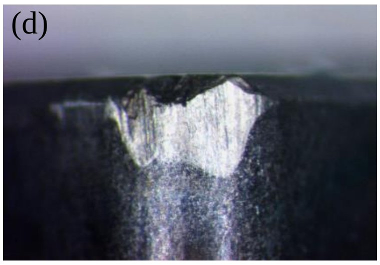

FWR = 133.2m/minute

Figure 4.34: Flank wear rate for: (a) 10Co-L, (b) 7Ni-L, (c) 10Co-S, (d) 7Ni-S inserts after dry milling at a v_c of 100m/minute and an a_p of 0.5mm

Table 4.19: Flank wear rate for cutting tool inserts after dry milling at a v_c of 100m/minute and an a_p of 0.5mm

Sample Abbreviation	Milling Conditions		Flank Wear Rate (m/minute)
	v_c (m/minute)	a_p (mm)	
10Co-L	100	0.5	77.8
10C0-S	100	0.5	112.6
7Ni-L	100	0.5	100.5
7Ni-S	100	0.5	133.2

4.4.5 Effect of MQL on tool wear at v_c of 75m/minute and an a_p of 0.5mm

The micrographs of the cutting tool inserts after MQL milling at a v_c of 75m/minute and an a_p of 0.5mm shows that the LPS inserts had lower FWR than the inserts (Figure 4.35, Table 4.20). The 10Co-L insert had the lowest FWR of 45.3m/minute, while the 7Ni-S insert had the highest FWR of 88.7m/minute (Figure 4.35a and 4.35d).

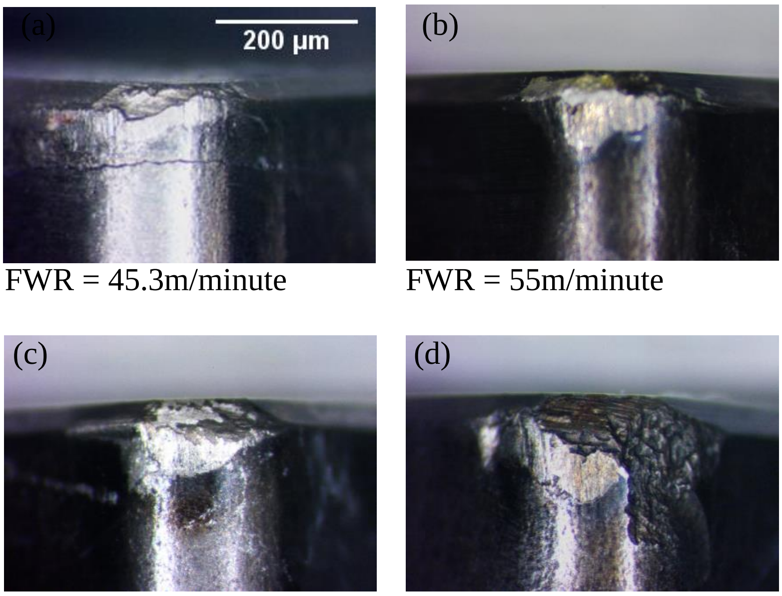

FWR = 45.3m/minute   FWR = 55m/minute

FWR = 60.9m/minute   FWR = 88.7m/minute

Figure 4.35: Flank wear rate for: (a) 10Co-L, (b) 7Ni-L, (c) 10Co-S, (d) 7Ni-S inserts after MQL milling at a v_c of 75m/minute and an a_p of 0.5mm

Table 4.20: Flank wear rate for cutting tool inserts after MQL milling at a v_c of 75m/minute and an a_p of 0.5mm

Sample abbreviation	Milling Conditions		Flank Wear Rate [m/minute]
	v_c [m/minute]	a_p [mm]	
10Co-L	75	0.5	45.3
10C0-S	75	0.5	60.9
7Ni-L	75	0.5	55
7Ni-S	75	0.5	88.7

4.4.6 Effect of MQL on tool wear at $\boldsymbol{v_c}$ of 100m/minute and an $\boldsymbol{a_p}$ of 0.5mm

The micrographs of the cutting tool inserts after milling a v_c of 100m/minute and an a_p of 0.5mm is shown in Figure 4.36. It can be observed that the FWR for the SPS inserts was lower than that of the LPS inserts (Figure 4.36, Table 4.21). The 10Co-L insert had the lowest FWR of 116.5m/minute, while the 7Ni-L had the highest FWR of 180.3m/minute (Figure 4.36a and Figure 4.36b).

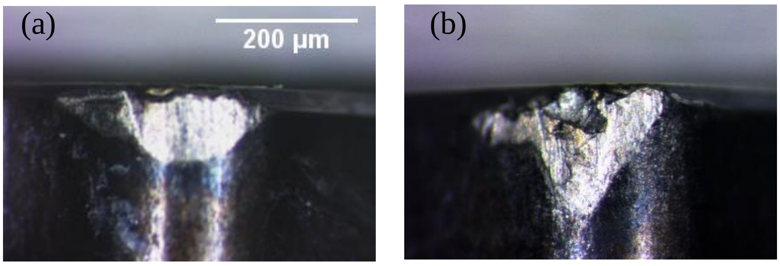

FWR = 125.3m/minute FWR = 180.3m/minute

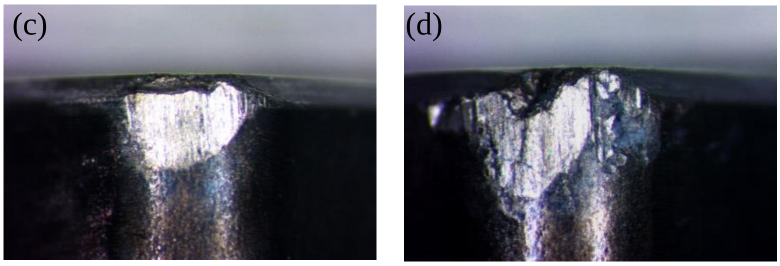

FWR = 116.5m/minute FWR = 170.5m/minute

Figure 4.36: Flank wear rate for: (a) 10Co-L, (b) 7Ni-L, (c) 10Co-S, (d) 7Ni-S inserts after MQL milling at a v_c of 100m/minute and an a_p of 0.5mm

Table 4.21: Flank wear rate for cutting tool inserts after MQL milling at a v_c of 100m/minute and an a_p of 0.5mm

Sample abbreviation	Milling Conditions		Flank Wear Rate [m/minute]
	v_c [m/minute]	a_p [mm]	
10Co-L	100	0.5	126.3
10C0-S	100	0.5	116.5
7Ni-L	100	0.5	180.3
7Ni-S	100	0.5	170.5

4.4.7 Overall Trends

Several trends could be established between the flank wear rates of the cutting tool inserts and the cutting speed/depth of cut. The FWR for the 10Co-L insert increased with increase in cutting speed irrespective of changes in the depth of cut (Figure 4.37). At an a_p of 1mm, the FWR for all the cutting tool inserts increased with increase in cutting speed, except for the FWR of the 10Co-S and 11Ni-L inserts (Figure 4.37). At a decreased a_p of 0.5mm, the FWR for all the cutting tool inserts increased with increase in cutting speed at a decreased a_p of 0.5mm (Figure 4.37). The application of MQL at a v_c of 75m/minute and an a_p of 0.5m reduced the FWR for all the cutting tool inserts (Figure 4.38). Nevertheless at an increased v_c of 100m/minute the application of MQL increased the FWR for all the cutting tool inserts (Figure 4.38 and 4.39.).

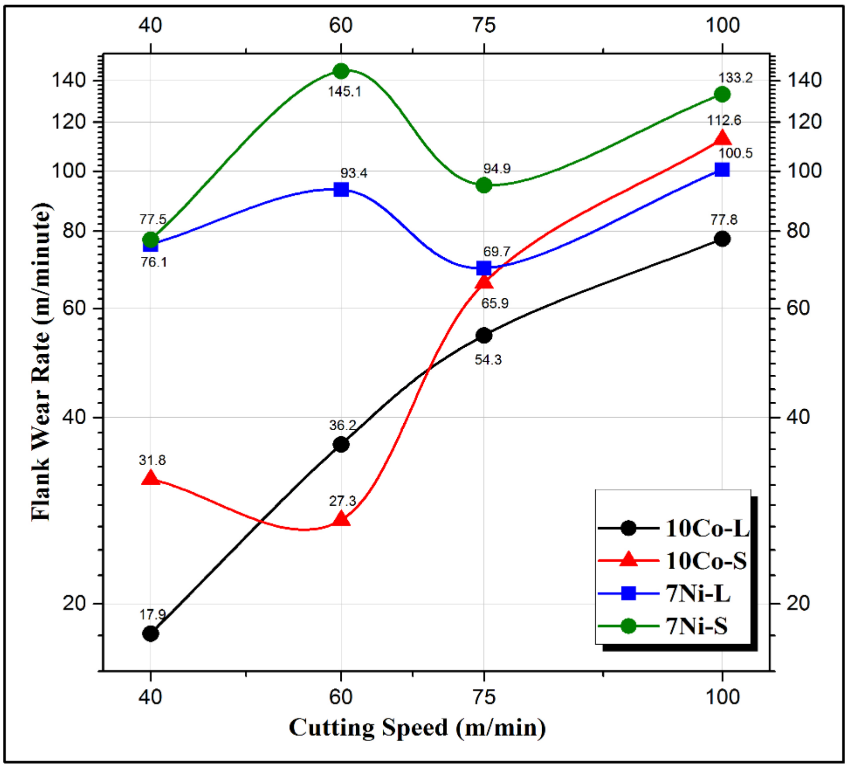

Figure 4.37: Variation in FWR for cutting tool inserts during dry milling of Ti-6Al-4V

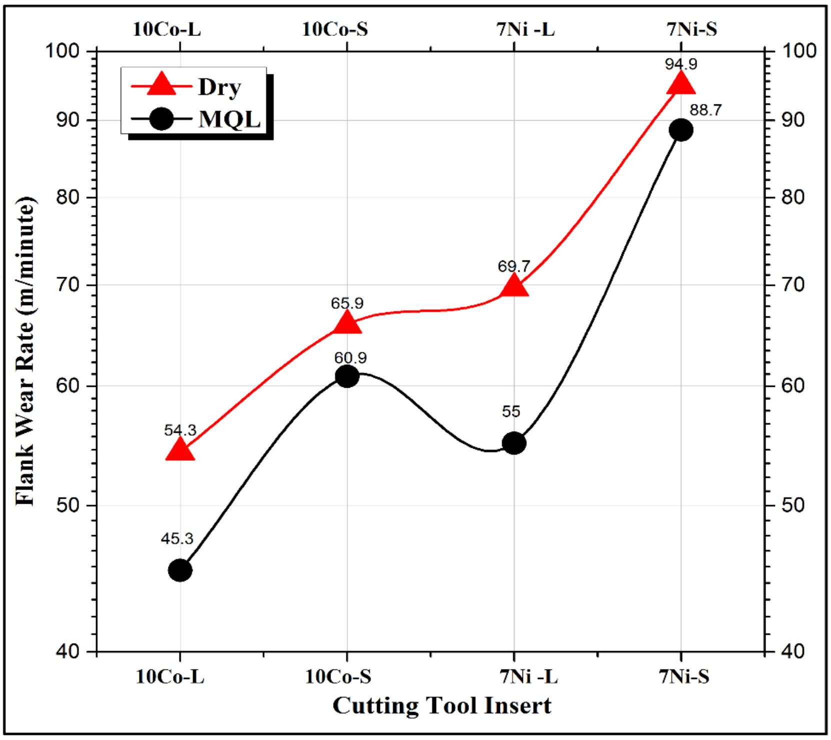

Figure 4.38: Variation in FWR for cutting tool inserts during Dry and MQL milling at a v_c of 75m/minute and an a_p of 0.5m

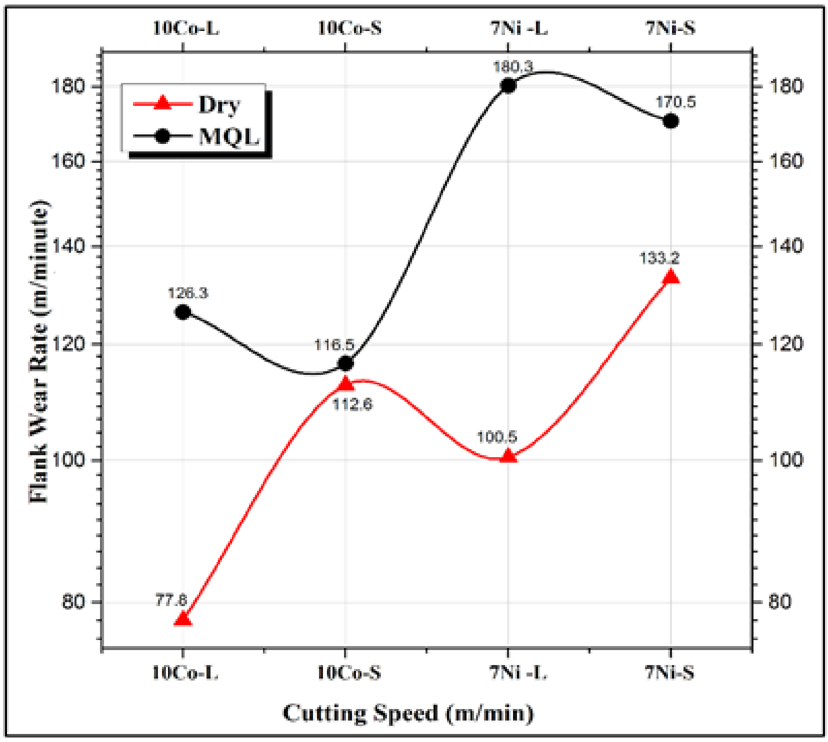

Figure 4.39: Variation in FWR for cutting tool inserts during Dry and MQL milling at a v_c of 100m/minute and an a_p of 0.5m

The FWR for the inserts were also observed to be lower during MQL milling at a v_c of 75m/minute than at 100m/minute (Figure 4.40). The lowest FWR for the 10Co-L, 10Co-S, and 7Ni-S inserts was during dry milling at a v_c of 40m/minute and an a_p of 1mm, while that of the 7Ni-L insert was during MQL milling at a v_c of 75m/minute and an a_p of 0.5mm (Figure 4.37).

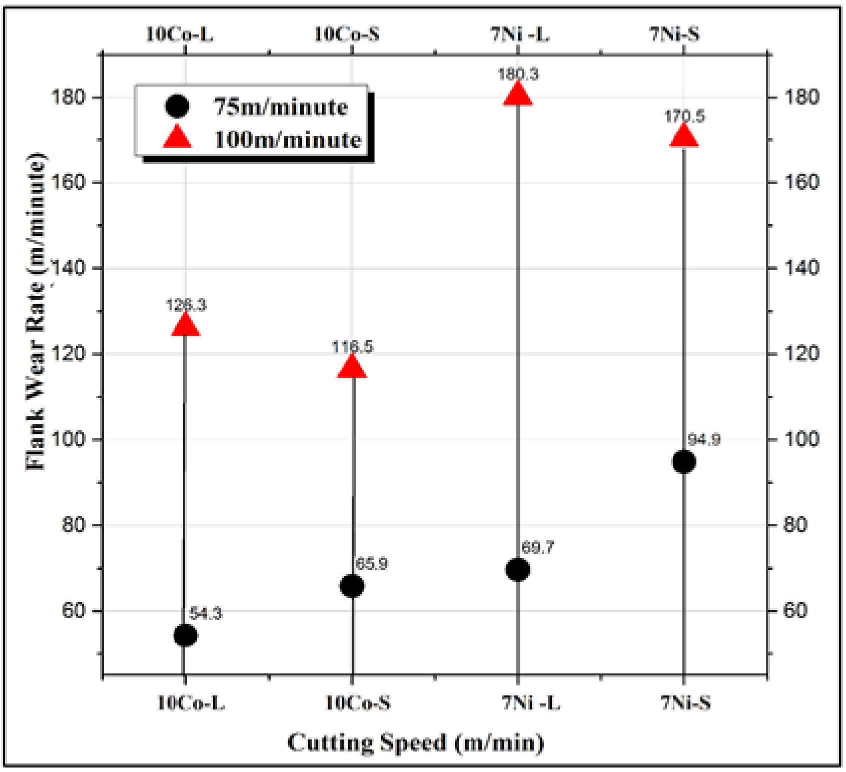

Figure 4.40: Variation in FWR for cutting tool inserts during MQL milling at a v_c of 75m/minute and 100m/minute

4.5 External Topography Analysis

The surface integrity results of the Ti-6Al-4V samples were suspected to be influenced by the selected milling parameters. Therefore, the surface roughness and residual stress data obtained from finishing milling runs are analyzed in this chapter, in order to compare, as well as attempt to find correlations between the milling parameters and surface integrity. Only selected micrographs for surface roughness are included in this section.

4.5.1 External Topography Analysis

The surface integrity results of the Ti-6Al-4V samples were suspected to be influenced by the selected milling parameters. Therefore, the surface roughness and residual stress data obtained from finishing milling runs are analyzed in this chapter, in order to compare, as well as attempt to find correlations between the milling parameters and surface integrity. Only selected micrographs for surface roughness are included in this section.

4.5.1.1 Analyses of surface roughness at a v_c of 75m/minute and an a_p of 0.5mm

The surface roughness (R_a) results for the Ti-6Al-4V samples after milling at a v_c of 75m/minute and an a_p of 0.5mm are shown in Table 4.22. It can be observed that the surface roughness for samples machined with LPS inserts was lower than those machined with SPS inserts (Figure 4.41). The sample machined with the 10Co-L insert had the lowest R_a of 0.4018 ± 0.03 μm, while the sample machined with the 7Ni-S insert had the highest R_a of 1.7338 ± 0.22μm (Figure 4.41).

Table 4.22: Surface roughness for Ti-6Al-4V samples after dry milling at a v_c of 75m/minute and an a_p of 0.5mm

Sample abbreviation	Milling Conditions		R_a [µm]	
	v_c [m/minute]	a_p [mm]	Profilometer	Confocal
10Co-L	75	0.5	0.4018 ± 0.03	1.430 ± 0.99
10Co-S	75	0.5	1.3338 ± 0.22	1.930 ± 0.59
7Ni-L	75	0.5	0.8750 ± 0.24	1.99 ± 0.54
7Ni-S	75	0.5	1.7338 ± 0.22	2.790 ± 0.03

R_a = 0.4018 ± 0.03µm R_a = 1.3338 ± 0.22µm R_a = 2.790 ± 0.03µm

Figure 4.41: Micrographs of the Ti-6Al-4V samples after dry milling at a v_c of 75m/minute and an a_p of 0.5mm with: (a) 10Co-L, (b) 10Co-S, and (c) 7Ni-S inserts.

4.5.1.2 Analyses of surface roughness at a v_c of 100m/minute and an a_p of 0.5mm

The R_a results after milling at a v_c of 100m/minute and an a_p of 0.5mm shows that the Ti-6Al-4V samples machined with LPS inserts had lower R_a than those machined with SPS inserts (Table 4.23).

Table 4.23: Surface roughness for Ti-6Al-4V samples after dry milling at a v_c of 100m/minute and an a_p of 0.5mm

Sample abbreviation	Milling Conditions		R_a [μm]	
	v_c [m/minute]	a_p [mm]	Profilometer	Confocal
10Co-L	75	0.5	0.4888 ± 0.14	1.817 ± 0.48
10C0-S	75	0.5	0.5670 ± 0.11	1.805 ± 0.12
7Ni-L	75	0.5	1.0380 ± 0.15	2.487 ± 0.4
7Ni-S	75	0.5	1.6728 ± 0.38	2.795 ± 0.46

The sample machined with the 10Co-L insert had the lowest R_a of 0.4888 ± 0.14 μm, while the sample machined with the 7Ni-S insert had the highest R_a of 1.6728 ± 0.38 μm (Figure 4.42).

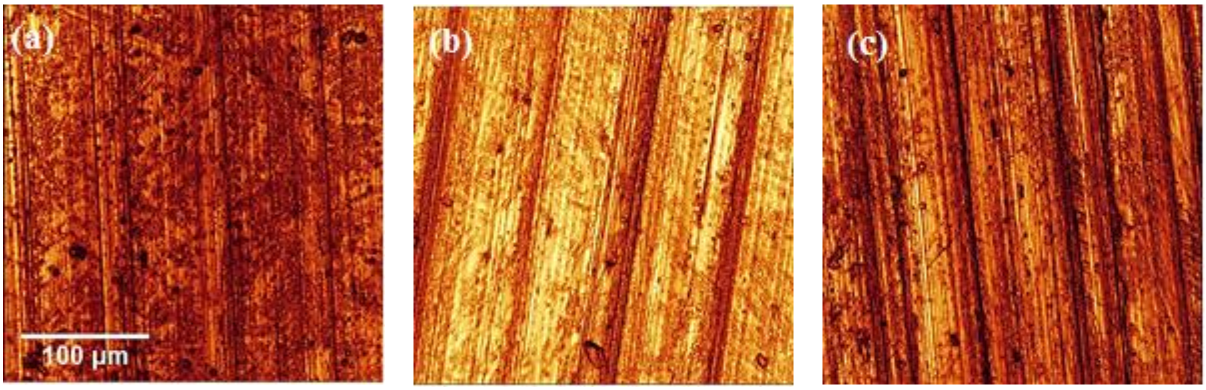

R_a = 0.4888 ± 0.134 μm R_a = 0.5670 ± 0.11μm R_a = 1.6728 ± 0.38 μm

Figure 4.42: 2D Micrographs of Ti-6Al-4V samples after dry milling at a v_c of 100m/minute and an a_p of 0.5mm with: (a) 10Co-L, (b) 10Co-S (c) 7Ni-S inserts

4.5.1.3 Effect of MQL on R_a at v_c of 75m/min and an a_p of 0.5mm

The R_a values after MQL milling at a v_c of 75m/minute and an of a_p 0.5mm shows that the samples machined with LPS inserts had lower R_a than those machined with SPS inserts (Table 4.24 and Figure 4.43). The sample machined with the 10Co-L insert had the lowest R_a of 0.2857 ± 0.05 µm, while the sample machined with the 7Ni-S insert had the highest R_a of 1.565 ± 0.33 µm (Figure 4.43).

Table 4.24: Surface roughness for Ti-6Al-4V samples after MQL milling at a v_c of 75m/minute and an a_p of 0.5mm

Sample abbreviation	Milling Conditions		R_a [µm]	
	v_c [m/minute]	a_p [mm]	Profilometer	Confocal
10Co-L	75	0.5	0.2857 ± 0.05	1.20 ± 0.19
10C0-S	75	0.5	0.6628 ± 0.12	1.740 ± 0.23
7Ni-L	75	0.5	0.7743 ± 0.23	1.930 ± 0.07
7Ni-S	75	0.5	1.565 ± 0.33	1.940 ± 0.04

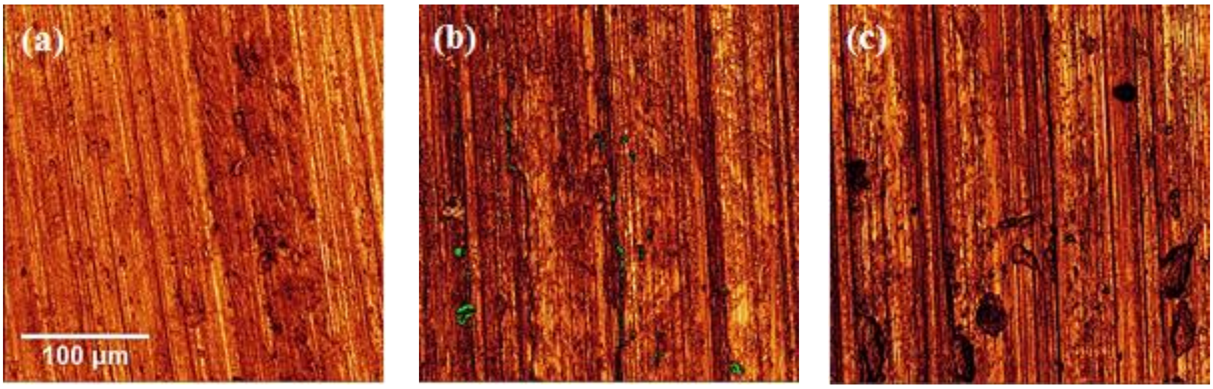

R_a = 0.2857 ± 0.05µm R_a = 0.6628 ± 0.12µm R_a = 0.7743 ± 0.23µm

Figure 4.43: 2D Micrographs of Ti-6Al-4V samples after MQL milling at a v_c of 75m/minute and an a_p of 0.5mm with: (a) 10Co-L, (b) 10Co-S (c) 7Ni-S inserts

4.5.1.4 Effect of MQL on R_a at a v_c of 100m/min and an a_p of 0.5mm

The R_a results for the Ti-6Al-4V samples after MQL milling at a v_c of 100m/minute and an a_p of 0.5mm is shown in Table 4.25. It can be observed that the samples machined with SPS inserts had lower R_a than those machined with LPS inserts (Figure 4.44). The sample machined with the 10C0-S insert had the lowest R_a of 1.046 ± 0.236µm, while that machined with the 7Ni-L insert had the highest R_a of 1.610 ± 0.014µm (Figure 4.44).

Table 4.25: Surface roughness for Ti-6Al-4V samples after MQL milling at a v_c of 100m/minute and an a_p of 0.5mm

Sample abbreviation	Milling Conditions		R_a [µm]	
	v_c [m/minute]	a_p [mm]	Profilometer	Confocal
10Co-L	75	0.5	0.8470 ± 0.11	1.315 ± 0.318
10C0-S	75	0.5	0.4590 ± 0.08	1.046 ± 0.236
7Ni-L	75	0.5	0.7980 ± 0.06	1.610 ± 0.014
7Ni-S	75	0.5	0.7820 ± 0.07	1.30 ± 0.042

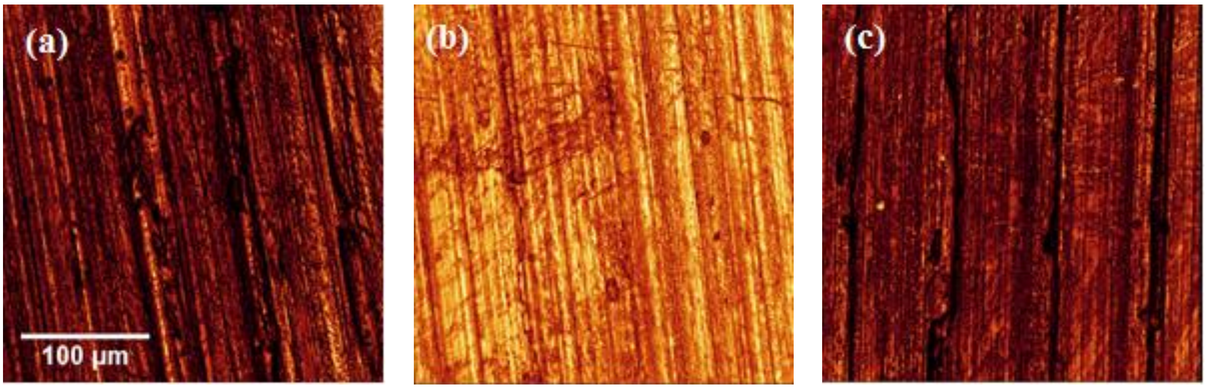

R_a = 0.8470 ± 0.11µm R_a = 0.4590 ± 0.08µm R_a = 0.7980 ± 0.06µm

Figure 4.44: 2D Micrographs of Ti-6Al-4V samples after MQL milling at a v_c of 100m/minute and ana_p of 0.5mm with: (a) 10Co-L, (b) 10Co-S (c) 7Ni-S inserts

4.5.1.5 Overall Trends

The following trends were established form the surface roughness results of the Ti-6Al-4V samples: during dry machining, it was observed that at an a_p of 0.5mm the surface roughness for samples machined with LPS inserts increased with increase in cutting speed while those machined with SPS inserts decreased with increase in cutting speed as shown in Figure 4.45. It was also observed that during MQL milling, the R_a for samples machined with LPS inserts increased with increase in cutting speed, while the R_a for samples machined with SPS inserts decreased with increase in cutting speed as shown in Figure 4.46.

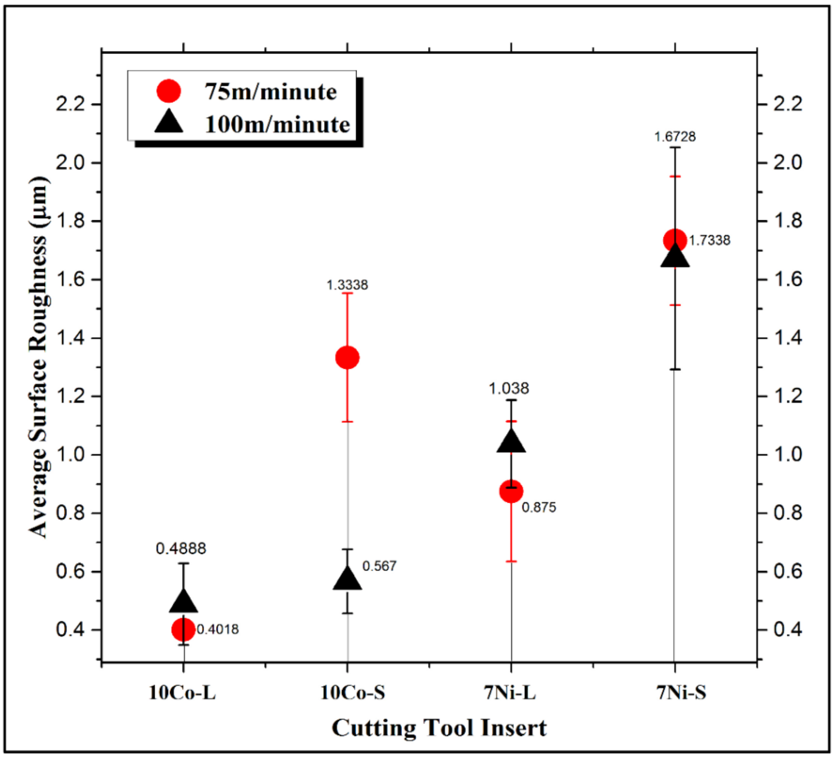

Figure 4.45: Variation in surface roughness of Ti-6Al-4V samples during dry milling at 75m/minute and 100m/minute

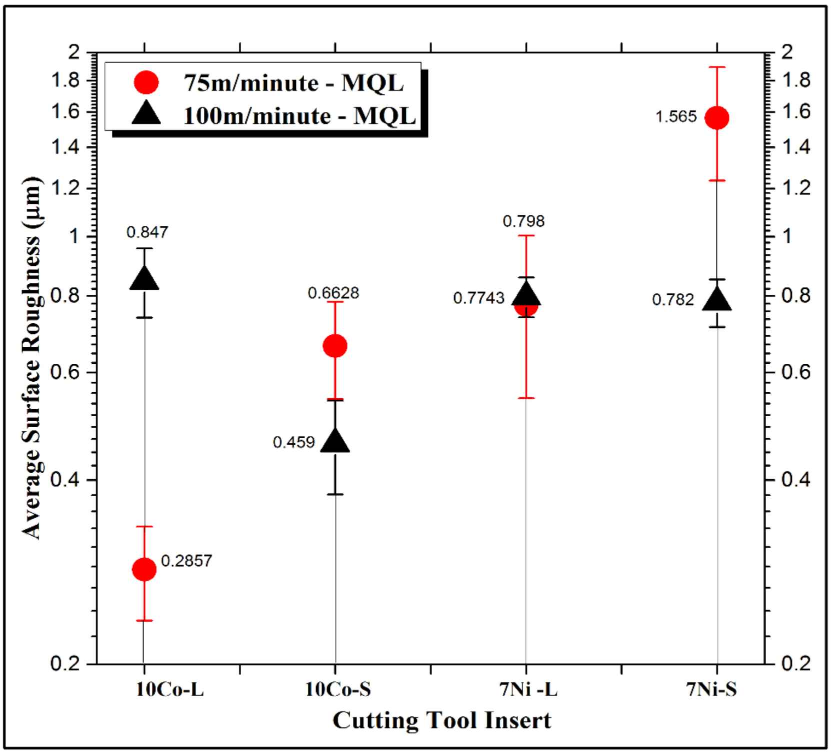

Figure 4.46: Variation in surface roughness of Ti-6Al-4V samples during MQL milling at 75m/minute and 100m/minute

The samples machined under MQL conditions had lower surface roughness than those machined dry at a v_c of 75m/minute and 100m/min (Figure 4.47 and Figure 4.48). The 10Co-L insert was however an exception to this trend at a v_c of 100m/min and an a_p of 0.5mm (Figure 4.48).

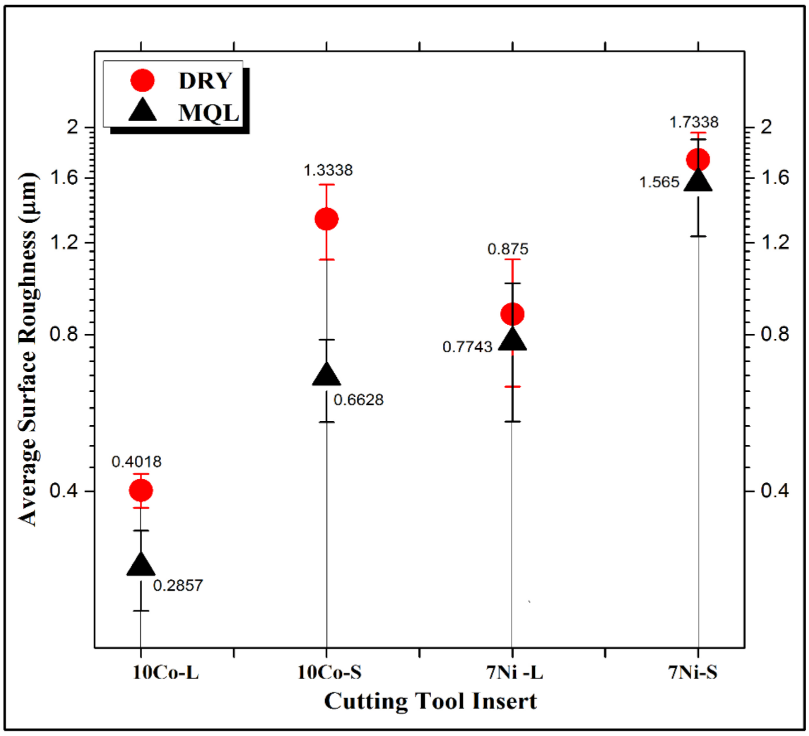

Figure 4.47: Variation in surface roughness of Ti-6Al-4V samples during dry and MQL milling at a v_c of 75m/minute and an of a_p 0.5mm

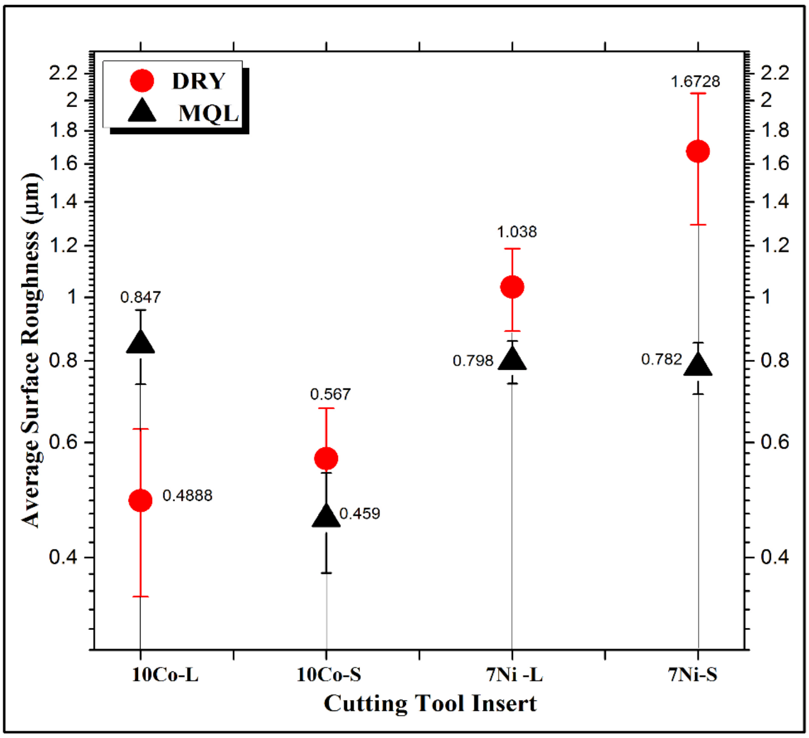

Figure 4.48: Variation in surface roughness of Ti-6Al-4V samples during dry and MQL milling at a v_c of 100m/minute and an of a_p 0.5mm

The Ti-6Al-4V sample machined with the 10Co-L insert under MQL conditions at a v_c of 75m/min and an a_p of 0.5mm had the lowest surface roughness of 0.2857 ± 0.05 μm for profilometry measurement and 1.20 ± 0.19μm for confocal microscopy measurements (Figure 4.45 and Figure 4.49). On the other hand the Ti-6Al-4V sample machined with the 7Ni-L insert under dry milling condition at a v_c of 75m/minute an a_p of 0.5mm had the highest surface roughness of 1.7338 ± 0.22 μm for profilometry measurement and 2.790 ± 0.03 μm for confocal microscopy measurements (Figure 4.46 and Figure 4.50).

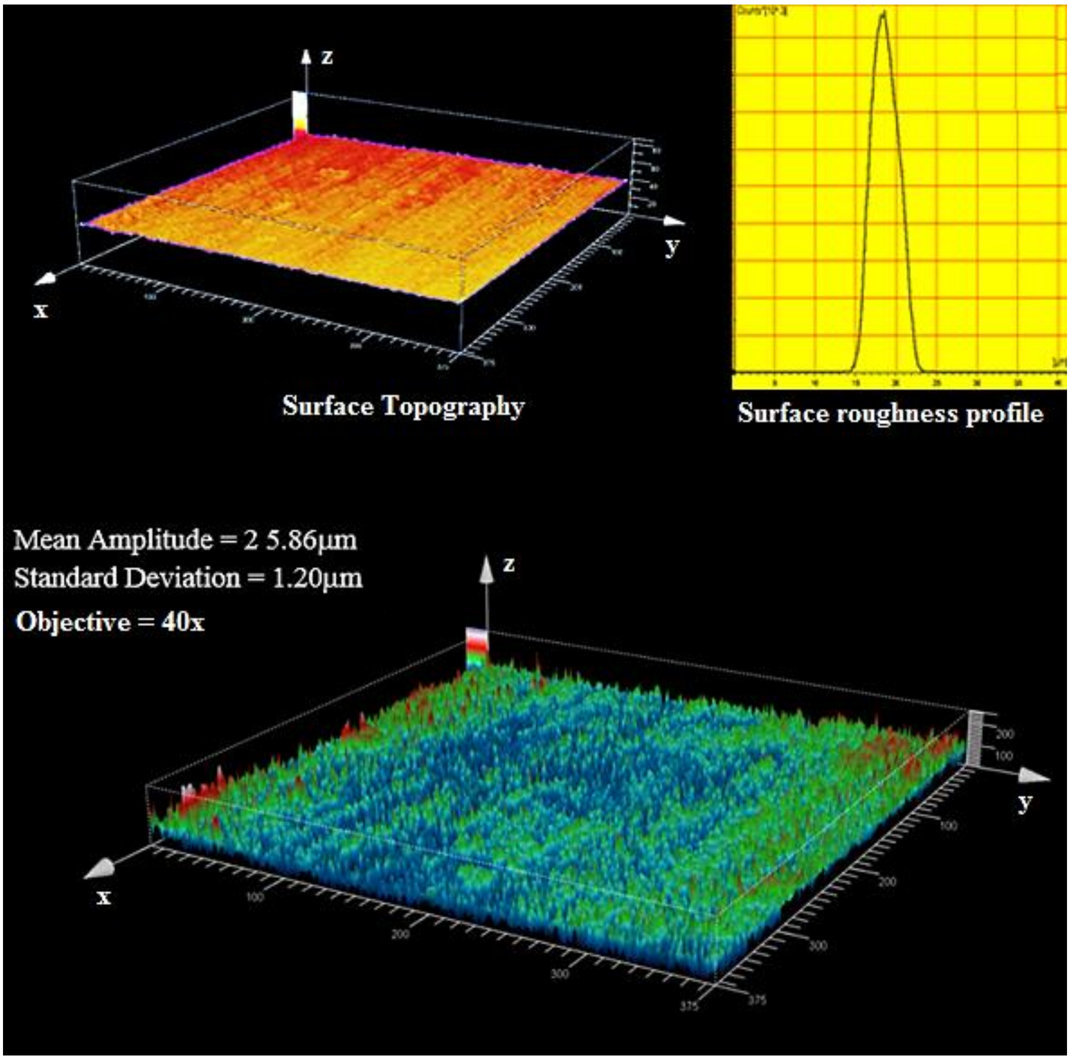

Figure 4.49: Laser confocal 3D topographical maps and surface deviation profile for the Ti-6Al-4V sample machined with the 10Co-L insert under MQL condition at a v_c of 75m/minute and a_p of 0.5mm

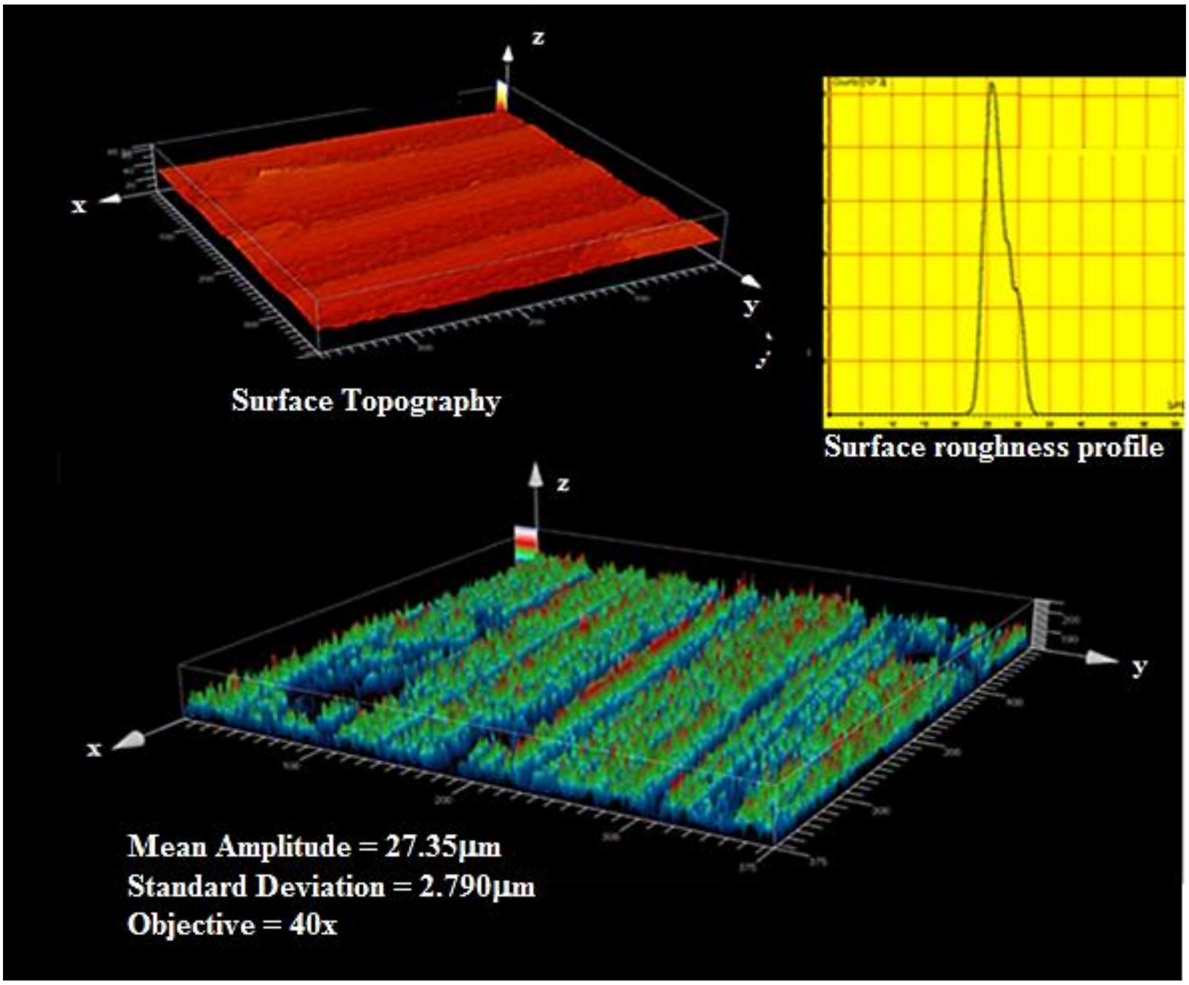

Figure 4.50: Laser confocal 3D topographical maps and surface deviation profile for the Ti-6Al-4V sample machined with the 7Ni-S insert under dry milling condition at 75m/minute using 7Ni-S cutting tool insert

4.5.2 Subsurface Layer Analyses

In order to analyze the effect of milling parameters on the subsurface layer of the Ti-6Al-4V samples during finishing, residual stress measurements were carried out on selected Ti-6Al-4V samples. Only preliminary data of residual stress measurements are included in this section. This is because some issues were encountered with the XRD detector. Nevertheless, further results will be available for a further part of this activity.

Six points were measured in the 10Co-L, 7Ni-L and 7Ni-S samples machined under dry condition at a v_c of 75m/minute and a_p of 0.5mm. The measurements were in the longitudinal (90 degrees) and transverse (0 degrees) directions (Table 4.26) (Figure 4.51, 4.53 and 4.53). The results were showing mostly surface induced residual stresses in compression, but there were still some uncertainties about the obtained peak, with no clear positioning as titanium alpha or beta phase induced. I still await further clarification from the XRD producer, Stress Tech, and Coventry University.

Table 4.26: Preliminary residual stress results for some Ti-6Al-4V samples machined at a v_c of 75m/minute and a_p of 0.5mm

Samples	Measurement N.	Points	σ0 [MPa]	Error [MPa]	σ90 [MPa]	Error [MPa]	Sample
10Co-L – Dry	1	1	8.7	32.3	-154.8	16.1	1-1
	2	1	-2.8.4	18.5	-162.8	24	1-1
	2	1	-2.6.4	28.5	-162.7	15.9	1-1
	4	2	64.8	27.9	31.9	9.6	1-2
	5	2	53.8	8.8	39.4	34.1	1-2
	6	2	99.1	28.9	24	32.5	1-2
7Ni-L – Dry	7	1	-14.6	18.2	-90.2	24.7	2-1
	8	1	-21.2	15.9	-139.3	18.1	2-1
	9	1	12.4	24.4	-113.1	15.9	2-1
	10	2	77.6	13.4	-60.2	20.1	2-2
	11	2	40.5	16.8	-11.5	11.8	2-2
	12	2	29.3	11.2	-50.8	18.5	2-2
10Co-S – Dry	13	1	-6.4	26	-161.1	11.5	3-1
	14	1	-12.3	18.8	-103.6	21.6	3-1
	15	1	-2.1	26.1	-167.5	14	3-1
	16	2	85.8	11.2	0.3	16.5	3-2
	17	2	97.5	27.6	7	23.5	3-2
	18	2	83	13	-36.6	15	3-2

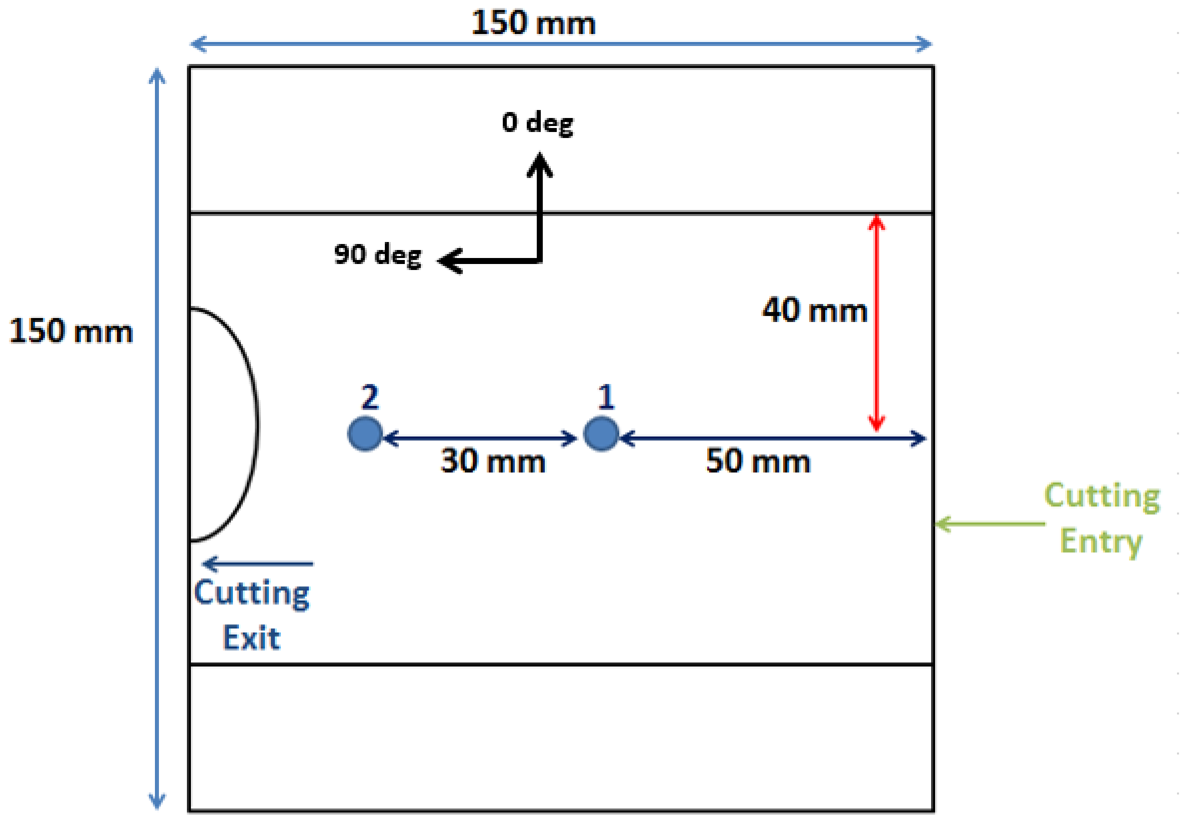

Figure 4.51: Schematic diagram of workpiece indicating points where residual stresses were measured

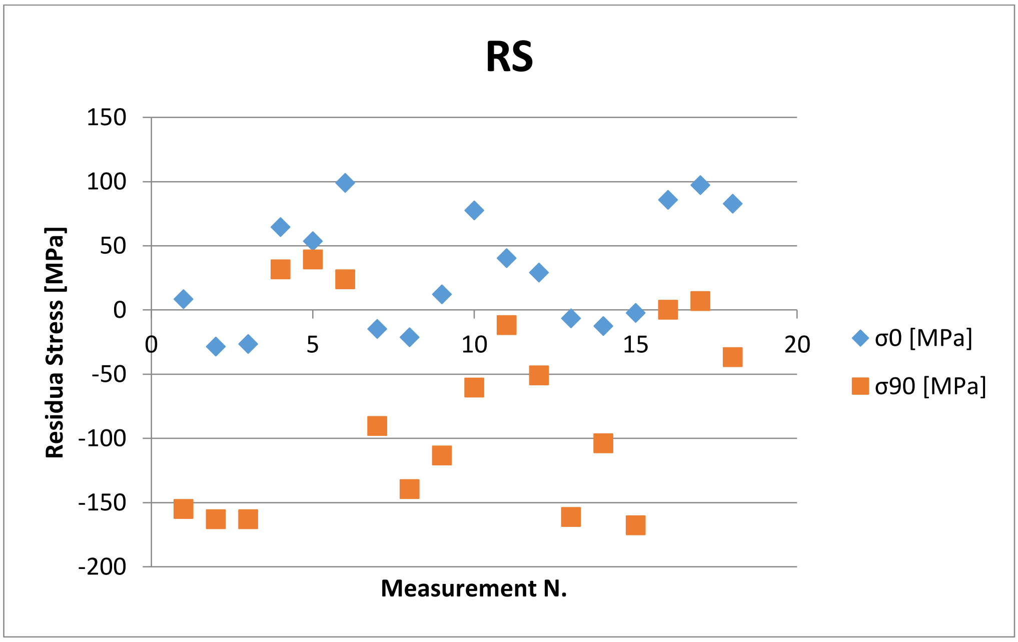

Figure 4.52: Graphical representation of residual stress measurements for Ti-6Al-4V sample machined with 10Co-L insert at a v_c of 75m/minute and a_p of 0.5mm

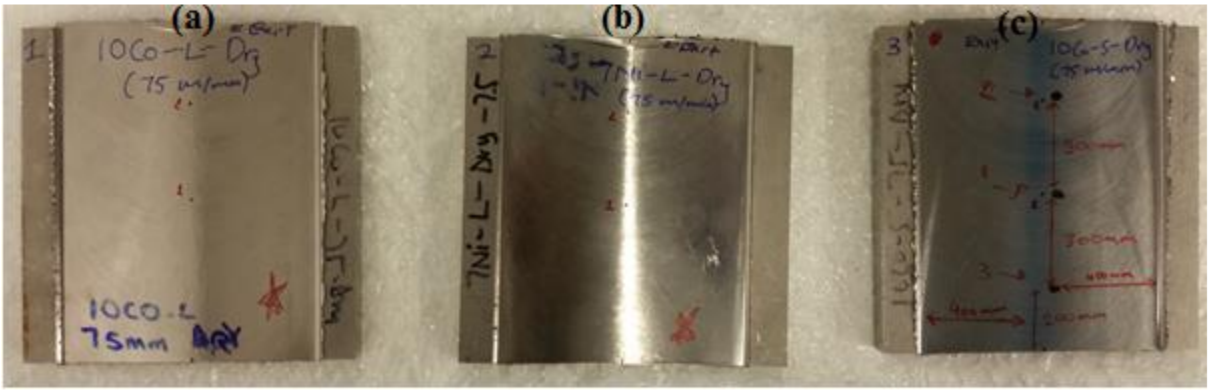

Figure 4.53: Ti-6Al-4V samples used for preliminary residual stress measurements: (a) samples machined with 10Co-L insert, (b) sample machined with 7Ni-L insert, (c) samples machined with 10Co-L insert at a v_c of 75m/minute and a_p of 0.5mm

Chapter 5 : Discussion

This chapter discusses the results obtained from the analyses of distinct performance characteristics in an attempt to establish correlations.

5.1 Analyses of milling at a v_c of 40m/minute and an a_p of 1mm

At a v_c of 40m/minute and an a_p of 1mm, no consistent trend could be established between the milling temperatures, resultant forces, and hardness of the cutting tool inserts. However, it was observed that the FWR experienced by the cutting tool inserts increased with respect to their K_{IC} (Figure 5.1). The only exception to this trend was the 11Ni-L insert (Figure 5.1). The 10Co-L and 10Co-S inserts which had higher K_{IC} experienced lower FWR of 17.9 m/minute and 13.8m/minute, while the N-12Co-L and N-12Co-S inserts which had lower K_{IC} experienced catastrophic failure (Figure 5.1). This confirms that high a K_{IC} is required for thermal and impact resistance (Figure 5.1) [2014Gen].

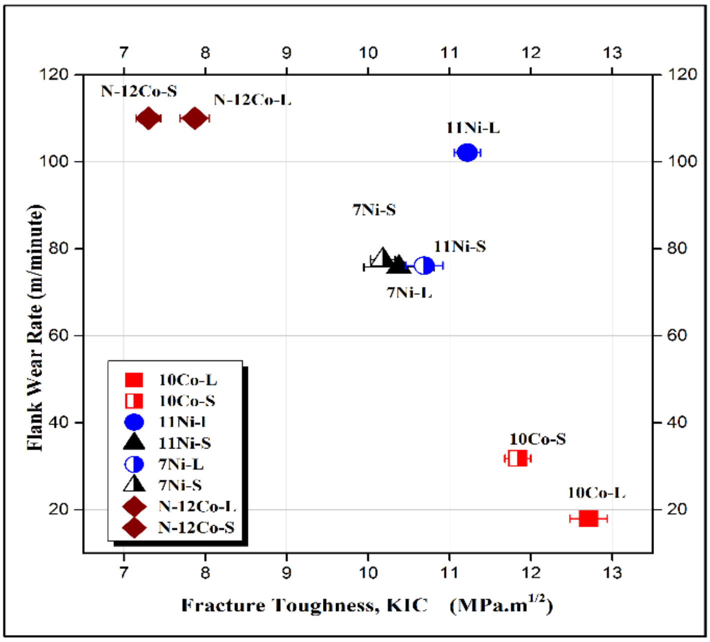

Figure 5.1: Relationship between flank wear rate of cutting tool inserts and fracture toughness and at a v_c of 40m/minute and an a_p of 1mm

5.2 Analyses of milling at a v_c of 60m/minute and an a_p of 1mm

At a v_c of 60m/minute and an a_p of 1mm, the resultant forces experienced by the cutting tool inserts decreased with increase in their K_{IC} (Figure 5.2[a]). The only exception to this trend was the 7Ni-L insert (Figure 5.2[a]). The 10Co-L insert which had the highest K_{IC} experienced the lowest resultant force (Figure 5.2[a]). The milling temperature increased with increase in resultant forces (Figure 5.2[b]). The only exceptions to this trend was the 7Ni-L and 7Ni-S inserts (Figure 5.2[b]). This was because of to their poor K_{IC} (Figure 4.2) [2014Gen]. The resultant forces experienced by the inserts was also observed to be increasing with increase in FWR (Figure 5.2[c]). This was because flank wear destroys the sharp insert cutting edge required for machining, resulting in more cutting forces being required for machining [2008Tha].

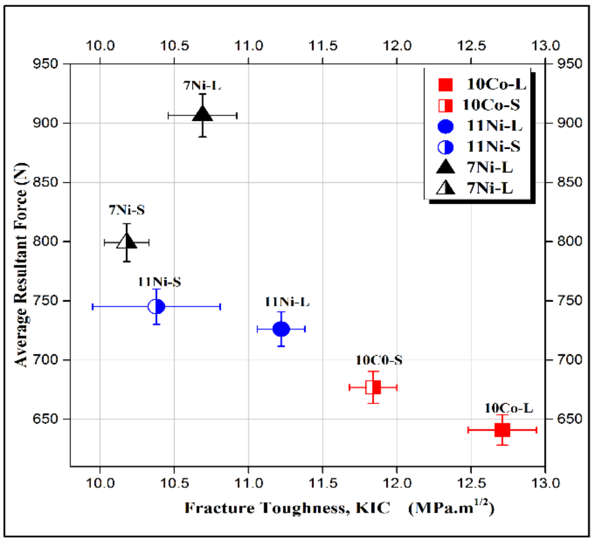

(a)

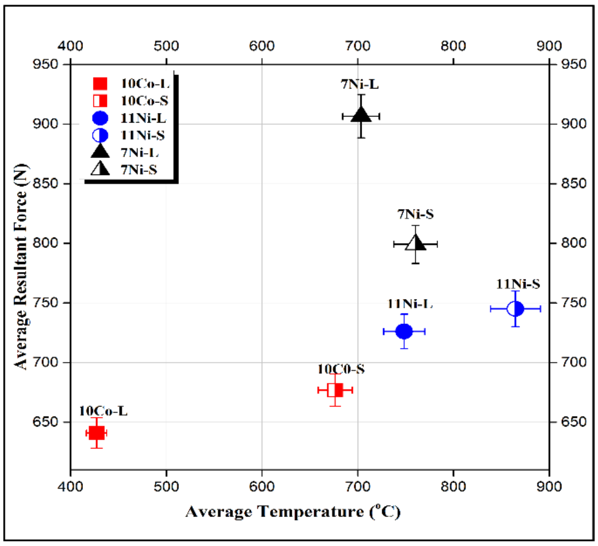

(b)

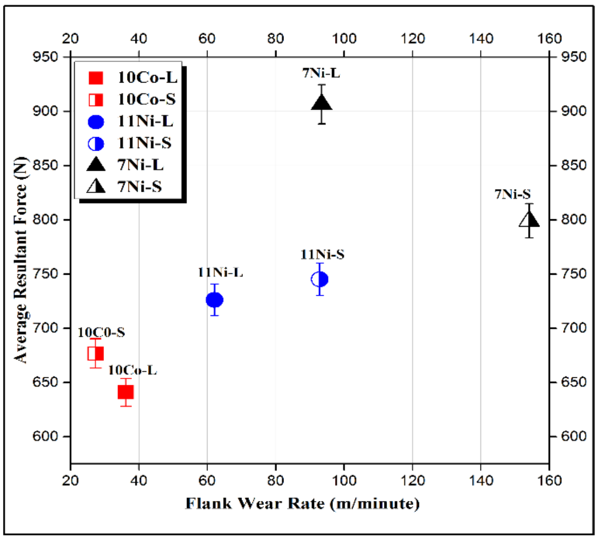

(c)

Figure 5.2: Relationship between :(a) Average resultant force and fracture toughness of cutting tool inserts, (b) Average resultant force and average temperature, (c) Average resultant forces and flank wear rate of cutting tool inserts at a v_c of 60m/minute and an a_p of 1mm

5.3 Analyses of milling at a v_c of 75m/minute and an a_p of 0.5mm

The lower temperatures experienced by the 10Co-L and 10Co-S inserts at a v_c of 75m/minute and an a_p of 0.5mm was due to their higher K_{IC} (Figure 5.3a) [2014Gen]. The LPS inserts which had higher K_{IC} owing to high binder amount and good wetting of WC by Co experienced lower temperatures, while the SPS inserts which had lower K_{IC} due to the retained stress from rapid cooling experienced higher temperatures (Figure 5.3a) [2014Gen]. The 10Co-L insert which had the highest K_{IC} experienced the lowest temperature of 237.8 ± 6.5 °C (Figure 5.3a). The lower cutting forces experienced by the 7Ni-L and 7Ni-S inserts could be owing to the higher milling temperature which thermally deformed the Ti-6Al-4V samples, thus making it easier to machine (Figure 5.3b) [1985Asm]. Nevertheless, the lower fracture toughness and higher milling temperature experienced by the 7Ni-L and 7Ni-S inserts resulted in higher FWR (Figure 5.3a, Figure 5.3b and Figure 5.3c) [2013Gen]. This was because the high temperature experienced during milling with the 7Ni-L and 7Ni-S inserts thermally softened their cutting edges resulting in accelerated FWR [2008Tha] (Figure

5.3a and Figure 5.3b). It could also be observed that the high temperature generated during milling with the 7Ni-L and 7Ni-S inserts were concentrated on the cutting tool edge, resulting in accelerated FWR (Figure 5.3b and Figure 5.3c). This is owing to the poor thermal conductivity of Ti-6Al4V [1989Mac].

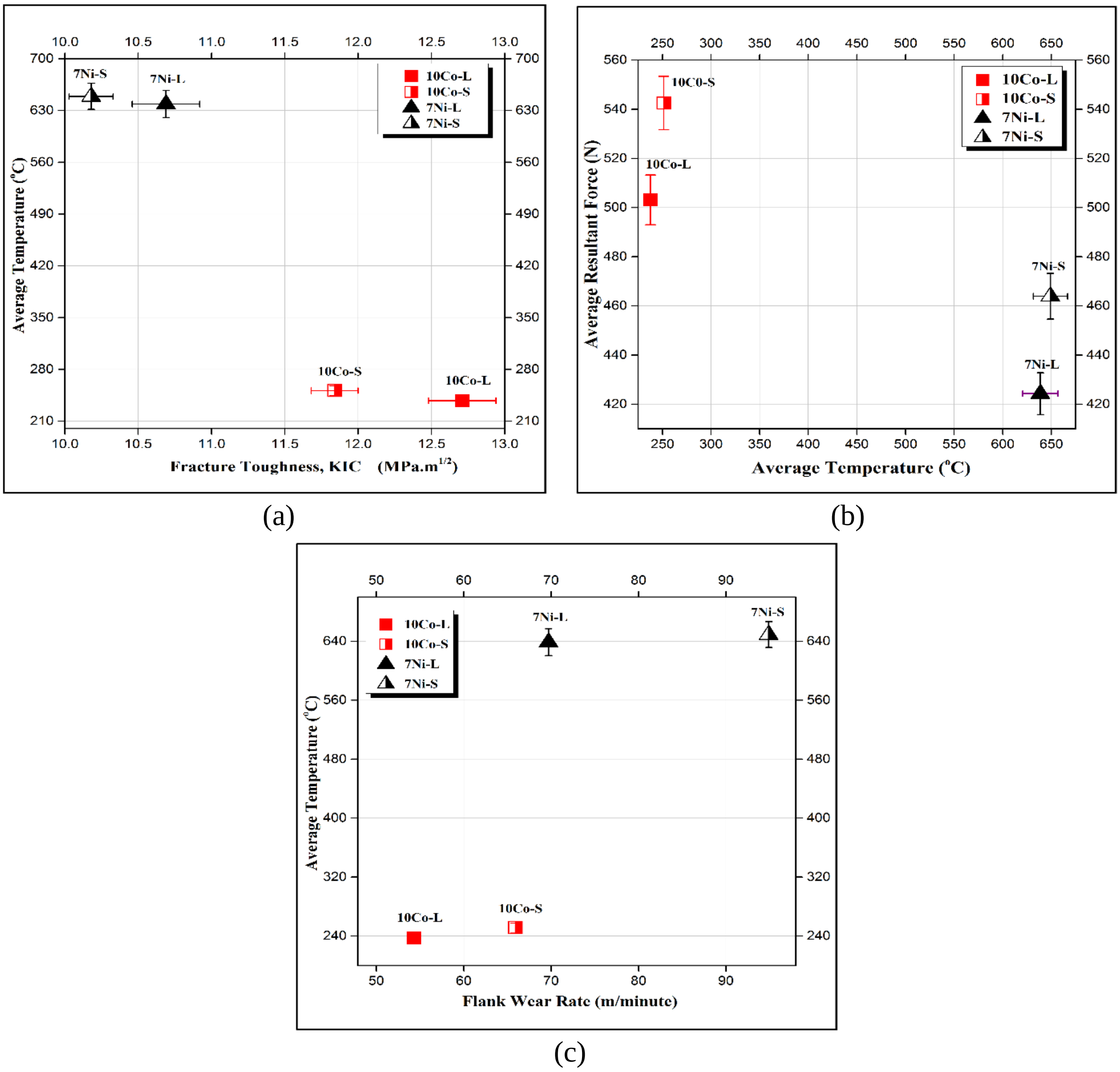

Figure 5.3: Relationship between :(a) Average temperature and fracture toughness of cutting tool inserts, (b) Average resultant forces and average temperature, (c) Average temperature and flank wear rate of cutting tool inserts at a v_c of 75m/minute and an a_p of 0.5mm

5.4 Analyses of milling at a v_c of 100m/minute and an a_p of 0.5mm

At a v_c of 100m/minute and an a_p of 0.5mm, the cutting tool inserts with higher K_{IC} experienced lower resultant forces than those with lower K_{IC} (Figure 5.4a) [2014Gen]. The 10Co-L insert which had the highest K_{IC} of 12.71 ± 0.23 MPa.m$^{1/2}$ experienced the lowest resultant force of 301.9 ± 6.1N (Figure 5.4a). The milling temperature increased with increase in resultant force (Figure 8.4b). This could be owing to poor thermal conductivity of Ti-6Al-4V (6.7 W/m-K) [1989Mac]. The LPS inserts which experienced lower resultant forces during milling experienced lower milling temperatures (Figure 5.4b). The FWR of the cutting tool inserts was also increased with increase in milling temperature and resultant forces (Figure 5.4b and Figure 5.4c). The FWR of the LPS inserts was lower than that of the SPS inserts because of the lower resultant forces and temperatures experienced during milling (Figure 5.4b and Figure 8.4c). The better surface finish produced by the LPS inserts was because of their high K_{IC}, as well as their lower temperature and resultant forces (Figure 4.42 Figure 5.4d) [2014Gen].

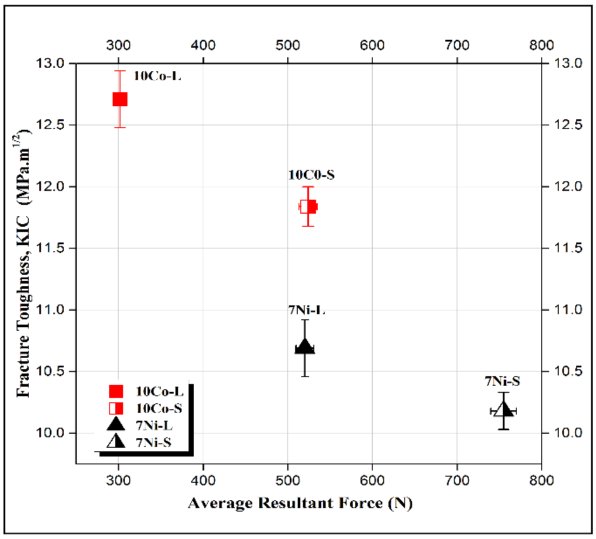

(a)

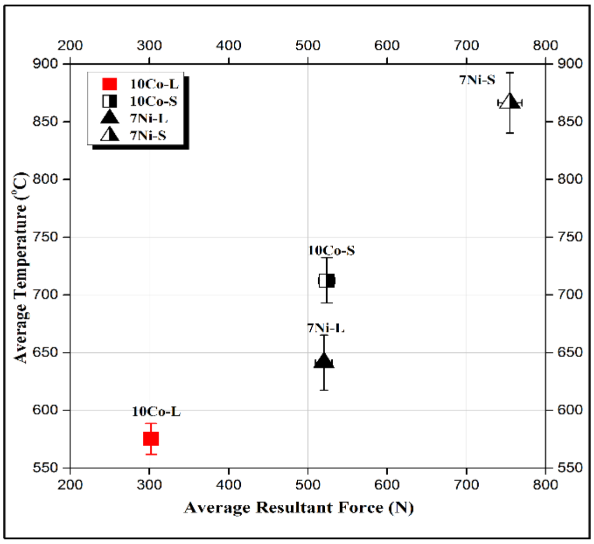

(b)

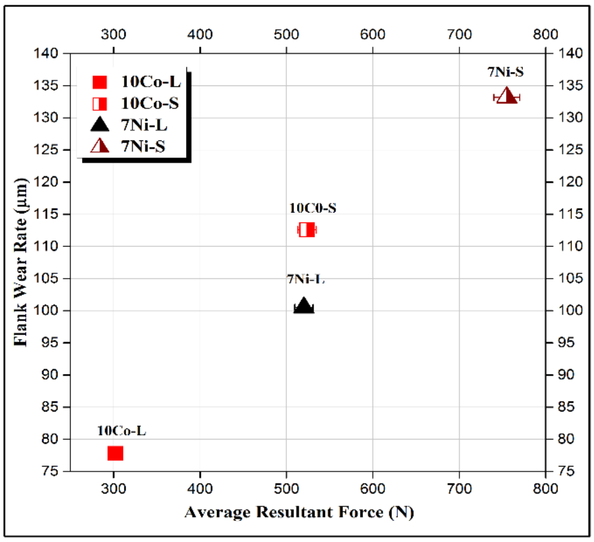

(c)

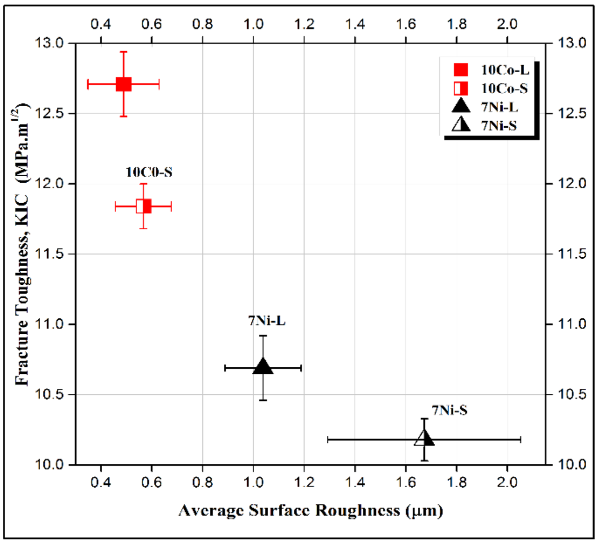

(d)

Figure 5.4: Relationship between :(a) Fracture toughness of cutting tool inserts and average resultant forces and, (b) Average temperature and average resultant forces, (c) Flank wear rate of cutting tool inserts and average resultant forces (d) Fracture toughness of cutting tool inserts and average surface roughness at a v_c of 100m/minute and an a_p of 0.5mm

5.5 Analyses of MQL milling at a v_c of 75m/minute and an a_p of 1mm

The analyses of results for MQL milling at a v_c of 75m/minute and an a_p of 0.5mm shows no consistent trend between the mechanical properties of the cutting tool inserts and the cutting temperature/resultant forces experienced during milling. However, It could be observed that the except for the 7Ni-S insert, the resultant forces experienced by the cutting tool inserts increased with respect to their FWR (Figure 5.5a) [2008Tha]. The results also shows that the inserts with lower FWR produced better surface integrity than those with higher FWR (Figure 5.5b). The better surface integrity for samples machined with the 10Co-L and 7Ni-L inserts could be due to their sintering technique (Figure 5.5b).

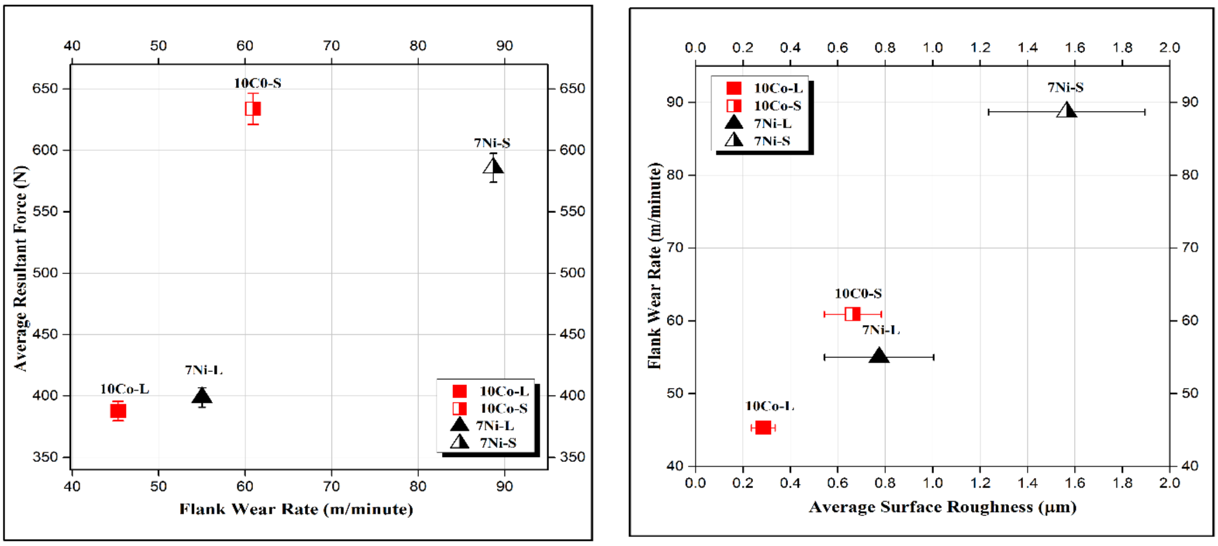

(a) (b)

Figure 5.5: Relationship between :(a) Average resultant forces with flank wear rate of cutting tool inserts (b) Flank wear rate of cutting tool inserts and average surface roughness at a v_c of 75m/minute and an a_p of 0.5mm

5.6 Analyses of MQL milling at a v_c of 100m/minute and an a_p of 0.5mm

The analyses of results for MQL milling at a v_c of 100m/minute and an a_p of 0.5mm shows that the hardness of the cutting tool inserts was an important criteria for machining at higher cutting speeds [2011Lop]. The high hardness of the 7Ni-L and 7Ni-S cutting tool inserts at elevated temperature owing to their finer WC grains made them more resistant to milling forces which resulted in their ability to produce a better surface finish of the Ti-6Al-4V samples (Figure 5.6a and Figure 5.6b) [1989Mac, 2014Gen]. Nevertheless, the poor K_{IC} of the 7Ni-L and 7Ni-S inserts owing to their sintering technique (Figure 5.6b).

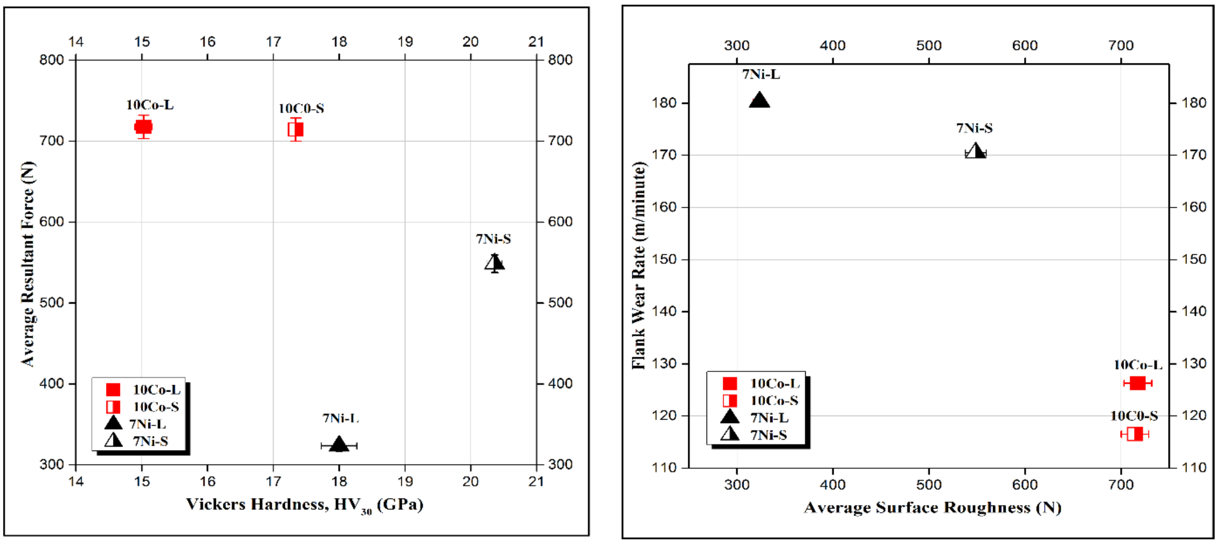

(a) (b)

Figure 5.6: Relationship between :(a) Average resultant forces and Vickers hardness of cutting tool inserts, (b) Flank wear rate and average surface roughness at a v_c of 100m/minute and an a_p of 0.5mm

5.7 Overall Analyses

The following correlations were established between distinct performance characteristics during dry finishing runs: Inserts with higher K_{IC} experienced either lower resultant forces compared to those with lower K_{IC} (Figure 5.2a, and 5.4a). This trend however changed during MQL runs at 100m/min, as inserts with higher HV30 experienced lower resultant forces compared to those with lower HV_{30} (Figure 5.6a). The FWR experienced by the cutting tool inserts was mostly dependent on the resultant forces, except during dry machining at 100m/minute where the high milling temperature played a role in the FWR of the cutting tool inserts (Figure 5.2c, 5.4c, and 5.3c). The surface roughness of the Ti-6Al-4V samples increased with increase in the flank wear rate of the cutting tool inserts (Figure 5.7). The sample machined with the 10Co-L insert which experienced the lowest FWR of 54.3µm at a v_c of 75m/minute and an a_p of 0.5mm had a better surface finish compared to other samples (Figure 5.7).

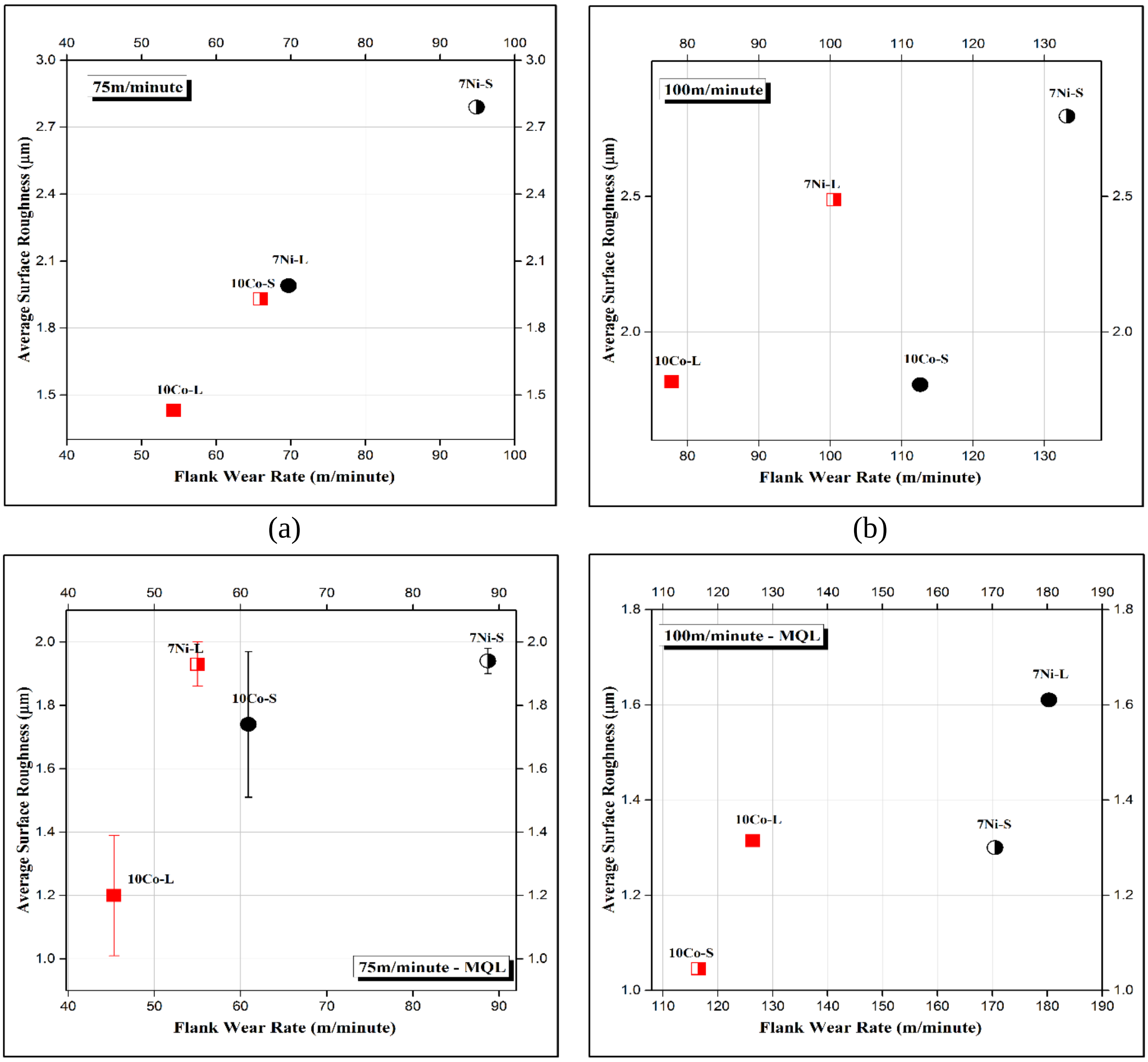

(c) (d)

Figure 5.7: Variation in surface roughness of machined Ti-6Al-4V samples with flank wear of cutting tool inserts at: (a) Dry machining at a v_c of 75m/minute and an a_p of 0.5mm, (b) Dry machining at a v_c of 100m/minute and an a_p of 0.5mm, (c) MQL machining at a v_c of 75m/minute and an a_p of 0.5mm, and (d) MQL machining at a v_c of 100m/minute and an a_p of 0.5mm.

Chapter 6 : Conclusion and Recommendations

6.1 Conclusion

In accordance to existing literatures on Ti-6Al-4V machining, the tungsten carbide inserts performed better than the polycrystalline diamond tool in Ti-6Al-V machining. In this work a step was further taken to compare the tungsten carbide insert with other promising classes of cemented carbide inserts, some having better mechanical properties than the tungsten carbide. Liquid phase sintering and spark plasma sintering techniques were used for producing the inserts in a bid to improve upon the mechanical properties. Similar to other Ti-6Al-4V researches the tungsten carbide inserts (10Co-L and 10Co-S) still performed better than the other classes of cemented carbides inserts (7Ni-L, 7Ni-S, 11Ni-L, 11Ni-S, N-12Co-L and N-12Co-S). The tungsten carbide inserts had better resistance to cutting forces, temperatures, FWR, as well as produced an optimum surface finish in both dry and MQL milling. Nevertheless, further research is recommended for the 7Ni-L and 7Ni-S inserts which showed promising results at a higher v_c of 100m/minute and an a_p of 1mm.

The LPS inserts generally performed better than the SPS inserts. This was due to their better mechanical properties (higher fracture toughness and transverse rupture strength) required for face milling of Ti-6Al-4V. The application of MQL generally reduced milling temperatures and forces resulting in an optimized surface finish. The cutting speed played a major role in achieving optimum surface integrity followed by the depth of cut. In this study optimum surface integrity was achieved at a v_c of 75m/minute and a lower a_p of 0.5mm.

It was however difficult to correlate this study with existing literatures, as little or no research had been conducted in the area of machining of Ti-6Al-4V with innovative carbide tools.

6.2 Recommendation

- Further investigations should be carried out towards optimizing the surface integrity during Ti-6Al-4V at higher cutting speeds and much lower depth of cuts.
- The effect of flood cooling in Ti-6Al-4V machining should be investigated, as this might result in a better surface integrity.
- Dry machining condition is not suitable for machining Ti-6Al-4V due to the high FWR and poor surface integrity, especially at high cutting speeds.
- Further investigations should be carried out towards increasing the fracture toughness of the 7Ni-L and 7Ni-S inserts which showed promising results at a v_c of 100m/minute and an a_p of 1mm.
- Further investigations should be carried out on the chips collected during machining, as this could provide additional information on the machining process, tool wear and machined surface quality.

References

[1953Coo] N. Cook, Proceeding of Son Machining and Grinding of Titanium, Watertown, Arsenal. (1973), pp. 1-7.

[1963Gur] J. Gurland, The Fracture Strength of Sintered Tungsten Carbide–Cobalt Alloys in Relation to Composition and Particle Spacing, Trans. Metall. Soc., 227 (1963), pp. 1146–1150.

[1964Fie] M. Fied and J. Kahles. The Surface Integrity of Machined and Ground High Strength Steels, DMIC Report, 210 (1964), pp. 54-77.

[1966Zor] N.N. Zorev, Metal Cutting Mechanics, Pergaon Press, Oxford, 1996.

[1970Fie] M. Fied and J. Kahles, Review of surface Integrity of Machined Components, Annals of the CIRP, 2 (20) (1971). pp. 153-162.

[1970Kos] W. Koster, and J. Fritz. Surface lntegrity in Conventional Machining, Metal Cutting Research Associates, ASME paper 70GT100, 1970.

[1970Ram] R. Ramaswami, The Effect of Built-Up Edge on the Wear of Cutting Tools. Production engineering and machine tool section, Madras, 1970.

[1970Zal] N. Zaltin, Modern Machine Shop, 42 (1970), pp. 139-144.

[1975Bro] K. J. A . Brookes, Hardmetal and other Hard Materials, Initiation Process in WC-Co Alloys, Acta. Metall., 23 (1975) pp. 109–115.

[1975Luy] S.B. Luyckx, Role of Inclusions in the Fracture Initiation Process in WC-Co Alloys, Acta. Metall., 23 (1975), pp. 109-115.

[1976Rud] O. Rudiger and H.E. Exner, Application of Basic Research to the Development of Hard Metals, Powd. Metall. Int., 8 (1976), pp. 7-13.

[1981For] A. L. Forrest, “Effect of Metal Chemistry on Behaviour of Titanium in industrial applications” Industrial Application of Titanium and Zirconium, (1981) pp. 112.

[1983Ree] R.P Reed, and A.F. Clark, Materials at Low Temperatures, American Society for Metals, Carnes Publication, Metal Park, OH., 1983.

[1984Kay] W. A. Kaysser, G. Petzo, Emergent Process Methods for High-Technology Ceramics, Volume 17 of the series Materials Science Research, (1984), pp. 225-231.

[1984Mye] H. Bomberger, F. Froes, Processing Titanium and Their Alloys, J.O.M. (1984), pp. 50-60.

[1984War] R. Warren, and B. Johanesson, Sintered Metal Ceramic Composites, Elsevier, Amsterdam, Netherlands, 1984.

[1985Asm] ASM Metals Handbook-Desk Edition, 1985, ASM International, (1985), pp. 27–29.

[1985She] D. Shetty, I. Wright, P. Mincer, and A. Clauer, Indentation Fracture of WC-Co Cermets, J. Mater. Sci., 20(1985) 1873-1882.

[1989Mac] R. Machado, J.wallbank, Machining of Titanium and it’s Alloy-A review, Warwick, 2012.

[1990Mac] A. R. Machado, and J. Wallbank, Machining of titanium and its alloys- A Review, Proceedings Institution of Mechanical Engineers, Journal of Engineering Manufacturing, (1990), Vol. 204, pp. 53–60.

[1991Jen] I. Jenkins and J.V. Woods, Powders Metallurgy - An Overview, Brookfield, The Institute of Metals, USA, 1991.

[1993Hon[a]] H. Hong, A. Riga, J. Cahoon, and G. Scott. "An Experimental Study of Wire EDM on Ti-8Al-4V, Tribology International, (1993), 34-39.

[1993Saw] S. Sukvittayawong and I. Inasaki, Detection of Built-up Edge in Turning Process. Internal Journal on Machine Tools and Manufacture, 6 (33) (1993), pp. 829 – 840.

[1995Hen] S. Henry, F. Reidenbach, G. Davidson, R. Boring, W. O'Loughlin,. J. Scott, ASM Speciality Handbook. Tool materials Davis J, editor. United States of America: ASM international. The materials Information Society, 1995.

[1995Her] W. Hertzberg, Deformation and Fracture Mechanics of Engineering Materials, Wiley, 4 (1995).

[1995Spr] E. Spreffrey, A history of fine grained hard metals, International Journal of Refractory Metals and Hard Materials, (1995), pp. 241–255.

[1996Exr] H.E. Exner, Understanding the toughness and the strength of WC–Co hard metals, Proceedings of the Euro PM'96, (1996), pp. 255–262.

[1996Joh] M. John, Structural Alloys Handbook, Technical Ed, Purde University, Wesr Lafayette, IN. (1996).

[1996Qui] D. Quinto, Technology Perspective on CVD and PVD Coated Metal-Cutting Tools. International Journal of Refractory Metals & Hard Materials, 14 (1996), pp. 7-20.

[1996Url] http://www.gordonengland.co.uk/hardness/rockwell.html (2015): Accessed 5/10/2015.

[1997Ezu] E.O. Ezugwu, Z.M. Wang, Titanium alloys and their machinability, a review Journal of material Processing Technology. 68 (1997), pp. 262-274.

[1997Ste] D. A. Stephenson, Metal Cutting Theory and Practice, Marcel Dekker, pp. (1997) 144.

[1997Sie] J. Siekmann, How to Use Titanium, Tool Eng., 34 (1955), pp. 78-82.

[1998Cha] H.E. Chandler, Machining of reactive metals, Metals Handbook volume 16: machining, (1998) pp. 844-857.

[1998Chi] T. Childs, K. Maekawa, and P. Maulik, Effects of coolant on temperature distribution in metal machining. Materials Science and Technology, 4(11) (1998), pp. 1006-1019.

[1999Fri] T. Friemuth, J. Winkler, Machining of magnesium workpieces. Adv. Eng. Mater. 3 -4 (1999), pp. 183–186.

[1999Tok] M. Tokita, Mechanism of Spark Plasma Sintering, (Kawasaki-shi Kanagawa, Japan: Sumitomo Coal Mining Company, Ltd., (1999), pp. 3-7.

[2000Chi] T. Childs, A6.2 Cemented carbides and cements. Metal Machining Theory and Applications. Butterworth-Heinemann, (2000), pp. 388.

[2000Hod] M. Hodgkinson, Mechanical Testing of Advanced Fibre Composites, Cambridge, Woodhead, (2000), pp. 132–133.

[2000Sre] P. Sreejith and B. Ngoi, Dry machining, Machining of the future, Journal of Materials Processing Technology, 101 (2000), pp. 287-291.

[2000Tre] E. Trent, “Metal cutting”, New York, Butterworth-Heinamann, 2000.

[2000Wit] P. J. Withers, and H.K. Bhadeshia, Residual Stress Measurement techniques, Materials Science and Technology, 17 (2001), pp.355-365.

[2001Che] C. H. Che-Haron, Tool life and surface integrity in turning titanium alloy, J Mater Process Technol., 118 (2011), pp. 231–237.

[2002Bra] D.U. Braga, A.E. Diniz, .A. Miranda, and N.L. Coppini, Using a minimum quantity of lubricant (MQL) and a diamond coated tool in the drilling of aluminium-silicon alloys, J. Mater. Process. Technol., 122 (2002), pp. 127-138.

[2002Pet] G. Petzow, and M. Herrmann, Silicon nitride ceramics, Struct. Bond. 102 (2002), pp. 47–167.

[2003Kri] C, Krishna, Automated planning and optimization of machining processes; A system approach. Massachusetts institute of technology, Department of industrial engineering and operations research, Syracuse University, 2003.

[2003Pau] E. Paul, J. T. Black, R. A. Kosher, Materials and Processes in Manufacturing, Wiley, (9), 2003.

[2004Bal] M. J. Balart, A. Bouzina, L. Edward, and M. Fitzpatrick, The onset of tensile residual stresses in grinding of hardened steels. Mater. Sci. Eng., 367 (2004), pp. 132–142.

[2004Dud] D. Dudzinski, A. Devillèz, A. Moufki, D. Larrouquere, V. Zerrouki, and J. Vigneau, A review of developments towards dry and high speed machining of Inconel 718 alloy. Int. J. Mach. Tools Manuf. 44 (2004), pp. 439 – 456.

[2004Ina] K. Weinert, I. Inasaki, J. W. Sutherland, and T. Wakabayashi, Dry machining and minimum quantity lubrication, CIRP Annals - Manufacturing Technology, 2 (2004), pp. 511–537.

[2004Wei] K. Weinert, I. Inasaki, J. W. Sutherland, Dry Machining and Minimum Quantity Lubrication, University of Dortmound, Germany, 2004.

[2005Cap] J.M. Capus, More roads point to cheaper titanium powder, Metal Powder Report, Vol. 60, (2005), pp. 22-23.

[2005Fit[a]] M. Fitzpatrick, A. Fry, P. Holdway, F. Kandil, J. Shackleton, and L. Suominen, Determination of Residual Stresses by X-ray Diffraction, The queens publisher, Middlesex UK., 2005.

[2005Fit[b]] M. Fitzpatrick, Measurement good practice guide: Determination of residual stresses by x-ray diffraction," National Physical Laboratory, 2 (56) 2005.

[2005Grz] W. K. Grzesik, S. C. Lubomír, H, Jiřina, Machining titanium and its alloys : state-of-the-art, Sborník vědeckých prací Vysoké školy báňské - Technické univerzity Ostrava, Vol. 48, (2005), pp. 89-95.

[2005Kan] S. Kang, Sintering, Densification, Grain Growth and Microstructure, Elsevier Butterworth-Heinemann, 1 (2005), pp. 265.

[2005Yan] H. Yan, J, Hua, R. Shivpuri, Numerical simulation of finish hard turning for AISI H13 die steel. Sci. and Tech Adv. Mat. (6) (2005), pp. 540.

[2006Cus] C. Cus, U. Zuperl, Kiker , E. M. Milfelner "Adaptive Controller Design for Federate Maximization of Machining Process," Journal of Achievements in Materials and Manufacturing Engineering, 17, (2006), pp 237–239.

[2006Enc] Encyclopedia Britannica – Titanium, Retrieved 29 December, 2006.

[2006Jaw] L. Jaworska, M. Rozmus, B. Królicka, and A. Twardowska, Functionally Graded Cerments, J. Ach. Materials and Manufacturing Engineering, 17 (2006), pp. 73-76.

[2006Mce] A. Mcevily, P. Moreira, Analysis of the effect of cold-working of rivet holes on the fatigue life of an aluminium alloy. Int. J Fatigue, 2006.

[2006Son] X. Song, X. Liu, and J. Zhang, Neck formation and self-adjusting mechanism of neck growth of conducting in spark plasma sintering. J. Am. Ceram. Soc. 89 (2) (2006), pp.494–500.

[2007Lia] Y. Liao, H. Lin, and Y. Chen "Feasibility Study of the Minimum Quantity Lubrication in High-speed End Milling of Nak80 Hardened steel by Coated Carbide Tool," International Journal of Machining Tools and Manufacture, 47, pp.1667-1676 (2007).

[2007San] Sandvik, Titanium Machining Guide. Sweden, 2007.

[2007Kor] I. Korkut, M. A. Donertas, The influence of feed rate and cutting speed on the forces, surface roughness and tool-chip contact length during face milling. Mater. Des. 28(1) (2007), pp. 308–312.

[2008Ast] V.P. Astakhov, Ecological machining: near-dry machining. In: Davim JP (ed) Machining: fundamentals and recent advances. Springer, London, 2008.

[2008Bon] K. Bonny, P. Beast, J. Vleugles, Haung S, and B. Lauwers, Dry reciprocating slidding friction and wear response of WC-Ni cemented carbide. Tribol, Lett., 31 (2008), pp. 199 – 109.

[2008Gao] F. Gao, R.K. Leach, J. Petzing, and J.M. Coupland, Surface Measurement errors using commercial scanning white light interferometers, Measurement Science and Technology, 19 (1) (2008).

[2008Hua] S.G. Huang, R.L. Liu, O. Vander, and J. Vleugels, NbC as grain growth inhibitor and carbide in WC–Co hardmetals. Int. J. Refract. Met. Hard Mater. 36 (2008), pp. 389–95.

[2008Ran] M. G Randall, S. Pavan, J.P Seong, Review on Liquid Phase Sintering, Journal of Materials Science (Impact Factor: 2.37). 44(1) (2008), pp. 1-39.

[2008San] C. Sandvik, Application Guide: Titanium machining, Sweden, 2008.

[2008Smi] P. Smid, CNC Programming Handbook (3rd ed). New York Industrial press, 2008.

[2008Tha] S. Thamizhmanii and S. Hasa, Investigating Flank Wear and Cutting Force on Hard Steels by CBN Cutting Tool by Turning, Proceedings of the World Congress on Engineering, WCE, London, U.K. 3 (2008).

[2009Asm] ASME, Dimensioning and Tolerancing, ASMW,Y14.5, American Society of Mechanical Engineers, 2009.

[2009Ibr] G.A. Ibrahim, C.H. Che Haron, and J.A Ghani, The Effect of Dry Machining on surface Intergrity of Titanium Alloy Ti-6Al-4V Eli, Journal of applied Sciences, Vol. 9 (2009), pp.121-127.

[2009Sch] G. Schnieder, Cutting tool materials, American machinist, 2009.

[2009Url] http://www.custompartnet.com/wu/milling. Assessed 9/11/2015.

[2010Dav] J. Davim, Surface Integrity in Machining, Springer, 2010.

[2010Get] G. A. Getosthuizen, Wear characterisation in milling of Ti6Al4V – A wear map approach. Dissertation presented for the degree of Doctor of Engineering at the University of Stellenbosch, 2010.

[2011Ali] S.M. Ali, R.N. Dhar, and S.K. Dey, Effect of Minimum Quantity Lubrication (MQL) on Cutting Performance in Turning Medium Carbon Steel by Uncoated Carbide Insert at Different Speed-Feed Combination, Advances in Production Engineering and Management, 6 (3) (2011), pp. 185-196.

[2011Kar] M. Karin, WC grain growth during sintering of cemented carbides, Doctoral Thesis Stockholm, Sweden, 2011.

[2011Lop] L.N. López de Lacalle, A. Lamikiz, J. Fernández de Larrinoa and I. Azkona, Advanced Cutting Tools, University of the Basque Country, Spain.

[2011Ros] N. Rossini, M.Dassisti, K. Benyounis, and A. Olabi, Methods of measuring residual stresses in components, Materials and Design, 35 (2011), pp. 572-588.

[2011Url] http://www.residualstress.org (2015): Accessed 7/08/2015.

[2012Dra] P. Drajith, Manufacturing Engineering Tripos, Part IIA, Production Machines and Systems, 2012.

[2012Ije] Factors Influencing Cutting Forces in Turning and Development of Software to Estimate Cutting Forces in Turning. International Journal of Engineering and Innovative Technology (IJEIT) 2(1), 2012.

[2012Hit] H. Hitano et al., A study for high accuracy measurement of residual stress by deep hole drilling technique Journal of Physics, Conference Series 379, 2012.

[2012Jin] A. Jidnal, Analysis of Tool Wear Rate in Drilling Operation using Scanning Electron Microscope (SEM), Journal of Minerals & Materials Characterization & Engineering, 11 (1) (2012), pp. 43-54.

[2012Joe] J. Thompson, Creating the best surface finish means choosing the proper insert, cutting conditions, technique, Canadian Industrial Machinery, 2012.

[2012Mac] C. Biermann, Machining of β-Titanium Alloy (Ti–10V–2Fe–3Al) Under Cryogenic Conditions Cooling with Co_2 Snow, Journal of Materials Processing Technology, 211 (6) (2011), pp. 1175-1183.

[2012Par] A. Parlikad, Manufacturing Engineering Tripos Part-A, Production Machines and Systems, 2012.

[2012Sad] A. B. Sadat, Surface Integrity When Machining Metal Matrix Composite, In Machining Metal Matrix Composite, London, Springer-Verlag London Limited, (2012), pp.51-61.

[2013Akh] H. Akhtar, Fundamentals of Metal Cutting and Machining Process, Kalpakjian and Grover, 2013.

[2013Cha] A.B. Chattopadhyay, Manufacturing Processes, Department of Mechanical Engineering, Institute of Technology, Kharagpur, 2013.

[2013Gen[a]] R.M. Genga, L.A. Cornish, and G. Akdogan. "Effect of Mo2C Addition on the Properties of SPS Manufactured WC-TiC-Ni Cemented Carbide", Int. J. Refract. Met. Hard Mater. 41 (2013), pp. 2-21.

[2013Gen[b]] R. Genga, Microstructure and Properties of Selected WC-Cemented Carbides Manufactured by SPS Method, 2013.

[2013Sha] S. Shajer, Practical Residual Stress Measurement Methods, Wiley, 2013.

[2013Ush] T. Usher, The Modern Machinist, N. W. Henley. (2), 2013.

[2014Gen] R.M. Genga, G. Akdonga, C. Polese, J.C. Carrett, L.A. Cornish, Abrasion Wear, Thermal Shock and Impact Resistance of WC-Cemented Carbides produced by PECS and LPS, Elsevier, 2014.

[2014Kum] A. Kumar and S.Mohanty, A Review on the Effect of Process Parameters on Different Output Parameters during Machining of Several Materials, International Journal of Engineering Science and Research, 2014.

[2014Sat] K. Satyanarayana, N. Ravi, K. Shivachi, and A. Venu Surface Integrity and Optimization in Turning Ti-6Al-4V, 5th International & 26th Manufacturing technology, Design and Research Conference, 2014

[2015Url[a]] https://www.sartorius.co.uk/en/product/product-detail/cpa224s (2015): Accessed 22/09/2015.

[2015Url[b]] https://en.wikipedia.org/wiki/Rake_angle (2012): Accessed 01/06/2015.

[2015Url[c]] www.olympusims.com/en/knowledge/metrology/roughness/2d_parameter (2015): Accessed 07/09/2015.

[2015 Wil] R. Willcutt, "When the chips are down", Modern Machine Shop, url= http://www.mmsonline.com/blog/post/when-the-chips-are-down, (2015).